



University
of Glasgow

Isa, Hafizah Noor (2019) *Towards reliable quantification of mixed oxide coating for LIGO using DualEELS*. PhD thesis.

<https://theses.gla.ac.uk/74354/>

Copyright and moral rights for this work are retained by the author

A copy can be downloaded for personal non-commercial research or study, without prior permission or charge

This work cannot be reproduced or quoted extensively from without first obtaining permission in writing from the author

The content must not be changed in any way or sold commercially in any format or medium without the formal permission of the author

When referring to this work, full bibliographic details including the author, title, awarding institution and date of the thesis must be given

Enlighten: Theses

<https://theses.gla.ac.uk/>
research-enlighten@glasgow.ac.uk

Towards Reliable Quantification of Mixed Oxide Coating for LIGO using DualEELS

Hafizah Noor Isa

Submitted in fulfilment of the requirements for the Degree
of Doctor Philosophy

School of Physics and Astronomy
College of Science and Engineering
University of Glasgow



University
of Glasgow

August 2019

Abstract

Gravitational Waves are a prediction of the General Theory of relativity, the last one to be experimentally verified by big international collaborations, using kilometre-sized interferometric detectors. Although the waves were indirectly observed in the spin-down of pulsars since the 80's, the direct detections was a significant breakthrough, and opened new vistas for astrophysicists and relativity researchers. The huge interferometers involved in the discovery used highly developed optics for the manipulation (reflection, beam splitting, and detection of interference) of infrared laser beams. The reflectors at the end of each interferometer arm are an integral part of the detector, allowing the enlargement of the optical path of the laser beam and increasing the sensitivity. In order to further improve the sensitivity of these detectors, improvement of these reflectors' surface and optical characteristics is of paramount importance. In the present thesis, new methods of surface characterization and quantification of the optical surfaces of these mirrors are developed and presented.

Highly reflective coating materials for the interferometer mirrors are selected based on their thermal/mechanical properties. It is a well-established fact that the mechanical bulk properties are directly connected to the thermal quantum noise, which is the parameter to minimize in a reflective coating used in a gravitational wave detector. However, the parameter space to explore is vast, including atoms used, composition percentages and thermal processing of the final material, and impossible to analyze well on a trial-and-error basis. Furthermore, the amorphous nature of the coating materials defies a simple theoretical description of the bulk or microscopic properties, and calls for detailed reporting of all processing steps. The microscopic examination of processed, candidate samples can reveal discrepancies between nominal and actual composition, and also give information on the effects of the thermal annealing on the exact atom arrangement in the material.

The novelty of our approach is dual: First, we use the concept of 'standard' samples, i.e. materials that contain the same or similar atoms as in the coatings

under consideration, in similar spatial arrangements. Second, we apply the recent advances in electron microscopy optics and electron energy loss spectrometry (EELS) to obtain signature spectra in energy loss ranges higher than those used before. These two innovations in tandem allow us to study in detail one coating configuration already used in Advanced-LIGO, a working gravitational wave detector, and a new, candidate coating for a next generation detector. The results of our analysis show significant discrepancies between nominal and actual composition values, up to almost 35% in some cases. They also show composition inhomogeneity over the surface of a sample, depending on the thermal history and composition values thereof.

The techniques described here can be used for two purposes: On the one hand, they can be used together with mechanical property data from the exact same samples in order to inform a phenomenological theory connecting composition and thermal history to bulk mechanical properties (and hence to thermal noise level). Furthermore, if automated enough, these techniques can be used as a 'quality control' method of massively produced coating for a future gravitational wave detector.

Table of Contents

Abstract.....	ii
Author’s Declaration.....	vii
Acknowledgement.....	ix
List of Acronyms.....	x
List of Figures.....	xi
Preface	xiv
1. Gravitational Wave Astronomy, Detectors, and Materials for Improved Detector Sensitivity.....	1
1.1. Gravitational wave astronomy	1
1.2. The nature of Gravitational waves	2
1.3. Sources of gravitational waves	4
1.3.1. Continuous waves.....	5
1.3.2. Binary signal	5
1.3.3. Burst signal	7
1.3.4. Stochastic background	8
1.4. Gravitational waves detectors	9
1.5. Third generation Detectors	11
1.5.1. Noise Sources	12
1.6. Coating for optics	16
1.6.1. Overall concept-multilayers and material choices	16
1.6.2. Mechanical loss and its origin	17
1.6.3. Characterisation of coatings	19
1.7. Conclusion.....	24
2. Instrumentation and Sample Preparation.....	26
2.1. Principle of STEM.....	26
2.1.1. Optical arrangement	27

2.1.2.	Lenses	30
2.1.3.	Scanning.....	32
2.2.	Overview of the Microscopes used in this Work	33
2.2.1.	The FEI Tecnai T20	33
2.2.2.	The ARM.....	35
2.2.3.	Electron lenses and aberrations	36
2.2.4.	Image resolution and aberration correction	39
2.3.	The FIB.....	41
2.4.	Sample Preparation	42
2.4.1.	Specimen for TEM.....	43
2.5.	Electron Energy Loss Spectroscopy	49
2.5.1.	Interaction of Electrons with the Sample	50
2.5.2.	Electron energy-loss spectrometer.....	54
2.5.3.	EELS	55
2.5.4.	Dual Electron Energy Loss Spectroscopy (DualEELS).....	57
2.5.5.	Spectrum imaging.....	58
2.5.6.	Common processing techniques	59
2.6.	Quantitative Standards-Based Elemental Analysis with EELS.....	66
2.7.	Multiple Linear Least Squares (MLLS) Fitting	68
2.8.	Conclusion.....	69
3.	Quantification of Ta ₂ O ₅ -TiO ₂ Film Composition	71
3.1.	Research approach	71
3.2.	Cross section determination	75
3.2.1.	Titanium cross sections	75
3.2.2.	Tantalum cross sections	82
3.2.3.	Chosen standards	85
3.3.	Ta ₂ O ₅ -TiO ₂ elemental analysis with experimental cross sections.....	86
3.3.1.	MLLS fitting Ta ₂ O ₅ -TiO ₂	88

3.4. Conclusion.....	93
4. Quantifying Ta ₂ O ₅ -ZrO ₂ Film Compositions	94
4.1. General concept.....	94
4.2. Cross section determination.....	98
4.2.1. Tantalum.....	98
4.2.2. Zirconium	99
4.3. Towards elemental analysis with cross section.....	101
4.4. Conclusion.....	104
5. Conclusion and Future Work	105
Bibliography.....	109
Appendix A	118
Appendix B	124
Appendix C	130

Author's Declaration

This thesis is an account and record of research carried out at the Institute for Gravitational Research and the Materials and Condensed Matter Physics Group, School of Physics and Astronomy at the University of Glasgow, between April 2014 and October 2018. The work described herein is my own, except where specific reference is made to the work of others. The contents of this dissertation are original and have not been submitted in whole or in part for consideration for any other degree or qualification in this, or any other university.

Hafizah Noor Isa

August 2019

The author has contributed to experimental work in the following publications:

Observation of Gravitational Waves from a Binary Black Hole Merger

By: Abbott, B. P.; Abbott, R.; Abbott, T. D.; et al.

Group Author(s): LIGO Sci Collaboration; Virgo Collaboration

PHYSICAL REVIEW LETTERS Volume: 116 Issue: 6 Article Number: 061102

Published: FEB 11 2016

and other whole LIGO collaboration papers, as part of the Optics Working Group within the LIGO collaboration.

And specifically to the following short author list paper:

- Order, disorder and mixing: The atomic structure of amorphous mixtures of titania and tantala

Riccardo Bassiri, Matthew R. Abernathy, Franklin Liou, Apurva Mehta, Eric K. Gustafson, Martin J. Hart, Hafizah N. Isa, Namjun Kim, Angie C. Lin, Ian MacLaren, Iain W. Martin, Roger K. Route, Sheila Rowan, Badri Shyam, Jonathan F. Stebbins, Martin M. Fejer, *J. Non Cryst. Sol.* **438** (2016) 59.

(Bassiri et al. 2016)

The following presentation has also been given at a conference:

- Hafizah N. Isa *et al.*, Reliable Quantification of the composition of (Ta,Ti)O_x mirror coatings, Poster Presentation, LSC-Virgo Meeting, Pasadena, California, March 2015.

Acknowledgement

I would like to express my special appreciation and thanks to my supervisor and advisor, Dr. Ian MacLaren you have been a tremendous mentor for me and you have guided me until the completion of my thesis. A special thanks to Prof. Sheila Rowan, your efforts of looking for ways to support me financially when times were tough, I am thankful to you both for encouraging my research and for allowing me to grow as a research scientist.

A special thanks to the members of the IGR and MCMP groups who have contributed immensely to my personal and professional time at University of Glasgow. These groups have been a source of friendship, tremendous opportunities of collaboration at an international level. A special mention of appreciation goes to Dr Sam McFadzean, Colin How and William Smith for their technical expertise in solving many of the problems I faced along the way.

A note of appreciation is for the LIGO collaboration. It is an honour to have been a part of the project, and to be associated with one of the greatest scientific discoveries of our times.

Not forgetting, lots of love and thanks to my family. Words cannot express how grateful I am to my parents and siblings as well as my nephews and nieces, who have been a great source of support to me, especially in helping me making me feel less homesick. Your prayer for me was what sustained me thus far. I would also like to thank my friends here in Glasgow especially my flatmates who have continuously supported me and looking after me; ensuring that I took meals on time and spending time to help me de-stress. Thank you for supporting me for everything and encouraging me throughout this experience.

Finally, I thank God, for letting me through all the difficulties. I have experienced Your guidance day by day. You are the one who let me finish my degree, and for that, I am forever grateful with the bless you have bestowed upon me. Thank you, Allah.

List of Acronyms

ARM - Atomic Resolution Microscope

CCD - Charge-Coupled Device

DM - Digital Micrograph

DualEELS - Dual Range Electron Energy Loss Spectroscopy

EDX - Energy Dispersive X-ray Analysis

EEL - Electron Energy Loss

EELS - Electron Energy Loss Spectroscopy

EELS -SI - Electron Energy Loss Spectroscopy - Spectrum Imaging

ELNES - Electron Loss Near-Edge Structures

EXELFS - Extended Energy Loss Fine Structure

FIB - Focused Ion Beam

GIF - Gatan Image Filter

GIS - Gas Injection Source

GMS - Gatan Microscopy Suite

HAADF - High Angle Annular Dark Field

MSA - Multi Statistical Analysis

PCA - Principal Component Analysis

PIPS - Precision Ion Polishing System

SEM - Scanning Electron Microscope

STEM - Scanning Transmission Electron Microscope

TEM - Transmission Electron Microscope

ZLP - Zero Loss Peak

List of Figures

<i>Figure 1-1: The observable effects on a system of masses arranged in a circle, of a gravitational wave that travels perpendicular to the page. (Kokkotas, 2002)...</i>	3
<i>Figure 1-2: Interferometric gravitational wave detector, principle of operation: The Michelson interferometer (Kokkotas, 2002).....</i>	10
<i>Figure 1-3: Principal noise sources for Advanced LIGO. Quantum noise includes shot noise and intensity fluctuations. Coating Brownian noise is the second most important noise source over much of the detector operating frequencies (Advanced LIGO Collaboration, Instrument Science White Paper).</i>	15
<i>Figure 1-4: Predicted structure of Tantalum pentoxide (light spheres are Ta atoms, dark ones are O atoms) (Reid & Martin, 2006)</i>	22
<i>Figure 2-1 : A schematic representation of an electron microscope. Operating in a high vacuum chamber to allow unimpeded electron motion, the flow of electrons and successive focusing actions are shown simply by straight lines. Apertures are used to help remove stray, unfocused electrons and increase contrast (Ahn, 2004).</i>	28
<i>Figure 2-2: Detector arrangement for a STEM (Williams& Carter, 2009).....</i>	30
<i>Figure 2-3: Schematic of a magnetic lens in cross-section, the major building block of an electron microscope; comparison with optical (converging) lens (University of Sydney, microscope. training, 2012).....</i>	31
<i>Figure 2-4: Schematic diagram of the FEI Tecnai T20 TEM (Portland State U., TEM Operating manual, 2010).</i>	34
<i>Figure 2-5: Schematic defining the incoming beam half-angle α (and the collection half-angles B_1, B_2) (From jeol.co.jp, Glossary of TEM terms)</i>	40
<i>Figure 2-6: The final stages of TEM sample preparation steps using the cross-section technique: From left to right, Coating-to-coating gluing, enclosure in molybdenum and copper, dimpling with dimpler, and ion polishing (Hart, 2017)</i>	45
<i>Figure 2-7: Scheme of columns in DualBeam FIB (Kizilyaprak et al., 2014).....</i>	46
<i>Figure 2-8: Specimen attached to the Omniprobe grid a) before b) after separation of the micro manipulator, c) the Omniprobe holder with specimen on the left B holder seen with 400x magnification with electron source, d) specimen</i>	

<i>after thinning from both sides. Photos were acquired during standard specimen preparation session. (Joana, 2017)</i>	48
<i>Figure 2-9: Definitions of α and β in (S)TEM showing α, the convergence semi-angle and β, the collection semi-angle.</i>	50
<i>Figure 2-10: Synopsis of possible electron-specimen interactions (Tran, 2017).</i> .	51
<i>Figure 2-11: A particle view of electron scattering. a) Elastic scattering that is caused by Coulomb attraction by the nucleus. Coulomb repulsion leads to inelastic scattering in b) Inner- and c) Outer- shell electrons that are excited to higher energy level</i>	52
<i>Figure 2-12: Schematic illustration of energy-loss spectrum and the generation of energy-loss peaks</i>	53
<i>Figure 2-13: Schematic diagram of the EEL spectrometer used in this study (Bobyanko, 2018).</i>	55
<i>Figure 2-14: An EEL spectrum, showing the principal characteristics (Williams and Carter, 2009).</i>	57
<i>Figure 2-15: Schematic representation of the spectrum imaging technique: Each x-y point on the specimen is associated with a spectrum (points on the E-axis), i.e. each cube contains an electron intensity value at this point in x,y, E (Egerton, 2016)</i>	59
<i>Figure 2-16: Graphic Synopsis of the analysis flow.</i>	65
<i>Figure 3-1: The area of the sample used for the cross section measurement: a) survey image for TiO_2; b) survey image for SrTiO_3 c) thickness map of the area scanned in the TiO_2.</i>	76
<i>Figure 3-2: Amorphous carbon in the amorphous TiO_2 film, clearly present in some areas in the spectrum, and clearly seen in elemental maps from EELS (60 eV background windows before edge, 50 eV integration window post-edge) with Ti in aqua and C in red.</i>	77
<i>Figure 3-3: Cross section for the Ti-L_{23} edge in all studied samples.</i>	78
<i>Figure 3-4: ELNES region of the Ti-L_{23} cross sections for different compounds containing Ti, and their comparison to a scaled cross section for one of the TiO_2-Ta_2O_5 glasses.</i>	80
<i>Figure 3-5: EELS spectra of cross section with background subtracted and without background-subtracted of $\text{Ti-L}_{2,3}$ and O-K.</i>	81

Figure 3-6: The area of the sample used for the cross section measurement: a) survey image for 003 Ta ₂ O ₅ 300 °C; b) Survey image for 004 Ta ₂ O ₅ 300 °C c) Survey image for LiTaO ₃ . d) Relative thickness colour scale	82
Figure 3-7: Cross section from Ta ₂ O ₅ 300 °C and LiTaO ₃ without background subtract.....	83
Figure 3-8: Background-subtracted cross sections of Ta-N _{4,5} (and O-K) of Ta ₂ O ₅ 300 °C and LiTaO ₃	84
Figure 3-9: Background-subtracted normalised deconvolved spectra for two different oxide compounds containing Ta: LiTaO ₃ and Ta ₂ O ₅	85
Figure 3-10: Cross section for two standards on the same plot including the backgrounds.	86
Figure 3-11: MLLS fit on CSIRO samples a)CSIRO 25 Ti 600 °C, b) CSIRO 25 Ti 400 °C, c) CSIRO 25 Ti 200 °C and d) CSIRO 55 Ti 600 °C	88
Figure 3-12: MLLS fit on CSIRO samples with extra background on MLLS fit a)CSIRO 25 Ti 600 °C, b) CSIRO 25 Ti 400 °C, c) CSIRO 25 Ti 200 °C and d) CSIRO 55 Ti 600 °C	90
Figure 3-13: EELS mapping of Ti and Ta cation percentage for CSIRO samples with 25% and 55% coating of Ti heat treated at different temperature.	91
Figure 3-14: Titanium cation relative percentage	92
Figure 4-1: An EELS spectrum of Zr-Ta-O the real sample after deconvolution that will be fitted using the MLLS method to find the accurate composition.	97
Figure 4-2: The area of the Ta ₂ O ₅ 300 °C sample used for the cross-section measurement.....	98
Figure 4-3: EELS differential cross section for the Ta M-edges from a Ta ₂ O ₅ glass, calculated after background subtraction from a 100ev window before the Ta-M _{4,5} edges and Fourier ratio deconvolution with the low loss.	99
Figure 4-4: The area of the ZrO ₂ sample used for the cross-section measurement.	100
Figure 4-5: Differential cross section for the ZrO ₂ L-edges.	100
Figure 4-6: MLLS fit to the ZrO ₂ -Ta ₂ O ₅ LIGO sample.....	102
Figure 4-7: EELS mapping of Zr and Ta cation percentage taken at 47 × 26 pixel size and the histogram graph Ta and Zr and histogram graph for the Ta and Zr percentage.	103

Preface

Chapter 1 is a brief overview of the nature and sources of gravitational waves, together with a simple historical overview of the detection efforts. Interferometric detectors are presented in detail, and the noise sources limiting their detector sensitivity are analyzed. In particular, the importance of highly-reflective mirror coatings and the thermal noise they introduce to the system is expounded on, followed by efforts to improve them.

Chapter 2 describes the methods of atomic structure investigation that are used in this thesis. After presenting the principle of operation of Transmission Electron Microscopy (TEM) and the Scanning TEM (STEM), the particular instruments used for the present work, the sample preparation techniques and the data analysis processes used are presented in detail. Moreover, the Electron Energy Loss Spectrometry technique is presented and its use for the mirror coatings investigated is explained.

Chapter 3 presents the STEM investigation of the various titania doped tantala coatings covered in the present research. After presenting the EELS spectra of various ‘standard’ samples (materials containing the same atoms as the coatings, in similar spatial arrangement), an analysis technique is selected that minimizes the errors; then, the actual mirror coatings used in A-LIGO are investigated as regards their composition and homogeneity.

Chapter 4 presents the STEM investigation of the various zirconia doped tantala coatings covered in the present research. In the beginning, innovative STEM optics

modifications that allow the extension of EELS to higher energies are exposed, which allow the quantification of Zr atoms. Then a similar analysis flow as in Chapter 3, recording standard samples' spectra and comparing/fitting them to a candidate coating is followed.

Finally, Chapter 5 summarizes the findings of the present research as regards currently-used and future mirror coating materials and proposes ways that these results can be used in the future research of high-reflective mirror coatings for gravitational wave detectors.

1. Gravitational Wave Astronomy, Detectors, and Materials for Improved Detector Sensitivity

1.1. Gravitational wave astronomy

Gravitational waves were already predicted by Einstein (Einstein, 1916), shortly after his formulation of the General Theory of Relativity in 1916. The theory describes the force of gravity as a distortion of space-time, the entity which combines the three-dimensional space and one-dimensional time. This space-time distortion, according to general relativity, is caused by the presence of mass or energy, which is famously equivalent to mass and, in turn, the distortion of course defines how the masses (or the energy) move (or flow). This deceptively simple description is summarised in an equally deceptively simple equation (1):

$$G_{\alpha\beta} = 8\pi T_{\alpha\beta} \quad (1)$$

In equation (1), $G_{\alpha\beta}$ measures the local space-time curvature, and $T_{\alpha\beta}$ describes the distribution of energy-momentum. Both quantities are in fact tensors (multi-dimensional matrices), and the above is finally translated into 10 coupled, non-linear, partial differential equations (Misner et al., 1973). No general solution has been found yet to the above equations, but even shortly after their discovery, Einstein could solve an approximation to them (Einstein, 1916, 1918), which gave rise to a wave-like disturbance of the space-time, travelling away from asymmetrically accelerating masses. The absolute magnitude of the travelling disturbance is extremely minute, since the gravitational force is extremely weak, except when huge masses are involved.

Huge masses and extreme accelerations are therefore needed in order to create observable waves. These can be found in three quite dramatic cosmic events, namely supernova explosions, coalescing (“inspiring”) neutron stars, or coalescing black holes. These processes are quite rare and are usually found at

huge distances from the Earth (in other galaxies). Therefore, the magnitude of the gravitational waves that reach the Earth is strongly diminished. However, they are very interesting to observe not only because they are a direct prediction of the general theory of relativity but also because they are essentially the only indications that the events (especially the inspiraling) are happening, and they travel practically undisturbed by the presence of any mass or electromagnetic fields between the source and the detector. The recent observation of gravitational waves, in combination with other astronomical observations, for example of neutrinos of astronomical origin, have given rise to a new kind of astronomy, called ‘multi-messenger’ astronomy (Abbott et al., 2016c).

1.2. The nature of Gravitational waves

As explained in the previous section, the general relativistic description of the generation and propagation of gravitational waves starts with the Einstein field equations (1). These can be solved exactly in some simple, idealised conditions. A trivial example is a region of space that contains no matter-energy distribution at all. In this ‘empty’ universe, the right-hand side of (1) is 0, and the left-hand side is consequently, also null. The curvature of space-time is zero, and the space-time can therefore be described as a “Minkowski space”, a model of space-time coming from the *special* theory of relativity. (In Minkowski space, the space-time distance between two events is independent of the frame of reference of the observer). The ‘empty’, trivial model just described can then become the basis for the next simplest one: a region of space quite far from any strong mass-energy distribution. An observer far away from a matter distribution, sees a local space-time metric that is approximately Minkowski-like, $g_{\mu\nu}$. A change in the distribution of matter will induce a change in space-time. This change will be propagated in other points of space-time and will arrive at the position of an observer, who will see a change in the local metric. When these disturbances are small enough, the change can be written as a ‘perturbation’ of the original metric: $g'_{\mu\nu} = g_{\mu\nu} + h_{\mu\nu}$, $|h_{\mu\nu}| \ll 1$. Because of the small magnitude of the perturbation, we can keep only terms linear with respect to it, in the subsequent treatment of the Einstein field equations. This is the linearisation approximation, transforming the Einstein equations to linear ones, and was first attempted by

Einstein, showing that, with this approximation, the resulting gravitational field $h^{\mu\nu}$ obeys the equation

$$\left(-\frac{\partial^2}{\partial t^2} + \nabla^2\right)h^{\mu\nu} = 0 \quad (2)$$

i.e. the wave equation. The simplest solution of equation (2) is a plane wave: a perturbation that propagates homogeneously through space. Using the solutions of equation (2), we can visualize what happens to a system of free particles when they encounter a gravitational wave. In particular, it can be proven that a gravitational wave produces an oscillation of the relative distance between the particles (Schutz, 1984). Moreover, the oscillation is out of phase in the two axes perpendicular to the gravitational wave propagation. In other words, if the wave propagates in the z-direction and encounters a system of particles arranged in the xy-plane, it will make the x and y coordinates of the particles oscillate, but when the relative distance in x is minimum, the relative distance in y is maximum, and vice-versa. (see *Figure 1-1*).

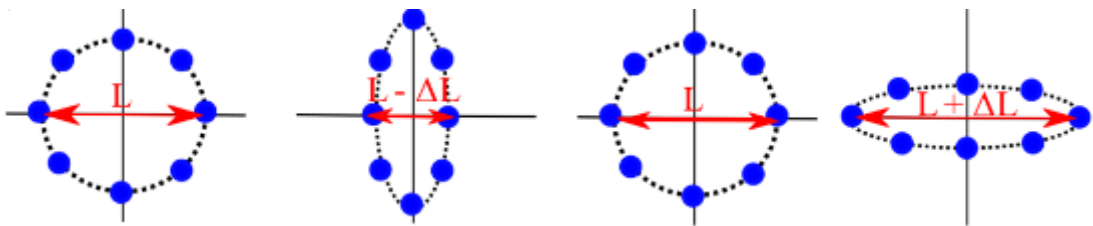


Figure 1-1: The observable effects on a system of masses arranged in a circle, of a gravitational wave that travels perpendicular to the page. (Kokkotas, 2002).

Supposing that a source of gravitational waves has luminosity L_G , (total radiated energy) then the flux F arriving at an observer on earth, at a distance r from the source, will be;

$$F = \frac{L_G}{4\pi r^2} \quad (3)$$

The factor 4π comes from the assumption that most sources do not emit isotropically, but mostly along an axis, which coincides with their axis of rotation. In addition, for a travelling gravitational wave that contains one dominant

frequency component, ω , the relation between F and ΔL (ΔL measures the relative change of metric in a system of test masses, as shown in Figure 1), will be

$$\frac{2\Delta L}{L} = \frac{1}{\omega} \sqrt{\frac{16\pi G}{c^3} F} \quad (4)$$

where $G=6.667 \times 10^{-11} \text{ m}^2\text{kg}^{-1}\text{s}^{-2}$ is the gravitational constant, and c is the velocity of light (Schutz & Ricci, 2010). The values of $\frac{2\Delta L}{L}$ for the most common sources known today are of the order of 10^{-18} m, about one-thousandth the size of a nucleon. Of course, if these are extrapolated over the distances of the commonly known sources, they represent immense amounts of power emitted (Buonanno, 2007, Carroll, 2003).

1.3. Sources of gravitational waves

The sources of gravitational radiation are usually divided in two categories, periodic and aperiodic (Schutz and Ricci, 2010). The periodic sources are those that emit continuously and include all double star binary systems and spinning stars. In fact, the first (indirect) observation of gravitational waves was done by accurate measurements of the change in the orbits of a binary pulsar system. This change in spinning could be exactly explained as due to the energy loss, through emission of gravitational waves. However, the luminosity of these kinds of sources is below the current and near future direct detection limits. With the current detectors, aperiodic sources are always detected: these are one-off events, including all kinds of star collapses, for example supernova explosions (also below the current detection limit), and inspiraling binary systems of black holes and neutron stars that finally coalesce (Schutz, 1996, 1999). Coalescing black holes gave the first detected gravitational wave from the LIGO instrument in 2015 (Abbott et al., 2016a). A significant stochastic background of primordial gravitational radiation is also expected to exist, according to the current theories of cosmology for the creation and evolution of the universe (well below the current detection limit, as well) (Cutler & Thorne, 2001).

1.3.1. Continuous waves

A continuous wave source of gravitational radiation is a source that emits a signal over a long period of time, usually at almost constant frequency. These sources are for the moment hypothetical, since they are very weak, but they are theoretically possible in any case where a non-symmetric mass distribution is subjected to great acceleration. A rotating neutron star (pulsar) that has an asymmetry due to shape, precession or movement of its interior components is expected to emit gravitational waves.

As noted above, the emission of gravitational waves would give a tell-tale alteration of the pulsar frequency (“spindown”). Since the observed spindown rates are quite low, the asymmetries present in the pulsars observed so far cannot be very big. However, there have been glitches (sudden changes) observed in the frequencies of pulsars, which are usually explained as releases of distortions of their crust (Weisberg & Huang, 2003).

The simplest approximation of a deformed pulsar is an ellipsoid, with two principal axes a and b and eccentricity $e = \frac{a-b}{\sqrt{ab}}$. If we denote the moment of inertia of the shape around its rotation axis as I , the total emitted energy (luminosity, L) of radiation can be calculated as:

$$L_G = \frac{288GI^2e^2\omega^6}{45c^2} \quad (5)$$

For known and relatively close pulsars and reasonable assumptions for the eccentricity (based on spindown and glitch observations), we arrive at values of $\frac{2\Delta L}{L} = 10^{-26} - 10^{-28}$. Calculations have shown that some pulsars within the Milky Way should be detectable in the frequency range of 10 to 100Hz.

1.3.2. Binary signal

A binary system is the simplest source theoretically that can emit gravitational radiation: two bodies that move in the gravitational influence of one

another. The signal is created when two bodies with masses m_1 and m_2 rotate in a circle of radius r around their common centre of mass, with angular frequency ω . The emitted gravitational radiation has a luminosity that is calculated as

$$L_G = \frac{32}{5} \frac{G}{c^2} \left(\frac{m_1 m_2}{m_1 + m_2} \right) r^4 \omega^6 \quad (6)$$

If the orbits are not perfect circles, the luminosity is much higher (because of the greater accelerations of the masses involved). The emitted radiation is maximum when the bodies are close to the centre of gravity, and therefore they lose more and more energy at this point, tending to re-circularize the orbits. The radiation also causes the orbits to eventually decay and the masses to collide. This coalescence, or ‘inspiraling’ motion creates gravitational waves with increasing frequency and amplitude until the point of final merging or collision. This ‘chirp’ signal is so characteristic that it can be sought for in detectors by signal matching algorithms, dramatically improving the signal to noise ratio.

Both the strain (relative coordinate change) and timescale of orbit decay can be calculated for an inspiraling system, giving (Schutz & Ricci, 2010):

$$\frac{2\Delta L}{L} \cong 1.02 \times 10^{-23} \left(\frac{m_1 m_2}{m_1 + m_2} \right) (m_1 + m_2)^{\frac{2}{3}} \left(\frac{\omega}{200\pi} \right)^{\frac{2}{3}} \frac{100}{r} \quad (7)$$

with r measured in Mpc, and the masses measured as multiples of the solar mass, and

$$\frac{\omega}{\dot{\omega}} = 7.97 \left(\frac{m_1 m_2}{m_1 + m_2} \right)^{-1} (m_1 + m_2)^{-\frac{2}{3}} \left(\frac{\omega}{200\pi} \right)^{-\frac{8}{3}} \quad (8)$$

Relation (8), for example, when applied with the numerical values of the pulsar system that Hulse and Taylor used to indirectly detect gravitational radiation, shows that they will collide in about 10^8 years. With realistic assumptions of detector sensitivity and coalescence event frequency, about 10 events per year are detectable. However, there are great uncertainties in the event rate.

The coalescing binaries, either pulsars or black holes are therefore the clearest (due to signal shape) and strongest and most frequent signals that gravitational detectors in the near future can expect to see (Abbott et al., 2016b, 2016d). The detection of electromagnetic radiation coming in coincidence with a gravitational wave, as happened for one signal in 2017 was a major breakthrough in the identification of mysterious transient sources of gamma ray radiation (gamma ray bursts). Enough statistics of coalescence signals can also give an independent measurement of the Hubble constant, lifting the tension currently existing between the two different methods of measuring it.

1.3.3. Burst signal

Burst signals are gravitational wave signals that usually are emitted in processes that last for much less than a second. The most usual (known) procedure of the type is a supernova explosion. Supernovae are essentially ‘failed’ stars: Stars that cannot create enough thermal pressure in their interior to act against the gravitational pressure of the external layers, and therefore collapse under their own weight. They are classified in two categories, Type I and II. Typical Type I supernovae are white dwarfs (small, hot stars) that accumulate extra material from some companion star and then collapse under the extra weight. Some of these explosions result in the formation of neutron stars, but never of black holes, since there is not enough mass in the original configuration.

Type II supernovae are the result of the collapse of an extremely massive star and the subsequent shockwave expansion of a shell consisting of the star’s outer layers. Less than 10 supernovae explosions have happened over the past 1000 years in our own galaxy, but it is estimated that one supernova explodes somewhere in the universe once every 2-3 seconds. Most Type II supernovae result in the creation of a neutron star, while the consensus is that many of them end up as black holes. The gravitational waves are emitted from the collapse of the outer shells of the supernova and have a millisecond timescale. A totally symmetric collapse will not emit any gravitational radiation; the more asymmetric, non-spherical movements will give bigger amplitudes of gravitational waves. The original asymmetries and speed of rotation can even result in the star

breaking up during the explosion and the creation of two neutron stars that will then eventually coalesce and merge, as seen in the previous section. The exact calculation of the characteristics of gravitational radiation from supernovae is extremely difficult, since each event is unique and the radiation comes from difficult to model parameters, such as the eccentricity or fluctuations at the time of the explosion. An indicative model of the $\frac{2\Delta L}{L}$ calculation, based on the formula

$$\frac{2\Delta L}{L} \sim \sqrt{\frac{15 \times 10^{-4}}{2\pi} \frac{G}{c^2} \frac{M}{r}} \quad (9)$$

gives a value of 10^{-18} for a possible source that would sit at the centre of the Milky Way, and 10^{-21} for supernovae in the local cluster which contains about 300 galaxies (Schutz & Ricci, 2010).

1.3.4. Stochastic background

The stochastic background of gravitational radiation includes the overlapping radiation from all the sources presented in the previous sections: gravitational collapses, coalescing binaries, and continuous signals from asymmetric pulsars (and any other source not imagined and modelled up to now). Since, as explained above, the interaction of gravitational radiation with the matter and electromagnetic fields of the universe is minimal, the gravitational waves from all these multiple sources are essentially free to propagate around the universe forever. It is not clear at the moment how this stochastic background of gravitational waves can be detected, since it would require exceptionally good uncorrelated noise cancellation in many different detectors operating in parallel (Schutz & Ricci, 2010).

More interesting, though extremely unlikely to be observed directly, is the 'relic' primordial gravitational radiation background, due to cosmological processes close to the big bang (nucleosynthesis). An upper limit can be calculated that gives the maximum energy density contribution to the universe due to primordial gravitational waves: This seems to be less than 10^{-5} of the total energy density of the universe, so there are hopes only for its indirect detection, for the

moment, through its interaction with the cosmic microwave background, for example.

1.4. Gravitational waves detectors

Historically, the direct detection of gravitational waves has been based on two techniques: The resonant detectors, and the interferometric detectors (Riles, 2013, Maggiore, 2014). Resonant gravitational wave detectors were first developed by J. Weber (Weber, 1969). Starting in the early 60's, he showed that a detector of gravitational radiation could be a mass quadrupole harmonic oscillator. The simplest form of this detector is a pair of masses at either ends of a spring. Weber had the idea of constructing this from piezoelectric material, or applying piezoelectric transducers to a metal bar.

Weber constructed two aluminium bar detectors, localised in Maryland and Illinois and started work first on characterising the background and then detecting coincidence events in the two detectors in real time. He reported bursts of gravitational radiation at kHz frequencies, which gave a huge boost in the development of new detectors of the same type, in various institutes in the USSR, Europe and the US. Weber's results were never replicated by any of the other detector groups.

In the 1970s, an improvement of the original resonant gravitational radiation antennas' sensitivity followed the introduction of cryogenic detectors, aiming to operate the resonant detectors at extremely low temperatures, in order to reduce the noise. Some room-temperature detectors and some low-temperature ones continue to operate around the world. The best cryogenic resonant detector has a sensitivity that would barely allow the detection of gravitational waves coming from collapse in our own galaxy (Schutz & Ricci, 2010).

Interferometric detectors all originate from an idea of (Pirani, 1956), who first talked about the possibility of using an electromagnetic wave travelling between test masses to explore the space-time curvature of the region between them (Saulson, 1994; Rakhmanov, 2000). The interferometric gravitational wave

detector design is based on a Michelson interferometer. In this instrument, a special optic configuration called a beam splitter is used to split a light beam in two, which then travel in perpendicular directions - two “arms” of the interferometer (*Figure 1-2*). Mirrors are positioned at the end of the arms, and the light is reflected back to the beam splitter. The two beams recombine on the beam splitter creating an interference pattern, meaning the “highs” and “lows” of the light waves get amplified or negate the effects of one another, depending on the relative phase of the two reflected beams. When a gravitational wave arrives, with a direction of travel that is perpendicular to the plane of the interferometer, one arm dilates by ΔL , while the length of the other is decreased by ΔL . This, in simplified terms, means that the number of full light waves that fit into the distance between the mirror and the beam splitter changes by a bit, and therefore a different phase of the light wave arrives at the beam splitter from each arm. The interference pattern observed is modified (periodically, or in a chirp pattern for binary sources, see above), and the gravitational wave is detected. The amplitude of the interference change and its frequency measure the corresponding values for the gravitational wave that produced the changes.

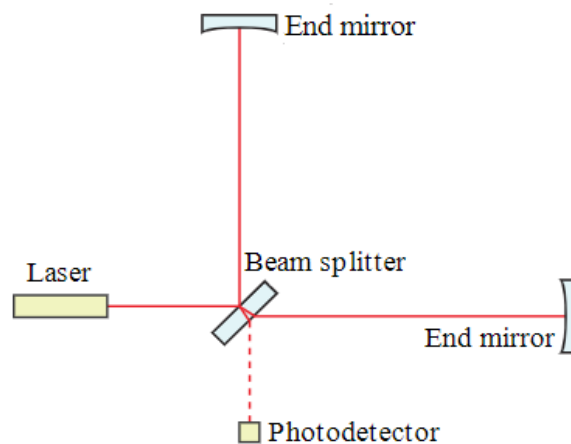


Figure 1-2: Interferometric gravitational wave detector, principle of operation: The Michelson interferometer (Kokkotas, 2002).

Current interferometric detectors in operation include the GEO600, with an arm length of 600m, operating in Hannover, Germany, which has been used mostly as a testbed for the development of technologies relevant to the other more sensitive interferometers. Advanced LIGO (Advanced LIGO team, 2007) and Advanced VIRGO (Virgo Collaboration, 2006) are the only operating

interferometers to have detected gravitational waves (Abbott et al., 2016a). Since late 2018, KAGRA, in Japan (Somiya, 2012), has been added to the existing detectors. It is expected to be one of the first detectors to use cryogenic temperatures.

1.5. Third generation Detectors

The first generation of gravitational detectors consist of Weber's efforts and his mimics' and continuers' ones. The first interferometric detectors are usually designated the 'second generation' of instruments; this led to the first direct detection of gravitational waves from astronomical sources (LIGO collaboration). The biggest development coming in the near future also relates to interferometric detection, and the third generation of detectors will use a variety of improvements to increase the sensitivity or the detected frequency range, and therefore the range of source phenomena observed.

The current Advanced LIGO detector will undergo a first upgrade resulting in a detector that will be called A+. First, 'squeezed light' will be introduced; the photons used will no longer have a random relation between their phase and amplitude, resulting in the reduction of the quantum noise (see next section). Then, a few years later, the strength of the suspensions of the test masses will be increased, and larger masses will be introduced. A less noisy optical coating for the mirrors of the test masses, which is the main topic of this thesis, will also have been identified by then. All this is expected to lead to an ~ 2 times improvement in sensitivity.

The next phase of the LIGO is named 'Voyager' and in this the test masses will be cooled down to 120K, to reduce the thermal noise. Because of this change, all the optics will have to be remanufactured using silicon instead of silica as a base material. This will in turn entail changing the laser frequency, and consequently finding newer coating materials that will work in the new frequency. All this will add another factor of ~ 2 sensitivity compared to the A+ phase. Finally, with a timeline of about 2035, a more speculative upgrade will see the increase

of laser power and increase of the interferometer arm length, giving an extra sensitivity factor of ~ 4 , compared to the previous phase.

A more imminent development will be the addition of a new, Advanced-LIGO-like detector in India, operational around 2020. This detector will improve sky localisation of gravitational wave sources by a factor of about 3. More interferometric detectors are planned for Europe: The Einstein telescope will have a triangle configuration, with two interferometers available for each of the three detectors situated at the triangle's vertices, sensitive to different frequency ranges.

The most impressive development in gravitational wave interferometry will undoubtedly be the Laser Interferometric Space Antenna (LISA), which will be launched around 2030, and will involve three identical spacecraft that will keep station at the vertices of an equilateral triangle with edge length of more than 2 million kilometres. The three vehicles will rotate around the Sun following an earth-like orbit and will contain two laser and two free floating test masses, constituting arms of an interferometer. LISA is not antagonistic to the ground-based detectors, but rather complementary, as the huge arm length of the interferometers will allow it to explore gravitational radiation from totally different sources (LISA experiment collaboration).

1.5.1. Noise Sources

Anything that can distort the interferometer geometry or produce a change in the interference pattern, other than a passing gravitational wave, is considered a source of noise for the gravitational wave detectors. As exposed in the previous section, modern interferometric detectors are able to measure displacements of extremely minute size. A big part of their sensitivities comes from the draconian control over the noise sources. We could crudely divide the noise sources of the interferometer into the ones coming from the intrinsic laser characteristics and operation, and the external noise sources (Edelstein et al., 1978).

The laser light bouncing on a mirror at the end of each interferometer arm, imparts two times its momentum on the mirror. This radiation pressure exerted on the test masses (mirrors) is increased with increasing laser intensity. The radiation pressure is not constant, but fluctuates, and its fluctuations are bigger with increasing intensity of the laser light. This is already a significant noise source for the interferometric detectors, which need a high-enough laser intensity in order for enough light to arrive at the far mirrors.

Moreover, the number of laser light photons returning from each interferometer arm is not constant but also fluctuates following a Poisson distribution, with mean N , and standard deviation \sqrt{N} , for big enough N . This 'shot' noise can hide phase fluctuations and destroy the interference measurements. This kind of noise decreases with increasing laser intensity. Therefore, there is a trade-off between optimisation of the laser intensity between shot noise and radiation pressure noise.

The external noise sources can further be divided into 'gravity-mechanical' and thermal sources of noise. The simplest noise in this category are 'seismic' sources. The mechanical vibrations of the test masses can be due to earthquake activity but also other vibration sources (man-made or natural). These vibrations are reduced with the use of special suspension systems, by hanging the test masses and optical equipment as pendulums. These are very effective at isolating higher frequency vibrations, but not so effective at ones below $\sim 1\text{Hz}$. Even the best suspension systems, though, cannot isolate the interferometer test masses from the gravitational attraction of the matter surrounding them. Low-frequency density variations of the surrounding matter can induce noise that can imitate gravitational waves, and cannot really, effectively be shielded, but they can independently be measured and subtracted from the signal.

Before turning to thermal noise sources, it should be noted that both these kinds of noise, gravity-mechanical and thermal, are effectively suppressed, as a source of false positives, by the decision to operate many identical interferometers situated at a great distance from one another. All the above presented noise sources are expected to be uncorrelated (except in the case of a huge magnitude seismic event) and will differ significantly in the different

locations on Earth where interferometers are operating. The problem with all these kinds of noises is that it will worsen the sensitivity of interferometers significantly.

The thermal noise of the detectors is due to the Brownian motion of the atoms and molecules that constitute the test masses (mirrors) (Saulson, 1990). Since the modern gravitational wave detectors operate at room temperature, this thermal motion of the constituent atoms can be significant (the Brownian motion increases with temperature, and theoretically only ceases to exist at a temperature of absolute zero) (Harry et al. 2002). Furthermore, thermal fluctuations affect all parts of the optical system, from the suspension to the mirrors themselves, inducing vibrations. By affecting the optical coating of the mirrors, thermal noise has two especially important noise manifestations, called ‘thermoelastic’ (changes in the shape, size and position of the coating due to thermal fluctuations), and ‘thermorefractive’ (changes in the optical properties of the coating) noise, respectively.

Thermoelastic noise is the result of the thermal expansion of the coating (or succession of coatings) covering a mirror in a gravitational wave detector (Harry et al. 2002). When there is a homogeneous temperature change, ΔT it will result in a change in the length scale of the material in all its dimensions, Δl , scaling linearly with the coefficient of linear expansion of the material α : $\Delta l = \alpha \Delta T$. The phase difference induced by this change is again linear, $\Delta \varphi = K_{TE} \Delta l$ (only the dimension perpendicular to the laser beam is important as a noise source). However, this simple model is only an approximation, since the temperature changes are not homogeneous, and the different materials of substrate mirror and coatings have different linear expansion coefficients, changing also the optical path of the beam through the whole system.

Thermorefractive noise, on the other hand, is the result of thermal fluctuations of the refractive index (Harry et al. 2002). Thermal fluctuations change the refractive indices, n , of the coating or coatings, causing a phase shift of the reflected light, while there are also changes to the electromagnetic field profile at each boundary between materials, inducing further phase shifts to the laser light beam (Bondu and Vinet, 1995, 1998). As a first approximation, again

we can suppose a linear overall induced phase shift, with the refractive index change: $\Delta\varphi = K_{TR}\Delta n$. Again, this simplified model must take into account real-life complications, like the presence of multiple coatings (and the substrate mirror material) with different K and inhomogeneous temperature differences, for example due to specific beam profiles (areas of the mirror near the centre of the beam are subject to heating due to the action of the beam itself).

More involved calculations of the thermal noise as observed by a beam with a Gaussian profile, with beam radius r_G done by Braginsky et al. (2003), give the spectrum of the thermal noise fluctuations as a function of the reflecting material properties, thermal conductivity θ and heat capacity per volume, C_V , as well as the temperature T :

$$S(\omega) = \frac{2\sqrt{2}k_B T^2}{\pi r_G^2 \sqrt{\theta C_V \omega}} \quad (10)$$

The noise sources presented above for the Advanced LIGO gravitational wave detector are summarised in graphical form presented in *Figure 1-3* below. As is clear from the figure, the coating-induced thermal noise contributes a lot to the overall noise of the detector (Bochner, 1998).

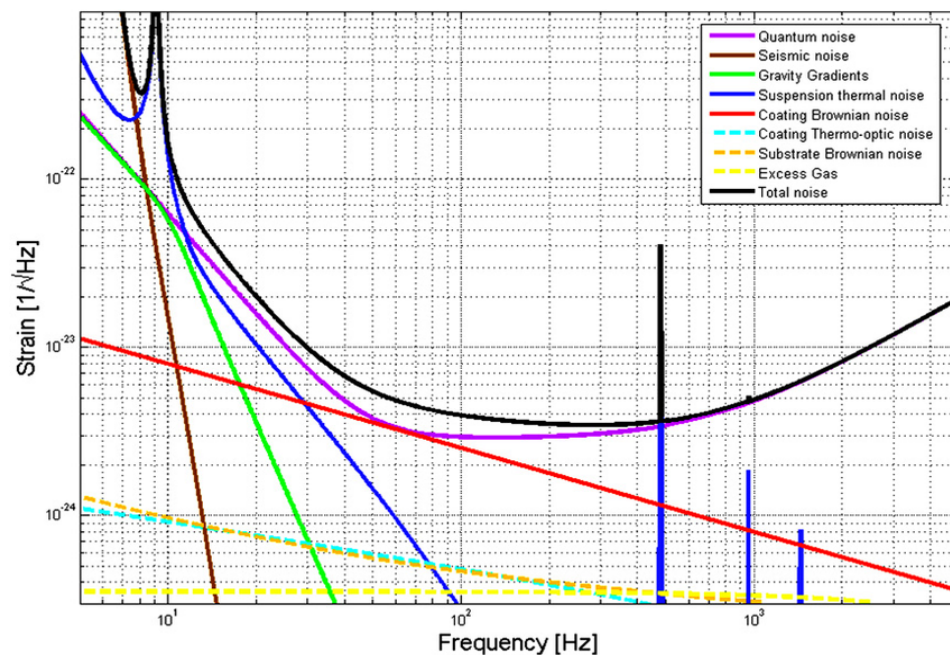


Figure 1-3: Principal noise sources for Advanced LIGO. Quantum noise includes shot noise and intensity fluctuations. Coating Brownian noise is the second most important noise source over much of the detector operating frequencies (Advanced LIGO Collaboration, Instrument Science White Paper).

1.6. Coating for optics

Optical instruments used for scientific research, but also for many everyday applications, make heavy use of specialised optical coatings. The coatings can have multiple functions: they can reduce the reflectance of a surface (or enhance it), they can increase the absorption of light, or they can even selectively transmit some wavelengths and prohibit the passage of others. They can also alter the polarisation of a light beam, or they can be used to divide a light beam into many paths. All the optical components of interferometric gravitational wave detectors presented above, use specialised coatings, in particular dielectric mirror coatings. These are made by stacking films of alternating materials of high and low refractive index. The reflectance of the mirror increases when the number of pairs is increased, and when the relative difference in refractive index of the two layers is increased.

1.6.1. Overall concept-multilayers and material choices

The optical coatings used for the advanced LIGO interferometer includes alternating layers of high refractive index Ta_2O_5 (tantala, tantalum pentoxide) and low refractive index SiO_2 (amorphous silica), both with width ' $\lambda/4$ ', i.e. with a width equal to a quarter of the wavelength of the laser light used. The material were selected because of their low loss and their high dielectric contrast, while the $\lambda/4$ scheme maximizes the reflectivity for a give number of layers. It can be proven that for the $\lambda/4$ coating, the reflectivity, r , at normal incidence is given by

$$r = \frac{1 - n_s \left(\frac{n_1}{n_2}\right)^{2p}}{1 + n_s \left(\frac{n_1}{n_2}\right)^{2p}} \quad (11)$$

where n_s , n_1 and n_2 are the refractive indices of the substrate, coating 1 and 2 respectively, and p is the number of high-low index pairs used (Harry et al. 2002). The substrate used for the test masses is fused silica (Agresti, 2006, Penn, 2003).

The main requirements for the coating materials are low absorption and scattering, stability and low thermal noise. Absorption is mainly produced due to impurities and defects, and non-stoichiometric composition. The initial efforts of interferometric detectors borrowed heavily from existing high-precision laser instruments, like gyroscopes and other interferometers, from where the amorphous tantala-silica alternate sheet structure was adopted. However, for the third-generation interferometers, the currently used scheme is an important factor that does not allow the increase of sensitivity, therefore, many alternative coating compositions and layering schemes are examined.

Among them, Hafnia (HfO_2) seems to have a promising loss angle, but is missing well-defined optical properties as yet. Zirconia (ZrO_2) has shown room temperature mechanical loss that is about ten times lower than tantala, but has also big optical absorption losses and shows high mechanical stress. It is hoped that silica or tantala-doped zirconia will reduce the stress and absorption, while retaining the low mechanical loss. Niobium pentoxide (Nb_2O_5), was rejected also because of its high optical absorption, while TiO_2 - SiO_2 nanolayers, amorphous silicone, silicon nitride are also being extensively tested as regards the noise and absorption profiles [Flaminio 2010]. For future detectors, a bold proposal is to go to full crystalline coatings, where the absorption will be negligible (due to the perfectly known composition and atom arrangement), and the mechanical loss will also be more easily modelled. Of course, to create a defect-free crystal coating that has all the desired optical and mechanical properties and can be easily coupled to a substrate mass is a tall order for current technology.

1.6.2. Mechanical loss and its origin

The thermal noise of the system can be related to the characteristics of mechanical loss in the set of multiple coatings and substrate, using the fluctuation-dissipation theorem (Rao, 2003). The theorem has general application and connects the intensity of random fluctuations in some (macroscopic) variable of a thermodynamic system, to the strength with which this system degree of freedom couples to the microscopic degrees of freedom of the environment of the system. The same coupling to the environment is responsible for the motion

damping of the same variable, and therefore the microscopic thermal fluctuations are proportional to the damping coefficient for the macroscopic movement in the same variable. Applied to the case of coating thermal noise, the theorem explains how the thermal fluctuations of the coating and substrate relates to the mechanical impedance of the same system (the theorem has much more general applications, as it can be used for electrical or fluid systems as well). In turn, the mechanical impedance can be related to material characteristics like the Young's modulus and Poisson's ratio (Penn et al., 2006a, 2006b). Another concept related to the mechanical loss of a coated mirror when impinged on by a laser beam, is the loss angle, φ , of the materials, which quantifies their ability to absorb electromagnetic energy from the incoming beam and transform it to heat (Harry, 2004, Vinet, 2005). In case the oscillation frequencies are much smaller than the resonant frequencies of the system, and also the beam size is much smaller than the size of the mirror, the thermal noise spectrum (intensity versus frequency f) can be found exactly and written using only the mechanical properties of the participating materials:

$$N = \frac{2k_B T}{\sqrt{\pi^3}} \frac{1-\sigma^2}{Y w_m} \left[\varphi_{\text{substrate}}(f) + \frac{1}{\sqrt{\pi}} \frac{d}{w_m} A \varphi_{\text{substrate}}(f) \right] \quad (12)$$

With A given by:

$$A = \frac{Y'^2(1+\sigma)^2(1-2\sigma)^2 + Y^2(1+\sigma')^2(1-2\sigma')}{Y Y' (1-\sigma'^2)(1-\sigma^2)} \quad (13)$$

where Y and Y' are the Young's moduli of the substrate and coating, σ and σ' their Poisson's ratios, d the thickness of the coating, and w_m is related to the beam geometry (Harry et al. 2002). In most experiments, the coating contribution is the largest of the two in (12), because the coating is nearer the surface interacting with the laser, and therefore fluctuations in it are more important, but also because of the different materials that comprise the coating, relative to the substrate.

When an external force is applied to a test mass, the material does not have an instantaneous response back to equilibrium: there is a lag (the system is said to present "structural damping"). This is due to internal variables of the

material such as thermal currents, shifting grain boundaries and moving defects. The vibrational modes of the test masses can be modelled as lightly damped harmonic oscillators:

$$F(\omega) = -kx(1 + i\phi(\omega)) \quad (14)$$

Here, k represents the spring constant and ϕ the phase lag of the system response, x , to the restoring force $F(\omega)$. It is possible to rewrite equation (14) in terms of velocity, v , taking into account the combined effect of internal friction:

$$F(\omega) = i\omega m v - i \frac{k}{\omega} (1 + i\phi(\omega)) v \quad (15)$$

Here, m represents the mass of the test mass. The impedance, $Z(\omega)$, is obtained by dividing equation (15) by the velocity, v . Then the fluctuation dissipation theorem gives:

$$S_x = \frac{4k_b T}{\omega^2} \frac{\omega_0^2 \phi(\omega)}{m(\omega_0^4 \phi(\omega) + (\omega_0^2 - \omega^2)^2)} \text{ per Hz} \quad (16)$$

This clearly shows that to reduce thermal noise and increase the sensitivity, a test mass should be made from materials with low mechanical loss. It can also be seen from (16) that operating at lower temperatures will result in lower thermal noise (as expected), and cryogenic detectors are proposed for the future generation of interferometers.

1.6.3. Characterisation of coatings

The materials used for the coatings of the interferometric detectors are not very well understood, and this is especially true for the Ta_2O_5 component, in its amorphous, thin-film form used for the coatings (Bassiri et al. 2013, Penn, 2003). The developments in this area for the moment come from quasi-random, ‘Edisonian’ researches and observations. For example, it has been observed that doping the high index tantala (Ta_2O_5) with titania (TiO_2) is able to reduce mechanical loss and these coatings have already been implemented in advanced

LIGO. Other studies (Flaminio et al, 2010, Franc, 2009) have, for example explored zirconium dioxide (ZrO_2 , zirconia), and niobium pentoxide (Nb_2O_5). While zirconia has a high refraction index, and small mechanical loss, the stress distribution in the coating (at least with current production techniques) seems too high to allow the consistent production of multiple coatings. Doping it tungsten ($ZrO_2:W$) decreases the stress, but increases the mechanical loss and absorption, while doping with titanium ($ZrO_2:Ti$) improves a bit the mechanical characteristics, but sets the optical absorption higher than the standard, titania-doped tantala. The niobium pentoxide has an even higher refraction index (allowing thinner layers, hence lower mechanical loss), however the absorption is roughly double of the standard and the mechanical properties are similar to it.

Mechanical loss can only be understood if the atomic structure is understood. In order to model the structure correctly, the composition has also to be clarified. The main aim of the present research is to gain accurate information on the composition of the samples that are being studied in the LIGO-Virgo collaboration. The information is used to determine potential candidate compositions for using advanced LIGO mirror coatings, which will then enable detailed studies of film preparation, structure, and properties links. It is also to guide the development of the best next-generation coatings.

In order to better understand the mechanisms behind this improvement, and thereby to further improve coatings, the atomic structure of the coatings is studied, in particular $Ta_2O_5-TiO_2$ and $Ta_2O_5-ZrO_2$. As stressed elsewhere, these stoichiometries seem to optimize high reflectance and low mechanical loss, however, their properties strongly depend on their processing, for example the deposition process and the thermal history (annealing) of the coating. Thus, it is important to explore the exact structure of the finished product in situ. One critical input for any atomic structure modelling is the composition of the coating, and this thesis describes the measurement of the composition of Ta-Ti-O and Zr-Ta-O coatings with unprecedented reliability using Electron Energy Loss Spectroscopy (EELS). To make the result of this research much more reliable, a standard sample of known composition was used for comparisons in each case. For example, in the case of $TiTa_2O_5$, $LiTaO_3$ and $SrTiO_3$ were used as comparison standards while for $ZrTa_2O_5$, $ZrTaO$ and ZrO_2 were used.

1.6.3.1. Layer Thickness

Alternative layer thicknesses have been examined in order to minimize the mechanical loss, and optimize the overall thickness of the coatings, as well as the proportion of coating in them. The first few pairs of coating and the interfaces between them are responsible for the biggest part of absorption and scattering. Hence the plan to separate the first few layers of the coating from the others that will continue touching the substrate using a spacer with small mechanical loss, or even air, with a separation distance that will be an odd multiple of $\lambda/4$. The ' $\lambda/4$ ' scheme maximizes the reflectivity of the coating. At the same time, according to measurements, the total mechanical loss is mostly induced by the coating layers in such a configuration (Penn et al., 2006b). In this way the reflectivity will be retained, but most of the thermal noise (from most of the coating and the substrate), will not reach the first coatings, and hence the reflected beam. A similar idea is to use a material with low absorption but high loss in the first few layers, and low-loss high-absorption material in the back (Agresti et al, 2016, Villar et al, 2010). Different ideas have examined the employment of layers with thickness that departs the usual $\lambda/4$ scheme, always in order to reduce the mechanical loss. For this reason, it was proposed to use a pair of thin high-mechanical loss material and increase the thickness of the low-loss one, maintaining the reflectance but improving the thermal noise. Also, a nano-layer structure, where the high-loss material is applied in films that have nanometre-scale thickness, has been explored, with the added advantage that these layers can withstand higher treatment temperatures (Castaldi *et al.*, 2007, Principe *et al*, 2008). The aim always is to improve or keep the same the optical characteristics of the coating, while minimizing the mechanical loss. There is no clear guidance from theory, and the search for new materials is quasi-random ("Edisonian") as explained in the next section.

1.6.3.2. Atomic structure

The atomic structure of the amorphous materials used for coating has been studied both theoretically and experimentally (Nowick & Berry, 1972). Fused (amorphous) silica, which also constitutes the material of the mirror substrates

and the low-index part of the coating pairs, has been studied more extensively than any other similar material (Fine et al., 1954), and the study of tantalum, titania, zirconia and other materials borrow heavily from the studies in silica. The mechanical loss of tantalum thin films has been studied across a range of temperatures, in order to extract the characteristic dissipation peaks that would allow understanding of the underlying mechanism. However, these were changing not only with stoichiometry but also with different treatment and preparation techniques. It was observed that titania doping changes the form of the dissipation peak of tantalum, making it shorter and wider. The activation energy associated with these peaks in tantalum are comparable to the ones observed in silica, and therefore atomic transitions of similar scale are expected to be involved in the two materials, which would in principle simplify the modelling of the material such as *Figure 1-4*.

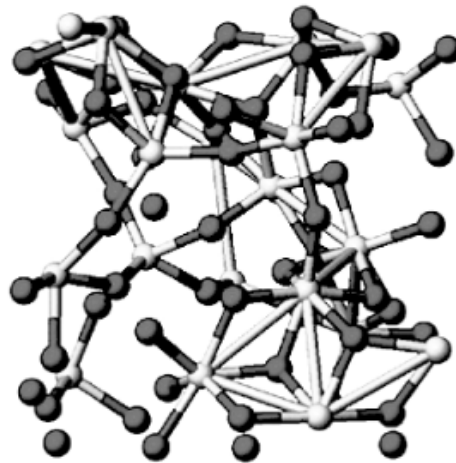


Figure 1-4: Predicted structure of Tantalum pentoxide (light spheres are Ta atoms, dark ones are O atoms) (Reid & Martin, 2006)

Molecular dynamics calculations started with the study of silica (Penn et al, 2003, Weidersich et al., 2000), but have recently also been applied to tantalum, and titania-doped tantalum (Bassiri et al. 2016) (Martin et al, 2008, 2009). These support the idea that the mechanical dissipation processes are dominated by the medium range structure, and especially a ring-like structure composed by 10-20 atoms. This explains in part why the mechanical loss properties are so sensitive to processing starting from deposition techniques and including annealing and polishing (Reid & Martin, 2006). These simulations are complicated by the fact that stoichiometry does not give the full picture of the material. Moreover, the

future plans to run the experiment at reduced temperatures, and even at extreme cryogenic temperatures in future upgrades should be taken into consideration, as this could also change the structure of the materials used. Furthermore, the laser light frequency could also change in a future upgrade of the detectors, or in planned detectors, necessitating another rethink of the refractive index requirements. There seem to be no corresponding molecular dynamics studies for zirconia or doped zirconia yet, although the similarity of the atom size and crystal structure allows to assume that it will be similar to SiO_2 (Yu et al, 2009).

1.6.3.3. Chemistry and characterisation techniques

Chemistry and modelling are unable to adequately characterise the materials applied for coatings. This is due to absence of a simple theory for amorphous materials that can describe them coherently, in the same way for crystalline materials. Apart from that, the best optical properties are many times optimised via doping, hence altering the stoichiometry or annealing (thermal treating at high temperatures) that alters the structure, wherein material modelling turns to be even more fraught (Hamdan et al., 2014). Typically, low-frequency losses in amorphous dielectrics are linked with low energy excitations that are modelled via two-level systems. In precise, atoms comprising of amorphous material are connected with bonds with two minimum energy configurations, along with similar minima that can 'flop' from the one to the other. In ambient temperatures, these 'flop' degrees of freedom are thermally activated, with probable peaks at certain temperature, which reflects the characteristic of the two-level system. The complication derives from the fact that real materials have distribution of 'floppable' bonds between varied atoms that compose them, thus the total 'internal friction' (mechanical loss) of a material comes from a weighted average of their contributions (Trinastic et al., 2016). Molecular dynamic simulations, including dozens of varied atoms in configurations that are extended to nm scales, have only recently been made possible in supercomputers. A recent success refers to the numerical simulation-based 'prediction' that the loss in tantala is minimised upon increment of doping with titania.

Chemistry characterisation of coating is crucial, despite the challenges, such as comprehending the effects of coating and annealing processes on glass film. The conventional EELS quantification route has been well-described by Egerton (2011). But, this does struggle with weak signals, overlapping edges and oscillatory background shapes. Hence, several procedures have been proposed in the attempt of overcoming such challenge, such as modelling the spectra through cross-section shapes and background fitting (Verbeeck et al., 2006; Verbeeck & Van Aert, 2004). Nevertheless, background perturbations and inaccuracy remain in the cross-sections. Bobynko et al., (2015) demonstrated that the EELS signal that derives from a precipitate within a thin steel specimen could be separated from its surrounding matrix using DualEELS spectrum imaging (SI). As for the approach of SI, electron probe is scanned over a defined area of the specimen, in order to record one or more spectrum/spectra at every pixel (Jeanguillaume & Colliex, 1989). The DualEELS method applies an electrostatic drift tube, electrostatic deflector and rapid electrostatic shutter in order to concurrently record low- and core-loss regions of the EELS spectrum at every pixel (Scott et al., 2008; Gubbens et al., 2010). After splicing low- and high-loss spectra areas at every pixel in the SI, followed by Fourier-logarithmic deconvolution to reduce multiple scattering (Anderson, 1998), single scattering dispersions can be retrieved. In order to quantify such spectrum images, standard materials of well-known chemistry were used to provide standard spectra to fit against using multiple linear least squares (MLLS) fitting. Craven et al., (2016) developed a method that extracted absolute energy differential cross-sections from standards, in that case for precipitates in steels. The current work extends this approach to the quantification of Ta-Ti-O and Ta-Zr-O glasses.

1.7. Conclusion

Gravitational waves, either alone or in combination with other astronomical techniques are a powerful window to some of the most extreme phenomena of the cosmos. The interferometric gravitational wave detectors that helped in their discovery, are also the instrument of choice for their detection in the decades to come - most existing and planned detectors, are of this type.

Interferometric detectors are based on the Michelson interferometer, and consist of two perpendicular arms (measuring kilometres) at the end of which are suspended the 'test masses': massive mirrors that bounce back a laser beam split in two at the junction point of the two arms, and sent down them. The recombination of the reflected beams creates an interference pattern that is disturbed with passing gravitational waves. Major noise contributions from fluctuations in the mirrors can mask the signal.

Mirror reflecting coating development is an important avenue to maximize the performance of the interferometric detectors. The coatings have to combine good optical characteristics (high reflectance, low absorbance) with mechanical ones (ultimately connected to their thermal fluctuations, via the fluctuation-dissipation theorem). Predicting coating characteristics from chemistry and stoichiometry is still in its infancy, hence the need for careful characterisation, using, among other techniques, electron energy-loss spectroscopy and electron microscopy, as presented in the next chapter.

2. Instrumentation and Sample Preparation

2.1. Principle of STEM

Electron microscopy allows the visualisation of structures much smaller than those that can be resolved by a conventional light microscope. The main limit of the resolution of a conventional microscope comes from the wavelength of the light used: Typically, a microscope is not able to examine structure that are smaller than the wavelength of visible light. However, with the development of quantum mechanics, it was realised that particles have a dual character - particle and wave. Their wavelength depends on their energy, and therefore it can be controlled by controlling their energy. An optic telescope's lenses manipulate light (bend and focus it); in the same way, electrons can be manipulated (accelerated, to give them a small enough wavelength, and focused) by electric and magnetic fields. Therefore by using electrons, a new kind of microscope can be created, that can see smaller scales. The highest the energy of the electrons, the smaller their wavelength is, and they can resolve structures of smaller dimension. The resolution limit of an electron microscope comes then from the highest energy that the electrons can have before damaging the material that we want imaged. Electron microscopy has contributed a lot to biological and material sciences since its conception (Ahn, 2004).

The electron beam that passes through the specimen undergoes several interactions including elastic and inelastic scattering, backscattering, simple transmission, x-ray emission, etc. All these interactions can be used to obtain information about the atoms of which the sample consists, and their specific arrangement in the sample.

Two main types of electron microscopes exist, the transmission electron microscope (TEM) and the scanning transmission electron microscope (STEM). In a transmission electron microscope, the sample is examined with the use of a broad, with respect to the crystal lattice, fixed, parallel beam. The resulting image is a diffraction pattern made from the electrons, originating from the whole sample.

In the scanning transmission electron microscope, the electron beam is scanned over the surface of the sample in a grid pattern. In this case the electron beam is focused to a minute spot and the result is a series of images, or spectrum information from a series of regions on the sample (Ahn, 2004).

The TEM and STEM are essentially the same system, but with reversed optics: the optics that are situated before the sample in a TEM are equivalent to the optics found after the sample in a STEM. The electron source of the STEM is equivalent to a single pixel of the TEM image (Egerton, 2016).

2.1.1. Optical arrangement

An electron microscope consists of an electron source (the generator of the “matter waves”), a system of magnetic lenses that direct and focus the electron beam, a specimen holder and subsequent lenses that provide the magnification. Of course, the electron beam, following interactions with the specimen and after magnification manipulations, has to be converted to an optical image, which is performed with a suitable electron detector (Egerton, 2016) (*Figure 2-1*).

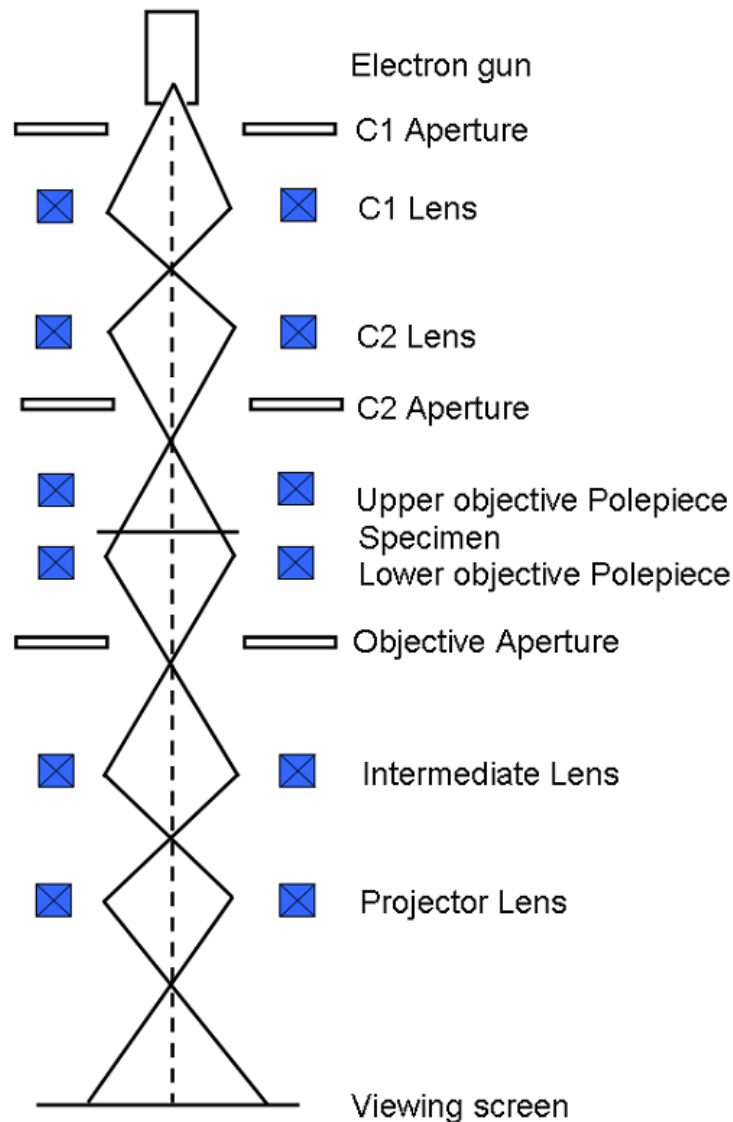


Figure 2-1 : A schematic representation of an electron microscope. Operating in a high vacuum chamber to allow unimpeded electron motion, the flow of electrons and successive focusing actions are shown simply by straight lines. Apertures are used to help remove stray, unfocused electrons and increase contrast (Ahn, 2004).

The sources of electrons used in an electron microscope can be thermionic or field emission sources ('field emission guns'). The thermionic sources eject electrons from a heated material, while the FE ones use a large electric field between a material and an anode to coax electrons out of it. Thermionic emitters operate based on the principle that heating up a material gives it energy which is distributed (also) in its electrons, and therefore some of them acquire enough

energy to overcome the barrier presented by the material edge (encoded through the 'work function', an energy characteristic for each material). Low work function materials are selected for thermionic emitters. On the other hand, the field emitters' principle of operation is the fact that electric fields are extremely amplified near sharp edges and points. Field emitters consist of 'needles' that are given a very fine tip, less than 5nm, and operated in high vacuum. Electrons from the tip of the needle are accelerated in the extreme electric field in their environment and again are able to overcome the work function of the material. Field emitters can be cold-type (operated at room temperature but high vacuum), or thermal-type (called Schottky gun), where the tip of the needle is kept at higher temperature (Luo, 2016).

The detector sits on the other end of the electron microscope and is where the image (from scanning or diffraction) of the specimen is formed and observed. A viewing screen, formed by a simple planed doped with a fluorescent material, is the simplest possible detector. Electrons impinging on it produce visible light, which can be observed by the naked eye. However, most if not all electron microscopes nowadays are equipped with detectors consisting of charged-coupled devices (CCDs). CCDs are pixelated devices; each pixel generates charge that is proportional to the intensity of the radiation it receives. This charge can be stored until the device is read out. Then, the charge from each individual pixel is collected and registered, and an intensity picture can be formed, that covers the whole viewing surface. To detect electrons, the CCDs are covered with another material (scintillator) that emits light when electrons impinge on it. In this way, the electron intensity is converted to photon intensity and then to charge, in each individual pixel.

Alternative detectors are utilised for STEM microscopy, where the readout speed of CCDs presents a disadvantage. A system of scintillator and photomultiplier, or a semiconductor detector can be used in this case. The usual arrangement of detectors for STEM imaging is shown in *Figure 2-2*.

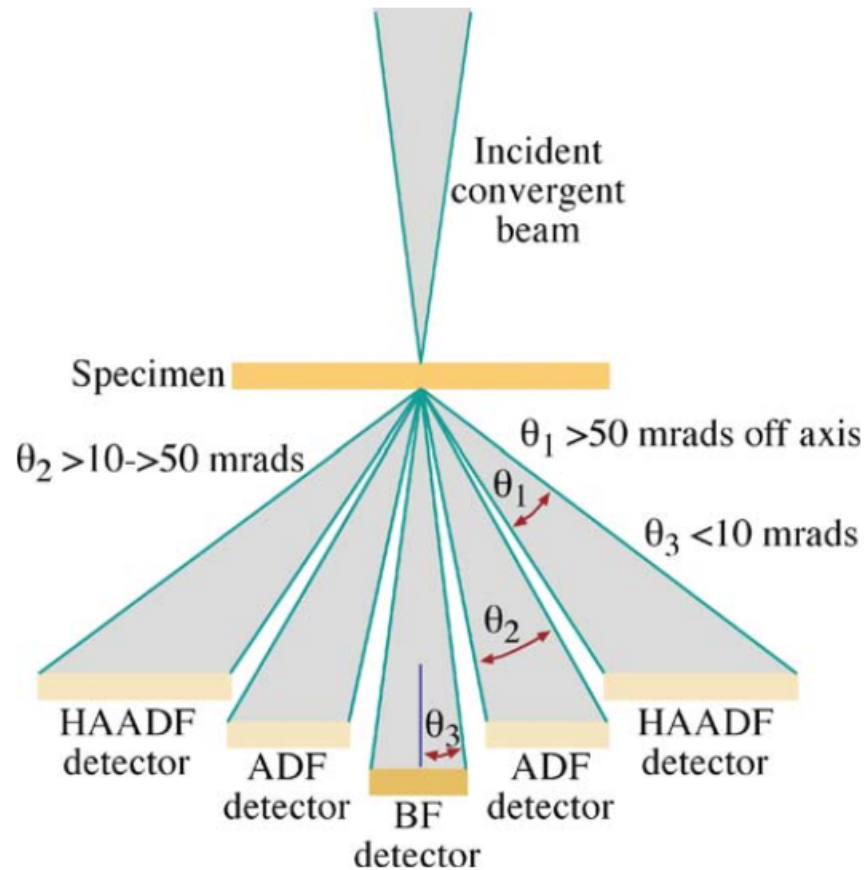


Figure 2-2: Detector arrangement for a STEM (Williams & Carter, 2009)

In a bright-field detector (BF) the intensity of the direct beam of electrons is used to image the specimen. The annular dark-field (ADF) detector uses electrons scattered at low angles from the sample to form images, while the high-angle annular dark-field detector (HAADF) uses electrons that are scattered to even higher angles.

2.1.2. Lenses

The lenses of an electron microscope are electromagnets of various configurations, with the simplest being a lens exhibiting cylindrical symmetry, creating a magnetic field with dynamic lines that lie parallel to the axis of the cylinder. These are equivalent to convex lenses in a classic optical microscope, and the same relations and formulas are still valid for electromagnetic lenses as for the optical ones, for example, the focal length f is given by

$$\frac{1}{f} = \frac{1}{u} + \frac{1}{v} \quad (17)$$

where u is the distance of the object and v that of the image. The magnification is given by

$$M = \frac{-v}{u} \quad (18)$$

A schematic of such a lens, consisting of a magnetic material formed into a hollow cylinder with a gap, and a wound copper coil that carries the field-producing current is shown in *Figure 2-3* (Williams and Carter, 2009, Egerton, 2016).

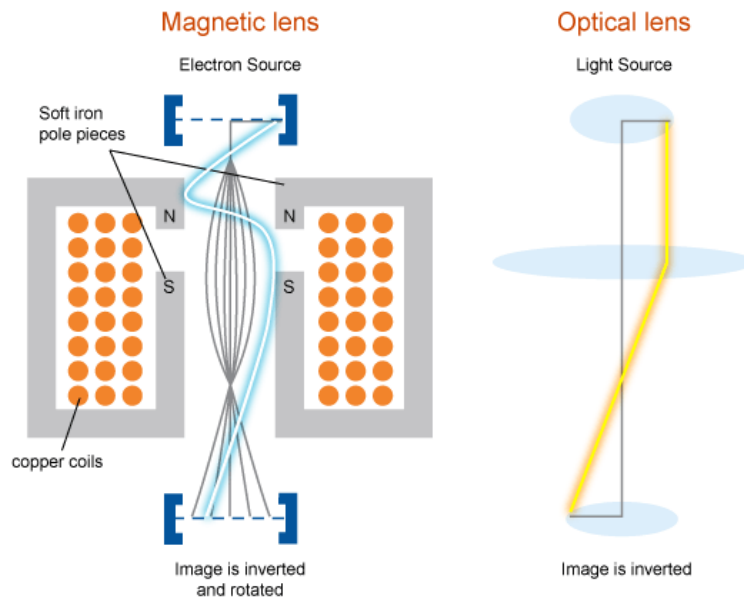


Figure 2-3: Schematic of a magnetic lens in cross-section, the major building block of an electron microscope; comparison with optical (converging) lens (University of Sydney, microscope. training, 2012)

The lenses that are found just after the electron gun constitute the condenser system, that defines the illumination of the sample. Typically, there are two condenser lenses in the system. The first one is used to build a demagnified image of the gun, therefore trying to reduce the electron source to a point. The focus point of the first lens is the object of the second condenser. The second lens can be controlled to create either a parallel beam or a spot

focussed beam at the level of the specimen holder. The first condenser lens controls the size of the probe. There is an interplay between spot size and angle of the electron beam, therefore there can either be large spot size and intense electron beam or small spot size and low intensity beam (because the high-angle electrons are lost at beam forming apertures) (Egerton, 2016, Luo 2016).

The lenses that come after the specimen form the imaging system of the microscope. The most important of them in the after-specimen optics, is the objective lens, which focuses the rays leaving the specimen. The objective creates an image of the diffraction pattern in the back focal plane of the lens, and an image of the specimen a bit downwards in the telescope column. Another lens then focuses either the image of the sample or the diffraction pattern, and other lenses down the column magnify these images and project them on the detectors.

2.1.3. Scanning

In STEM instruments, special coils are used to move the beam around on the specimen plane, thus 'scanning' the beam spot on it. The electronic detector that receives the image at the bottom of the column is usually connected to a computer that synthesizes the images from each spot (knowing the scanning coils' configuration at each moment), and produces the final image. The image is thus more slowly formed than for the case of TEM, and this can result in drift and spatial distortions.

As explained above, STEM imaging can use both bright-field (direct beam illumination), or dark-field (scattered beam or tilted beam illumination) imaging detectors. The intensity of the image in an annular dark field image is related to the atomic number of the atoms imaged and the number of them participating in the scattering (i.e. related the thickness of the specimen and its composition). This is because low angle scattering in the position of the ADF area is due mostly to (low-angle) Rutherford scattering of electrons of the beam from nuclei. It has also been shown that in HAADF (high-angle scattering) images, the contrast is almost proportional to Z^2 , instead of Z , as in the case of ADF. In STEM, the use of annular detectors has also 'freed up' the very-low-angle scattered electrons -

those almost collinear with the original beam, to perform electron energy loss spectrometry EELS. This technique allows elemental analysis in specific spots of the specimen, while it is imaged (Luo, 2016).

2.2. Overview of the Microscopes used in this Work

Two different instruments were used to perform the work presented in this thesis. The FEI Tecnai T20 TEM microscope was used for coarse TEM and STEM study of the materials, and then the JEOL ARM 200F was utilised for a more detailed characterisation of the samples, including electron energy-loss spectrographic studies. The basic characteristics of the two instruments are presented in the following sections.

2.2.1. The FEI Tecnai T20

The FEI Tecnai T20 microscope provides most standard imaging methods with simple processing software and a user-friendly interface. The microscope employs a LaB₆ filament as an electron source, with a subsequent accelerating voltage of 200kV. The instrument can therefore be useful in the visualisation of the structure of various materials (metals, ceramics, biological specimens) exhibiting moderately high resolution and different magnifications. The T20 can be operated as a conventional TEM. It is one of the instruments used in the research of the atomic structure of the coating materials. A simplified schematic diagram of the microscope is in *Figure 2-4*.

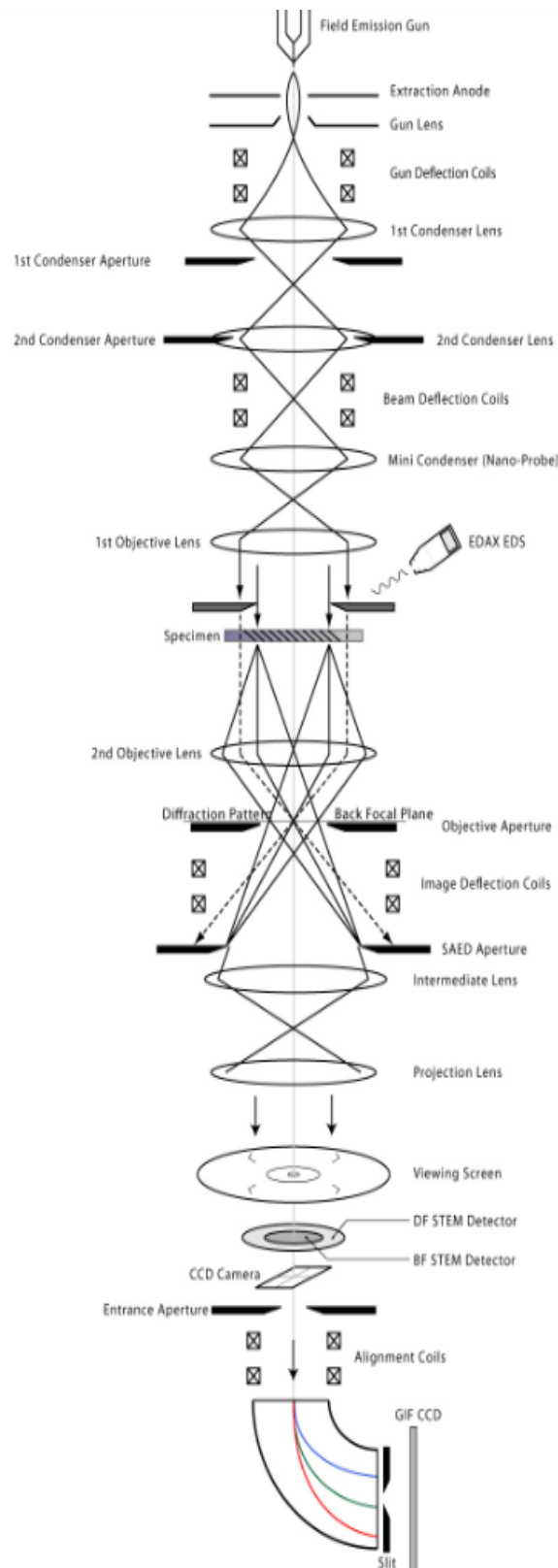


Figure 2-4: Schematic diagram of the FEI Tecnai T20 TEM (Portland State U., TEM Operating manual, 2010).

The TEM uses two condenser lenses for greater accuracy in the control of the electron beam. It includes a Soft Imaging System (SIS) Megaview III CCD camera retractable through a side slot, with large dynamic range and sensitivity that can

be used to collect diffraction patterns which has high dynamic range and high sensitivity, and is used to collect diffraction patterns for atomic composition analyses. At the bottom of the column, there is a Gatan Image Filter (GIF) CCD with the capability to record EEL spectra, using a slit and a system of quadrupole and sextupole lenses, providing dispersion control and energy filtering. The GIF CCD is used for EEL spectra registration of the coating samples.

2.2.2. The ARM

The JEOL ARM 200F is a high-end TEM/STEM using cold field emission gun as an electron source. The instrument is probe-corrected and allows STEM-based images with minimum resolution of approximately 0.6Å. This is inclusive of Bruker X-ray detector, as well as Gatan and JEOL imaging detectors. Electron source with high brightness demonstrates massive electron current per area solid angle that concentrates on minute region. This particularly suits spectroscopic assessments that allow atomic resolution spectroscopy, which is a state-of-the-art instrument with exceptional stability and very high resolution.

The EELS system, which is placed at the bottom of the column, consists of Gatan GIF Quantum ERS with an intrinsic spectrometer resolution of 0.04eV. This is capable of dual and fast EELS. The spectrometer has an EDXS system (JEOL Centurio EDX detector) to perform compositional analysis. The probe corrector, which is a sextupole DCOR, relieves all axial aberrations up to fourth order semi-automatically, apart from reducing astigmatism. The TEM can be operated at 30, 60, 80, and 200 kV to generate electrons that are near monochromatic, with an energy spread of 0.27 eV. As for the TEM mode, the microscope can achieve magnifications from 50x to 2,000,000x, while in STEM mode, it can magnify from 200x to 150,000,000x.

The experimental works carried out in this study employed JEOL ARM200F equipped with Gatan GIF Quantum ER EELS spectrometer and cold Field Emission Gun for rapid DualEELS. The conditions of standard acquisition reflect STEM mode that applies 29 mrad convergence angle and 2 cm specially prepared camera length (Craven et al., 2017), which offers almost constant 36 mrad acceptance

angle for 0-3 keV loss range, upon usage with 2.5 mm spectrometer entrance aperture.

Most data were retrieved with the gun lens set at around 600 pA of current. Some lower loss spectral data were recorded as SIs, when the spectra were generated from several hundred or thousand individual spectra, including correction for energy alignment and single channel defects (e.g., random X-ray spikes). A CCD of 5x1 binning at ‘high speed’ was applied to record the data, especially for noisy scenario and high-loss data acquisition. In this case, several spectra can be gathered and assessed while scanning the beam over a small box (a few nm), with a few seconds of exposure time.

2.2.3. Electron lenses and aberrations

An electron that moves inside a combined electric and magnetic field is subject to forces that in general modify its trajectory and its speed. The combined electric and magnetic forces are known as the Lorentz force, given by:

$$\mathbf{F} = \mathbf{F}_E + \mathbf{F}_B = -e(\mathbf{E} + \mathbf{v} \times \mathbf{B}) \quad (19)$$

where bold symbols are used for the vectors of force (\mathbf{F}), velocity (\mathbf{v}), electric and magnetic fields (\mathbf{E} and \mathbf{B}), e is the charge of the electron and “ \times ” is the external product. According to Newton’s second law, the equation of motion for charges in static electric and magnetic fields is given by the differential equation:

$$m\ddot{\mathbf{r}} = -e(\mathbf{E} + \mathbf{v} \times \mathbf{B}) \quad (20)$$

with m the mass of the electron and $\ddot{\mathbf{r}}$ its position vector’s second derivative with respect to time. In principle, following this equation we could describe the movements of an electron beam passing through any configuration of static electric and magnetic fields precisely. In practice, since the electric and magnetic fields inside a microscope are not precisely described (they include measurement errors, for example), and also the integration of the above equation is complicated, for complex static fields configurations, simplifications and

numerical methods are heavily used to predict an electron beam's behaviour in the instrument (Groves, 2005).

2.2.3.1. Electromagnetic lenses

The simplest electromagnetic lens encountered in an electronic microscope is one that creates a constant magnetic field within it. It is usually called “pole piece (dipole)”, and consists of a magnetic material form with cylindrical symmetry and a central hole (the “bore”) in the middle, around which current-bearing coils are wound. This configuration generates a gradually changing magnetic field in the bore of the pole piece, with a total strength proportional to the current that passes in the coils, and a configuration that makes it totally parallel to the bore axis in the middle of the bore and gradually deviating towards the bore walls. Electrons that travel close to the axis of the bore, travel in lines almost parallel to the magnetic field there, and therefore experience no force (the external product of \mathbf{v} and \mathbf{B} is zero, and there is no \mathbf{E}). On the contrary, electrons that pass further from the symmetry axis will experience a force that is bigger the further away they are from the axis. This will result in their deviation towards the axis (in practice, they will move in helices of diminishing radius around the axis), and hence, the ‘focusing’ effect of the magnetic lens (Groves, 2005).

The above analysis is of course highly simplified, and the ideal magnetic field configurations are idealised, in order to simplify the mathematical treatment. In reality, the imperfections in the pole piece construction, but also the physics of the pole piece magnetic field itself gives rise to perturbations in the electrons’ trajectories. Following the optics terminology, these are called ‘aberrations’, and in order to correct or alleviate their effects, more kinds of lenses are used in a modern electron telescope. These consist of the same general idea (a cylinder-like form with a central borehole and wound coils to generate the magnetic field), but differ in two basic aspects. First, the symmetry is no more cylindrical, but 4-fold, 6-fold or 8-fold and combinations thereof (and the lenses are named quadrupoles, sextupoles, octupoles... etc.). Second, while the magnetic

field in the dipole magnet is mostly parallel to the electrons' velocity, in the multipole ones it is mostly perpendicular to it (Carter & Williams, 2016).

2.2.3.2. Defects of electromagnetic lenses – Aberrations

In analyses of systems of optical lenses (optical microscopes, telescopes, binoculars), there are always some simplifying assumptions, that allow the extraction of simple and practical formulas. In practice, these are accompanied by calculations of inescapable deviations from the ideal (aberrations). These are connected with both the lens characteristics (the ideal description stands for “thin” lenses, for rays “close enough” to the axis and parallel), and the beam characteristics (the ideal is a monochromatic beam, of a single frequency). Aberrations in magnetic lenses follow the same general characterisation, and therefore we have geometric aberrations (connected to construction), and chromatic aberrations (connecting to the spread in electron velocities).

Spherical aberration in magnetic lenses arises from the magnetic field component that is not parallel to the bore axis, in a dipole magnet. This is bigger the further away from the axis, and therefore influences electrons coming parallel to the axis, but further away from it more than the ones moving parallel, but close to the bore axis. This means that the former will be ‘focused’ in a different point than the latter, and the resulting image will be blurred. The phenomenon of spherical aberration can be removed by placing an aperture (circular diaphragm in the periphery of the beam) to totally cut out electrons away from the axis (losing beam intensity). Alternatively, it can be improved by making the magnetic field much stronger, so that the focus point is closer to the lens, and the relative differences in focal length do not matter much (which then means that we will need more lenses overall) (Groves, 2005).

Astigmatism is an aberration caused by a non-axisymmetric magnetic field. This can happen due to errors in construction of the borehole, the selection of the magnetic material, errors in the wounding of the coils, or even impurities accumulated in the borehole or anywhere in the dipole. The focal distance of all electrons will coincide, however the focal point will move on the plane

perpendicular to the beam, forming a characteristic ellipse of an image. Astigmatism is usually corrected using a quadrupole lens, in practice overcompensating the magnetic field where is reduced, and vice-versa (Williams & Carter, 2009).

Coma aberration is also connected to geometric defects of the focusing system; in particular, in a beam that does not follow the axial symmetry of the dipole bore, but travels at a slight angle to it. This creates multiple images of the focused beam (again due to travelling through regions of varying magnetic field strength), that resemble a comet tail. This defect requires careful alignment of the electron production and acceleration system and the optical components of the microscope (Luo, 2016).

Chromatic aberration is the result of the different speed with which the electrons are travelling through the system. In optical systems, chromatic aberration arises from light that contains many frequencies, resulting in photons that have different energies, and therefore “see” different refractive indexes in the optic materials. In magnetic lenses, the electrons that take on the role of optic rays can also have multiple energies, either due to their production and acceleration system, or due to their (inelastic) interaction with the lens materials, the apertures, or the imaged specimen itself. Again, the different energies result in different focusing spots and blurry imaging (Groves, 2005).

2.2.4. Image resolution and aberration correction

In both optical and electron microscopes, the main performance criterion is the instrument resolution. The resolution refers to the shortest distance that can be image using the instrument. A formal treatment of the resolution defines it as the distance, d , between two point scatterers (i.e. two bright points in the specimen), that produce, through the instrument, an image of two points, with the central brightness falling to 75% of the peak brightness (so that can be distinguished as two points and not as an extended object). In this so-called Rayleigh criterion, d is calculated according to

$$d = 1.22\lambda/\alpha \quad (21)$$

where λ is the wavelength of the photons or electrons, and α is the half-angle of the beam impinging on the specimen. The resolution is improved by minimizing d : either decreasing λ or increasing α (which can be achieved by increasing the aperture) see *Figure 2-5*.

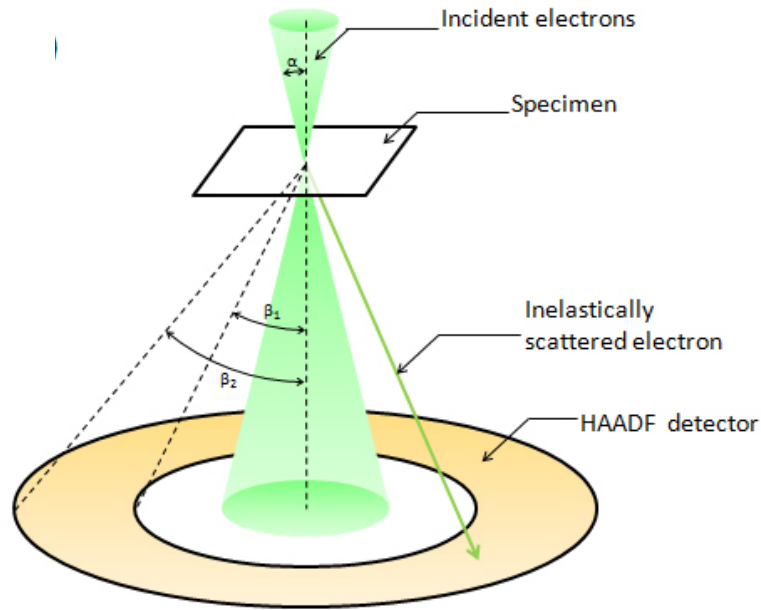


Figure 2-5: Schematic defining the incoming beam half-angle α (and the collection half-angles β_1 , β_2) (From jeol.co.jp, Glossary of TEM terms)

In practice, decreasing the λ of the electrons means increasing their energy: there is a limit up to which this can be done, since very energetic electrons will destroy the specimen before it is imaged adequately. On the other hand, increasing the aperture much will increase the geometric aberration effects, as has been analysed above. Therefore, there is an optimisation to be done between diffraction effects and spherical aberration effects. In fact, there is a third limiting factor, related to the source size: idealised microscope analyses represent the electrons starting from a single point in space, while in reality the source of electrons is extended in space. The simplest treatment of these three resolution-limiting sources adds their effects in quadrature, resulting in a formula that will guide the optimisation that resembles:

$$d = \sqrt{d_{source}^2 + d_{diffraction}^2 + d_{aberration}^2} = \sqrt{\frac{A}{\alpha^2} + \frac{B\lambda}{\alpha} + C\alpha^3} \quad (22)$$

with A, B, C appropriate constants, λ the wavelength and α the angular aperture as above.

The chromatic aberration, on the other hand, can be optimised by minimizing the energy spread, ΔE , of the initial electron beam. This is done by using newer, cold-field emission and Schottky-type sources, the use of energy filters/monochromators, or the combination of the two (Goodman, 1968, Carter & Williams, 2016).

2.3. The FIB

The Focused Ion Beam (FIB) is a method for specimen analysis, inspired by the working principle of the electron microscope. Essentially, the FIB is an electron microscope that uses ions instead of electrons. These are accelerated by a voltage difference and focused on a small spot of the specimen under investigation. The ions, due to their higher mass, disrupt and modify the structure of the specimen, while at the same time they eject other ions and electrons belonging to the specimen, that can be analysed to extract information about the specimen.

Most FIB instruments use gallium ions, which are created with a tungsten needle immersed in a liquid gallium reservoir (gallium is used exactly because it is a high-enough atomic number material that is liquid in normal conditions). The needle includes cone-shaped channels, and when a potential is applied to the reservoir, the liquid is drawn into them and arrives at the tip of the needle, where the field value is multiplied due to the shape. A liquid gallium needle is formed that extend beyond the tungsten tip, and has a diameter of about 2nm. This extremely small tip amplifies the field even more and causes the ionisation of gallium atoms and their emission from the tip and acceleration.

The intensity of the ion beam can be controlled: low currents are useful for TEM-like imaging, while high currents allow manipulation of the sample. Ions hitting the surface of the specimen transfer momentum to its atoms, and if the transfer is high enough then they can liberate them from the sample, and induce “sputtering”. The liberated atoms are free to move away from the sample surface (ablated). Alternatively, they can be displaced around in the sample bulk. The ion beam also creates lots of electrons, which can also have imaging uses. The ions, being much heavier than electrons, can induce significant damage on a surface easily, however, their penetrating power in the bulk of the sample is reduced to a few nm. Using FIB techniques, samples can be prepared for TEM and STEM imaging, creating extremely thin specimen from bulk materials (Yao, 2007).

2.4. Sample Preparation

Many methods can be used to prepare a sample for TEM studies. The most important factor common in all of the methods is that the final specimen has to be thin enough to be transparent to electrons. In the case of the specimens prepared in Glasgow, ion milling with a Gatan PIPS 1 was used as a conventional method, but most of the specimens were prepared by the focused ion beam (FIB) method. The FIB method allowed the choosing of the desired area with higher precision, together with optimisation of time required to prepare single specimen from a bulk. These methods are described in more detail in the next sections.

Each analysis technique requires different and well-standardised shapes and dimensions of specimens. All mechanical and thermal analysis techniques require bulk samples with dimensions and shapes as defined by testing standards. For optical studies on a scanning electron microscopy, the best metallographic sample is a polished and etched surface. In case of transmission electron microscopy the sample demands are much more sophisticated, because the specimen has to be transparent for electrons and contain a representative sample of the material under investigation, with no or minimal alteration of the structure by the preparation technique. Thus, the thickness of the sample should be in the range 10-80nm and the diameter of sample or its supporting mount less than 3mm.

Ideally, the sample should be stable under electron irradiation, have parallel sides, and be non-magnetic; or if composed of ferrous materials, the sample should be very thin and small in volume to minimise any effect of the magnetic induction in the sample on the electron beam.

Each method has advantages and disadvantages: some are more automated and consistent, while others require more intervention by highly skilled technicians, and the results depend on many difficult to control factors. Some techniques, like carbon replica and FIB have greater danger of introducing artefacts and changing the characteristics of the sample to be imaged. Therefore, the selection of technique depends on the available technical manpower and instruments, the material to be imaged, and the specific properties that need to be measured from it (Wang, 2013).

2.4.1. Specimen for TEM

The coatings evaluated in this study were 500nm-thick layers of tantalum (tantalum pentoxide), as well as titanium- and zirconium-doped tantalum, which were deposited on amorphous fused silica discs with 10 mm thickness and 25.4 mm diameter. In order to be transparent to TEM electrons, crystalline materials have to be generally less than 100 nm thick. Amorphous materials, on the other hand, have to be less than 40 nm thick. The specific thickness required for electron transparency relies on the accelerating voltage of the instrument, the composition of the specimen, and its structure. The electrons can be 'channelled' in a periodic and crystalline structure, hence the usage of thicker crystalline specimens. Most specimens used in this study were prepared via conventional cross-section method, while some applied the Focused Ion Beam (FIB) Lift-out technique method. Both methods will be discussed in the next section.

2.4.1.1. Conventional cross-section method

Initially, the samples were attached with wax to a standard optical microscope slide, made of glass, with the coated face on the glass. The

attachment was performed to protect the coating while cutting the samples. A diamond circular saw was used to cut the sample disks in two semi-circular pieces, working from the side opposite of the glass slide (and the coating).

A 2 mm-width section was cut along the diameter of one of these sections, which created roughly a parallelogram that measured 25.4 x 2 mm. The bulk of the substrate was removed, first by cutting and then by grinding, to reduce its thickness to about 500 nm. The thickness of 2 x 25.4 mm parallelogram was about 1 μ m, with half of it being substrate and the rest consisting of coating material. This section was cut into half, and the two halves were glued together, with the coating sides touching by using some epoxy resin. The half-sections of a molybdenum rod were fitted on either side of the resulting section. Next, the whole configuration was inserted into a brass tube with a layer of epoxy resin. The epoxy was cured for ~1hr at 130 °C, and the whole system was cut with a diamond circular saw into 500 μ m thick discs. The disks were ground down to ~80 μ m thickness.

A Gatan Dimpler was implemented to create 'dimples' on both sides of the resulting disks by using a rotating copper wheel that had varied diamond paste grades as the grinding material. Two missing hemispherical regions were created by the dimpler on two sides of the sample disk, with a central "bridge" of the material that included coatings with 20 μ m thickness.

The final step employed the Gatan Precision Ion Polishing System (PIPS) that used ions to further grind the area of the disk close to the centre, down to a thickness of about 10 nm. The system used dual argon ion beams with 4 keV energy, and a 4-degree incidence normal to the disc surface, with a final polish pass using 0.5 keV ions, in order to reduce remaining roughness and to maximise the electron transparent region. Acetone, chloroform, and ethanol were applied at all steps to clean the sample. Figure 11 illustrates the varied implemented stages. *Figure 2-6* illustrates the varied implemented stages.



Figure 2-6: The final stages of TEM sample preparation steps using the cross-section technique: From left to right, Coating-to-coating gluing, enclosure in molybdenum and copper, dimpling with dimpler, and ion polishing (Hart, 2017)

The study samples were also prepared by using the FIB technique that allowed the production of micron-scale specimens with uniform thickness and can be taken from specific sites on the bulk sample. Initially, platinum or gold is deposited on the raw sample, with most of the material around the area of interest removed. Next, the area of interest is cut out and lifted from the material bulk. It is mounted onto an Omniprobe grid, and then again FIB is used to thin it and clean it. A drawback of this technique is the potential for structural change and chemical interaction of Gallium ions used with the material, including the formation of ‘destruction zone’ due to ion interactions that can extend maybe tens of nanometres inside the sample. Similar issues may occur due to the final ion milling polishing of the cross-section prepared sample. This shows that the impacts of both methods are insignificant for this analysis.

2.4.1.2. FIB lift-out method

Apart from controlling the parallelism of specimen sides and preserving good quality to allow a range of analyses, the FIB approach is more rapid than other conventional techniques. Only a small amount of magnetic materials and ferrous steels (excluded from this research) are required in the FIB approach because conventionally-prepared specimens in vast quantity may lead to significant magnetic deflections of electrons, while small amount of specimen has no effect on beam for FIB method. One drawback of FIB, similar to other methods, is the damages imposed on the specimens and artefacts formation. Hence, ion damage and ion implantation may incur on the sidewalls and surface. However,

the extent of damages and artefacts rely on incident energy, ion species, material density, incidence angle, and material bonding/structure. Discarding the artefact is vital to prepare apt samples for microscopy with high resolution.

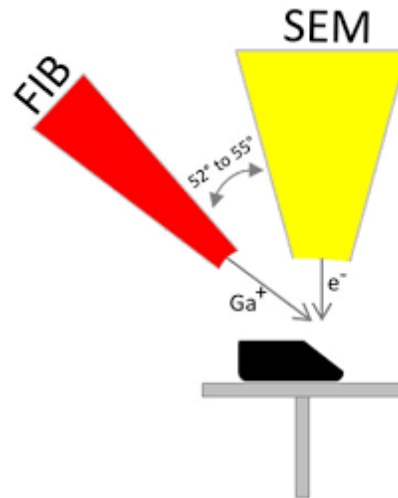


Figure 2-7: Scheme of columns in DualBeam FIB (Kizilyaprak et al., 2014)

This study combined FEI Nova 200 DualBeam FIB system with Scanning Electron Microscopy (SEM) and FIB columns in a single tool. Some vital FIB elements refer to SEM column at 52° to ion column, Sidewinder FIB column (permits formation of small ion probes down to 2 or 1 keV energy), main chamber with sample holder (can be moved in x, y and z directions and tilted up to 52°), Omniprobe 100 micromanipulator (can be slotted into the main chamber on the opposite side to ion column to lift out small specimens), and a gas injection source (GIS) needle positioned between electron and ion columns. The GIS deposits a metal layer (commonly Platinum [Pt]) to protect surface of material from damages incurred by ion beam while thinning the cross-section sample of STEM. During FIB lift out, GIS is attached to the sample holder, thus placed next to the sample ($\sim 150 \mu\text{m}$ above the sample). The sample is liberated and deposited on the surface after heating GIS nozzle. Typically, the needle is linked with Pt-carbonyl gas in the crucible. Upon insertion of GIS, the side of electron column becomes $150 \mu\text{m}$, while the tip becomes $50 \mu\text{m}$ at the side of ion column for deposition of Pt. displays the scheme. Interaction between gas and Gallium ion (Ga^+) leads to breakage of Pt-carbonyl chemical bond, hence Pt deposition on the surface. The vacuum system discards carbonyl gas residue to avoid milling by Ga^+ to protect the surface during FIB lift-out method.

Protection was provided to the sample by evaporating about 30 nm gold for several minutes via Emitech (Quorum) sputter coater at 20 - 25 mA. for a few minutes. In this sputtering technique, which is called physical vapour deposition (PVD) technique, the atoms are transferred from a specified conducting target for deposition on the substrate surface. A DC magnetron is employed by the sputtering source through use of strong magnetic and electrical fields in order to confine the plasma particles that have been charged nearer to the sputter target surface. The argon sputtering gas enhances the frequency of ionising collision, which results in a coating range of almost 360 °. The specimen is placed on a rotating platform in order to generate a conducting film with high insulation across the sample. This particular step of pre-fabrication was adopted because the oxides (with thick insulation) on the specimen surface led to excessive and frequent sample charging under FIB, hence the beam drift cannot be handled. One drawback of this method is that some parts of the sample may be damaged due to accidental milling. Despite its ability to mitigate charging, metallic coating may be intricate while preparing sample. For instance, the essential surface features may be unseen upon coating, thus the need to pay closer attention to lift-out region at pre-coating and coating thickness.

After the specimen has been coated with gold, a rectangular (10 μm x 2 μm) first electron (400-500 nm), and followed by ion beam platinum (~2 μm), are deposited to the target extraction area. A deposition of an electron beam platinum layer (5 keV, 1.6 nA) is performed prior to deposition of thicker ion beam platinum (30 keV, 1nA) to minimise implantation of Gallium in the specimen surface. Next, 30 kV Ga⁺ is used to cut trenches at the front and back of the deposited platinum when the stage is tilted at 52°. The longer the specimen, the higher chances the specimen has to warp or break under the beam due to thinning, and the more challenging to attach to the grid for electron microscopy analysis. After determining that the trenches are sufficiently deep, the sample is tilted to 7°, wherein the bottom, one whole side, and a fraction of the other side are discarded. Now, using the deposition of ion beam platinum, the sample can be attached to a probe tip. After that, the sample is cut and separated from the bulk to be manipulated and micro-welded to TEM Omniprobe™ lift-out grid via FIB platinum metal deposition. The probe is cut and final thinning (5 kV, Ga⁺) is

carried out to attain a sample thickness of < 100 nm. The specimen is now ready for STEM analysis, as illustrated in *Figure 2-8*.

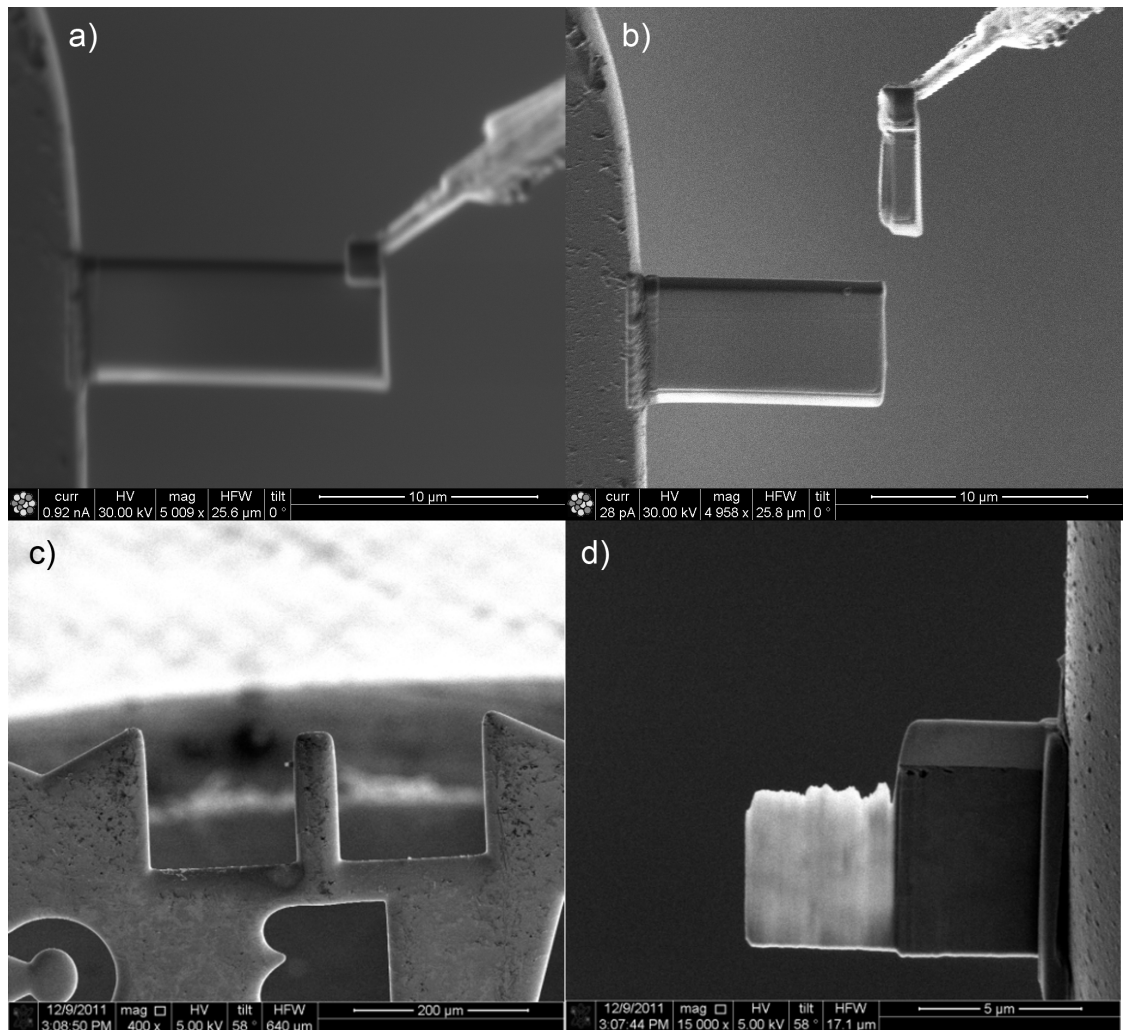


Figure 2-8: Specimen attached to the Omniprobe grid a) before b) after separation of the micro manipulator, c) the Omniprobe holder with specimen on the left B holder seen with 400x magnification with electron source, d) specimen after thinning from both sides. Photos were acquired during standard specimen preparation session.

(Joana, 2017)

It is very challenging to fabricate a specimen and at the same time maintaining its thickness at 100 nm. However, this process is made possible via FIB only at manual operation throughout the procedure. Such complete manual procedure, which excludes automatic trench cutting, milling, and tilting, is time consuming to obtain a lift-out specimen from the bulk.

Upon successful lifting, grid attachment, and thinning, the specimen undergoes a thickness check via Tecnai T20 Transmission Electron Microscope, prior to further analysis with JEOL ARM 200F Scanning Transmission Microscope.

2.5. Electron Energy Loss Spectroscopy

As explained in previous sections, a lot of potential information comes from the interaction of high-energy electron with the specimen in an electron microscope. On top of the diffraction pattern or the magnified image of the specimen, one can take advantage of the X-rays, interacted primary electrons or even secondary electrons to get more details of the specimen under study. Electron energy-loss spectroscopy studies the inelastically scattered electrons that have interacted in the spot position illuminated during the raster scan of a STEM, and gives information about the composition of the sample in this particular spot.

The EELS refers to energy distribution analysis amidst mono-energetic electrons that travel through sample with <100 nm thickness. Internal structure information and interactions within the sample can be retrieved by placing the beam that has been transmitted in a spectrometer. Events that depict loss of energy reveal much information about a sample, such as electronic structure, thickness, valence state, and chemical fingerprint. The electrons are classified into two groups upon exiting a sample: (1) nil energy loss, and (2) scattered and possess lower energy than the incident electron beam. Electrons that are not scattered, as well as those scattered elastically, have zero loss peak while the other electrons lose energy during excitation process in the specimen. Nonetheless, it is impossible to gather all scattered electrons via EELS analysis due to geometrical shortcoming. *Figure 2-9* portrays two angles that must be weighed in to determine the scattered electrons gathered in spectrometer. Turning to this study, DualEELS datasets had been retrieved from GIF Quantum ER with spectrometer acceptance and probe convergence angles at 36 and 29 mrad, respectively. α refers to convergence semi-angle that is retrieved from microscopy setting, particularly aperture and condenser lens. β represents collection semi-

angle that is obtained from camera length, objective and spectrometer entrance apertures, as well as tool mechanical setting.

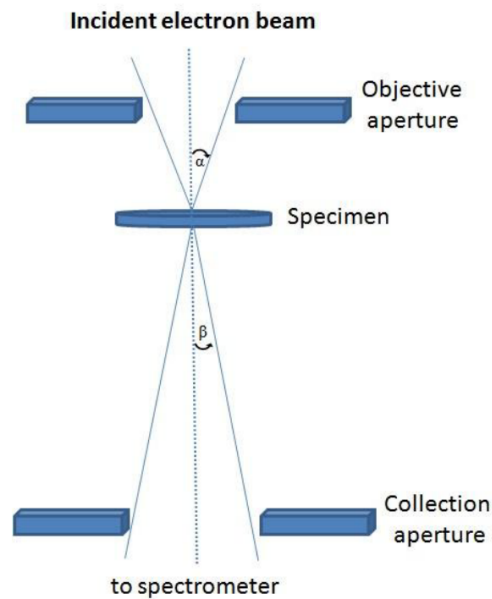


Figure 2-9: Definitions of α and β in (S)TEM showing α , the convergence semi-angle and β , the collection semi-angle.

2.5.1. Interaction of Electrons with the Sample

The TEM assesses interaction between thin sample and uniformity of energetic electron beam. Upon entering solid, the electrons interact with specimen atoms via electrostatic force (Coulomb) (Egerton, 2011), hence the scatter of incident electrons. Apart from experiencing momenta change, indirectly transmitted electrons can be inelastic (massive transfer of energy from electron to atom) or elastic (trivial energy transfer). *Figure 2-10* illustrates the connection between specimen and electron beam.

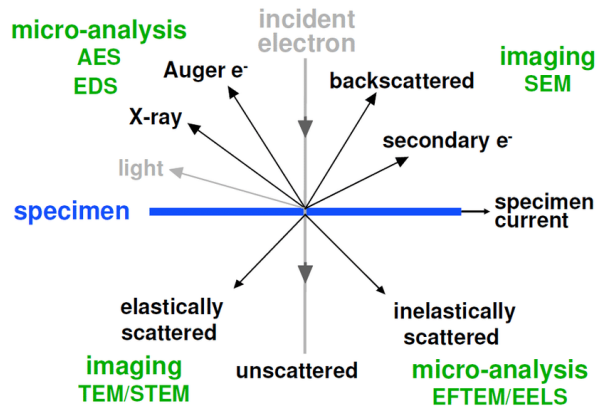


Figure 2-10: Synopsis of possible electron-specimen interactions (Tran, 2017).

Electrons scattered in inelastic way lose energy during interaction, while those scattered elastically do not lose energy and repel from the real path by the sample atoms as they adhere to Bragg's Law:

$$n\lambda = 2d \sin \theta \quad (22)$$

where n refers to positive integer, d reflects distance of interplanar, θ denotes scattered angle, and λ represents incident wavelength. Incidents scattered by similar atomic spacing are also scattered by similar angle. Crystalline and thin sample commonly offers coherently elastic scatter. With integral charge concentration in the tiny atomic nucleus confines, huge angle deflection occurs when incident electron beam gets closer to the nucleus (Carter 2009). This occurrence is called Rutherford scattering (see *Figure 2-11a*), which was initiated in 1911 by Ernest Rutherford while assessing alpha particles scattering that led to the conception of atom model, hence the Bohr model. He also described deflection of electron by $> 90^\circ$ that derive from the specimen surface that it entered, thus known as Rutherford backscattering (see *Figure 2-11a*). Nonetheless, this reflects a fraction of electrons scattered elastically. Dielectric screening in specimens with sound conduction band electrons concentration can weaken the electrostatic field of nucleus when the electron travels away from the centre of atom, in adherence to inverse square law. Thus, more electrons are scattered at miniscule angles ($0-10^\circ$) (Carter, 2009). The interaction in crystalline solid between electrons that are scattered can modify the endless scattered

intensity dispersion into one, reflected by peaked angles that refer to spacing in atoms. Such elastic scatter is known as diffraction.

Coulomb interaction defines inelastic scatter between atomic and incident electrons that surround the nucleus. Initially, the interaction between inner shell electron and rapid incoming electron is weighed in, shown in *Figure 2-11b* (promotion of electron into Bohr orbit at higher quantum number) or in *Figure 2-11c* (higher energy level). The inner shell electron has ground-state energy that can hold hundreds of electron volts under the solid's level of Fermi.

In order to be dissociated from the ground state, the electron should absorb incoming electron energy that is equivalent to or bigger than the binding energy, hence generating an upward trajectory above Fermi level into an unoccupied state. Hence, the rapid incoming electrons are scattered through an angle of some mrad, as energy is given to the inner shell electron. Interaction between elements is characterised by inelastic energy loss experienced by incident electrons. Since the energy is unique for every bonding of elements (see *Figure 2-12*, such energy can extract bonding and compositional information, such as oxidation state, in the assessed sample region. Inelastic scattered electrons can thus be used for Electron Energy Loss Spectroscopy (EELS). The process of de-excitation generates kinetic energy to other atomic electron or results in X-ray liberation, especially after the outer shell electron transitions down to the core hole left behind.

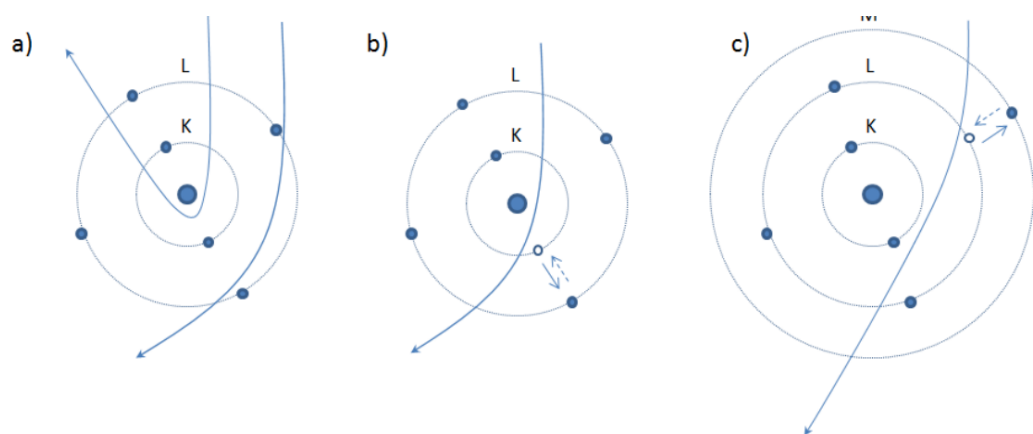


Figure 2-11: A particle view of electron scattering. a) Elastic scattering that is caused by Coulomb attraction by the nucleus. Coulomb repulsion leads to inelastic scattering in b) Inner- and c) Outer- shell electrons that are excited to higher energy level

Plasma resonance reflects the interaction between outer-shell electrons and the collective effect of many solid atoms, and not mere single electron. It is represented in longitudinal wave and the plasmon energy ranges from 5 to 30 eV. The ability of sharing energy among the electrons is vital for plasmon excitation and can be attained in delocalised state, but not for atomic core level.

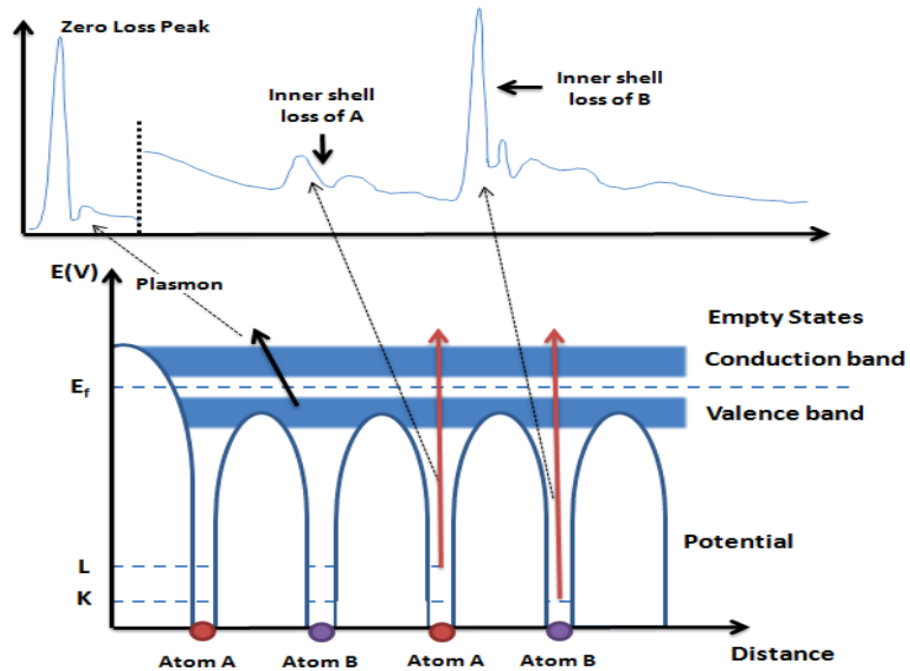


Figure 2-12: Schematic illustration of energy-loss spectrum and the generation of energy-loss peaks

This thesis probed into the reliable quantification of film coating, thus the significance of comprehending the transitions that take place within interatomic so as to accurately interpret the energy spectra arrived at, though not discussed elaborately here. Rich information about the tested specimen can be retrieved from chemical fingerprint, including high-loss (electron movement between specimen atoms and inner-shell electrons) and low-loss information (plasmonic interaction).

2.5.1.1. Elastic scattering

Elastic scattering can happen either on the electron cloud of an atom, resulting in a small angle deviation ($1-2^0$), or on the nucleus of the atom, resulting in large deviation, up to 180^0 (backscattering). Small angle scattering from crystalline materials is affected by the periodic arrangement of their atoms (diffraction) and depends on the incidence angle of the electrons with respect to the atom arrangements. This is coherent low-angle scattering, with the main characteristic being that the electrons do not lose energy during these processes. At higher angles, elastic scattering happens incoherently, but always with no energy loss. These are also due to the nucleus, and their probability, and the resulting scattered electron intensity, depending on the atomic number Z of the participating atoms.

2.5.1.2. Inelastic scattering

Inelastic Scattering refers to electron scattering that is accompanied by energy loss in the specimen. This energy loss can be caused by numerous reasons, including generation of X-rays, ejection of Auger electrons from inner atom shells, ejection of secondary electrons (from valence, outer shells), or scattering from collective electromagnetic (plasmons) or acoustic (phonons) excitations of the specimen atoms. The ejection of secondary electrons is characterised by the energy loss and emission angle of the ejecta, which can be collected and analysed in an electron spectrometer, incorporated in the microscope (Brydson, 2001).

2.5.2. Electron energy-loss spectrometer

Figure 2-13 below shows a schematic of the Gatan Quantum ER spectrometer used in this research. It includes a gradient magnetic prism, excited by two electric coils. The electron drift tube has direct connection to the microscope vacuum system. This alters the kinetic energy of the electrons, in order to shift the spectrum position on the detector CCD. The spectrometer bends the electrons at a right angle: The Lorentz force that the electrons feel inside the magnetic prism, bends the electron trajectories of different velocities (energies).

This causes the electrons of different energies to emerge from the spectrometer at different angles. Seven dodecapoles focus and correct the aberrations of the emerging electrons, and then they are directed towards the detectors.

The main limitations of the instrument come from the energy spread, ΔE of the initial beam of electrons, the intrinsic energy resolution of the spectrometer, and the camera resolution (Ahn, 2004). A diagram representing the EEL spectrometer used in this study is explained in *Figure 2-13*.

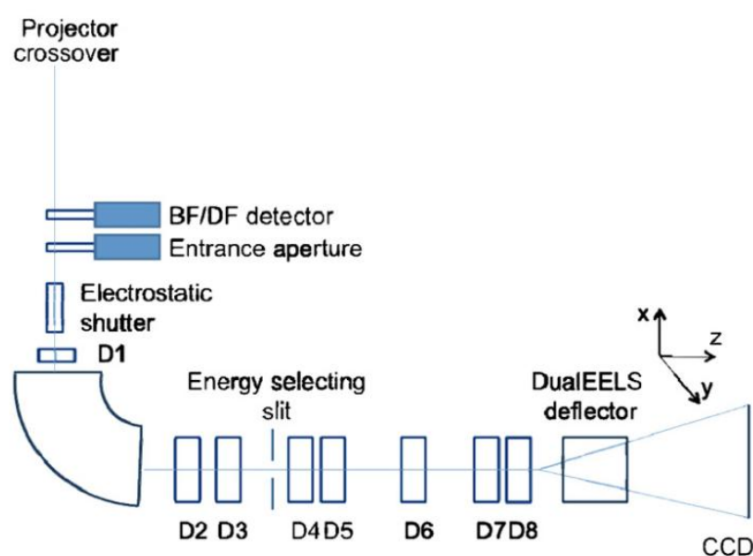


Figure 2-13: Schematic diagram of the EEL spectrometer used in this study (Bobyanko, 2018).

2.5.3. EELS

The inelastically scattered electrons produce the electron energy-loss spectrum, with the intensity as a function of energy loss. The EELS is composed of two regions, called the low-loss region and the core-loss region.

The low-loss region is the region from 0-50eV. Its most prominent characteristic is the zero-loss peak (ZLP), that is created by the electrons that are transmitted without any scattering and therefore without any energy loss at all. The intensity of the ZLP includes also electrons that have small losses, below the resolution of the magnetic prism (these are mainly scattered by phonons, and lose

10-100meV). The FWHM of the ZLP is an indicator of the energy resolution of the instrument and usually take values of about 1-2 eV *Figure 2-14*.

After the ZLP, there are small peaks that come from scattering on plasmons, i.e. collective oscillations of the valence electrons. The plasmon peaks are well defined and intense for metallic materials. In insulators and semiconductors, there are broad, less intense plasmon peaks. In this low-loss area, there may exist more peaks due to transitions from the valence to the conduction bands.

The core-loss region includes energies from 50eV to 2-3keV. Its extend is limited by the intensity level of the signal at high energies, i.e. by how many electrons take part in extremely high energy loss interactions in the specimen. The intensity at 2keV can be eight orders of magnitude less than that at the ZLP. This region is mostly interesting for elemental characterisation of the studied material, since it shows ionisation edges, coming from the excitation of electrons occupying inner shells of the atoms to states above the Fermi level. The ionisation signals are edges and not peaks, since a little extra energy is always provided to the escaping electrons. The edges sit upon a falling background caused by excitation events at lower energy loss.

The edges' nomenclature follows the standard spectroscopic notation, depending on the initial shell of origin for the excited electron. The leading edge energy of every edge gives the binding energy of the particular electron shell, which has a characteristic value for every atom. A typical EEL energy spectrum is shown in *Figure 2-14*. Therefore, the EELS can be used to study the atomic composition of the specimen, or even, in STEM mode, in a particular spot on the specimen ("Spectrum Imaging, see next section). Moreover, the fine structure of a given edge contains information about the atom environment inside the sample, i.e. its neighbouring atoms and the kind of bonding it has with them. Finally, the edge intensity gives hints about the stoichiometry of the specific atom in the studied sample (Luo, 2016).

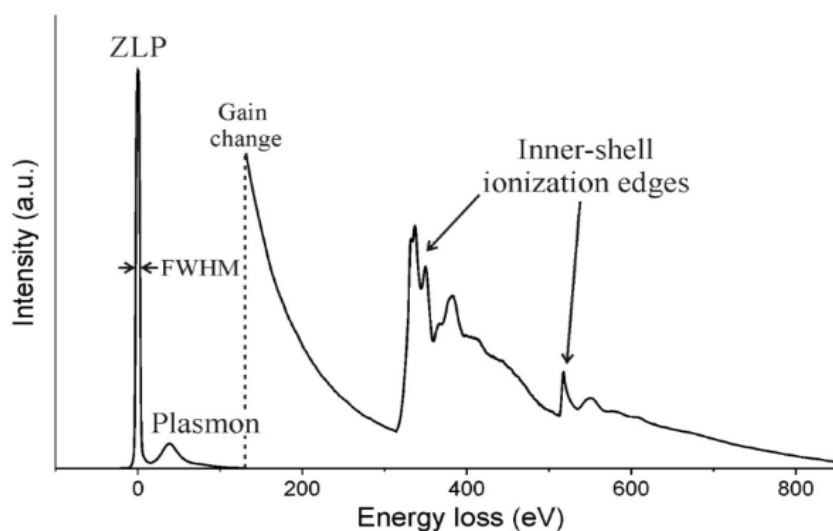


Figure 2-14: An EEL spectrum, showing the principal characteristics (Williams and Carter, 2009).

2.5.4. Dual Electron Energy Loss Spectroscopy (DualEELS)

Chemical, electronic, compositional, and physical aspects of a specimen can be obtained from EELS. Despite the availability of dynamic electron detectors, determining core- and low-loss areas in EELS spectra under identical electron-optical criterion is still a challenging task. This is attributable to high intensity of zero-loss that seems to be a common occurrence for a range of magnitude orders, which is higher than that for weak ionisation edges of interest.

Higher-speed acquisition can be obtained for low- and core-loss spectra via DualEELS application, as recording both spectra concurrently has several benefits, such as: (1) the ability to capture a comprehensive picture of energy loss in the sample, (2) removal of energy shift to allow accurate chemical shift measurements, (3) performance of absolute quantification, (4) accurate determination of specimen thickness, (5) the ability to deconvolve plural scattering, and (6) the ability to correlate low-loss signal with core-loss feature (e.g., plasmonic and band gap). This enables one to apply advanced quantification routines, apart from precisely determining energy shifts.

The DualEELS, which was initiated by Scott et al., (2008), refers to a system that incorporates apt hardware and rapid electrostatic shutter managed by extra scripts found in the spectrum imaging application. For the first time, this system permits one to record all EELS spectra at each pixel in SI, inclusive of image detector signals and X-ray spectra. In fact, recent spectrometers have embedded fast mapping that suggests 1000 spectra per second (Gubben et al., 2010) which permits mapping of hundreds of nm within a few minutes at low nm resolution. Such rapid recording of spectra eases analyses that include a massive and dynamic range of EELS data.

Prior studies have employed EELS to assess the oxidation of zirconium alloys, in which quantification has been limited to k-factor semi-quantitative technique that excludes multiple scatters in a sample (Ni et al., 2011). Past analyses neither mapped larger regions of metal and oxide, nor elaborated the mapping correlation between electronic structure (low-loss) and chemical fingerprint (high-loss). Thus, DualEELS is vital as it records high- and low-loss spectra simultaneously (Scott et al., 2008). In precise, this study adopted the DualEELS approach via STEM to determine Zircaloy-4 corrosion, apart from probing into the corrosion chemistry via EELS analysis.

2.5.5. Spectrum imaging

Spectrum imaging is a technique that cleats an EELS at each probed point, while the STEM probe moves over the specimen. With this technique, for each point $x.y$ (*Figure 2-15*) of the specimen, also the electron intensity at each electron energy E is recorded, resulting in a 4-dimensional data array. Lately the technique has been also applied to the recording of even more data per specimen pixel, for example x-ray, HAADF, etc. Since the EELS recording required significant time, in order for enough electrons to be collected for the spectrum of each point, there is danger for drift that will image distortion. The drift distortion is corrected essentially by conducting a fast survey of the whole specimen, and then comparing the fast-survey images with the detailed images collected during spectrum imaging. The long collection times of the EELS would also mean big damage to the sample by its continuous bombardment, on the same spot, by the electron beam.

For this reason, a fast beam switch is employed to limit the exposure of the sample to the beam. When using normalised spectra, the intensities of the peaks allow absolute quantification of the atoms present in the sample under study (see below), also known as Dual EEL spectroscopy (Luo, 2016, Wang et al, 2018).

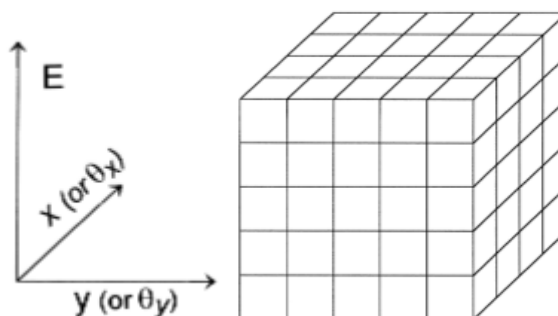


Figure 2-15: Schematic representation of the spectrum imaging technique: Each x-y point on the specimen is associated with a spectrum (points on the E-axis), i.e. each cube contains an electron intensity value at this point in x,y, E (Egerton, 2016)

2.5.6. Common processing techniques

The raw, unprocessed electron energy loss spectrum images collected include noise of various types. The noisy data cannot be used directly for quantification; rather, many processing steps are performed to the dataset, in order to select data and reject the noise. These steps and techniques to perform spectral clean-up are standardised in the EELS community and are readily available in the “Digital Micrograph” (DM) program (The Gatan Microscopy Suite Software and EELS.info websites provide access to the program and a pedagogical overview of the techniques, respectively). Below are listed in detail the stages involved in removing the background noise from Dual EELS datasets (information mainly gathered from DM User’s Guide).

- i. **Correct Zero-Loss Centering:** - When datasets are obtained, the zero loss peak does not occur at zero eV. The spectrum has therefore to be realigned so that this feature is moved to zero. By selecting the ‘Correct Zero-Loss Centering’ menu item with the spectrum-image active, the routine prompts the user to specify the corresponding zero-loss drift map from a list of the open images that are dimensionally compatible.

The selected image should contain the calibrated deviation of the input data's zero-loss peak position (DM User's Guide, 2003). This procedure allows the removal of zero-loss drift that can arise from chromatic effects or microscope high-tension instability.

- ii. **Non-linearization** - In the process of the low-loss and high-loss datasets being recorded, they were not perfectly aligned at the point where they were supposed to meet. There was a clear and visible misalignment between the two which was believed to subsequently affect further steps in the processing methods described in this chapter. Hence, it must be dealt promptly with the as-acquired data. After a thorough analysis, it was found that the mismatch was caused by the energy scale in the spectrometer that was not being linear. Therefore, the energy loss linearity had to be identified and corrected first before any other processing steps could be employed. This process was characterised using a script from B. Schaffer (Gatan) which scans the ZLP across the spectrometer using accurately known voltage shifts on the drift tube.. A second script was used to analyse the results of the non-linearity characterisation and measure the peak position, which varied with spectrometer dispersion linearity. This script was provided by Mr. Robert Webster at the University of Glasgow and is shown in Appendix A with permission from the author. The script was functional by locating the maximum pixel position throughout the full ZLP scan across the spectrometer and gathered all these maxima into a single image. A gaussian is fitted on each peak to avoid the jitter on the ZLP, and this is then used to find the centre. The positions of these maxima are then compared to the ideal reference positions where the ZLP was expected to be, and the deviations were calculated. The script uses the polynomial correction to both energy and intensity per channel and produces a linearised version of the spectrum image.
- iii. **Extract volume:** - After realigning the zero loss peak, a small range of channels at each end of the spectra often contain unreliable data. Moreover, there is loss of detection efficiency at either end of the

spectrum caused by shadowing of the electron beam by the entrance aperture of the EELS spectrometer. Only the central region of the dataset where these effects are not an issue is selected, thus cropping the outer edges which contain alignment artifacts is required. This is done using the Volume - Extract tab in Digital Micrograph.

- iv. **Remove X-rays:-** This function allows the user to remove intense pixels from a data-set that may have been generated by x-ray events. The routine that is built-in in the DM program can check every image plane of the data to detect spikes in energy more than 10 standard deviations above the local median. This higher energy, pixel-size presentation is typical of the interaction of an X-ray with the detector. All anomalous pixels found by this procedure are set to the local median.
- v. **PCA noise reduction:** - Principal Component Analysis (PCA) is a multivariate statistical analysis method that can be performed on a spectrum imaging data file, using a plug-in process in DM, which uses proper weighting based on Poisson statistics. After decomposition of the SI file, each component from the PCA analysis leads to the extraction of a pair of a loading spectrum (spectral feature) and a score image (spatial amplitude) for each point. In this way, a noise-free (or noise-reduced) dataset from the original SI can be reconstructed.
- vi. **Splicing and deconvolving:** - To continue analysing a dataset, the low-loss and high-loss spectra need to be spliced together into a single spectrum image. If the spectrometer bleed-through (as described in Section II) is not removed, issues could arise such as steps in the spliced spectrum image in the region of the splice point. Notably, the low-loss and high-loss data have different acquisition times; which means that the spectra will have different intensities at the splice point, with the high-loss having higher intensity than the low-loss. When splicing, the two are scaled to the same intensity with the difference in intensity being given by the splice ratio. This varies across the dataset, with the splice map showing the splice ratio at each (x, y) pixel in the spectrum image. Ideally, the splice ratio at each point will be similar as the time

ratio, i.e. the difference in intensity between the low-loss and high-loss spectra at the splice point is the same as the difference in acquisition times between the two. However, this is not usually the case, especially in the case that small pixel to pixel variations were expected. The agreement is better after the non-linearity in the dispersion is corrected for, with further improvement when the stray signal from spectrometer bleed-through is removed as well. These corrections have to be applied together with PCA for noise reduction. In order to remove plural scattering, Fourier-logarithmic deconvolution is used. This removes the effect on the shape of the low-loss as a result from changes in the specimen thickness, carbon contamination or composition. It also ensures that the subsequent steps described in this chapter can be performed as it uses the standard spectra that were taken under different experimental conditions, as long as they have also been deconvolved. This step uses Fourier transforms and is based on the assumption that plural scattering will follow Poisson statistics. At all times, I must be cautious to avoid any negative counts in the spectrum as this will lead to artefacts in the deconvolution. These negative counts can often be found before the ZLP after the bleed through signal has been removed; hence, this is another reason to eliminate the signal in that region using volume extraction.

- vii. **Background subtraction:** - Using scripts in DM, background noise can be removed from the low-loss SI.
- viii. **Log-ratio low-loss deconvolution:** - The electrons that are scattered inelastically and end up in the core-loss edges of the EEL spectrum may have been submitted to more than one scattering event inside the sample. To eliminate the outcome of this so-called 'plural scattering', a beneficial technique is to use the low-loss region. In this region, the effects of plural scattering will be utmost visible as a tail of the ZLP to higher energies (higher losses). This region can then be used for the deconvolution of any other energy area around interesting core-loss edges. The Fourier-Log technique is used for this deconvolution (in essence, the Fourier transform of a region around the ZLP and a - similar

in width - section around an interesting peak are Fourier transformed and divided; the result is Fourier transformed back to the energy space). In principle, this way can be used to properly eliminate plural scattering from all energy-loss regions of the spectrum at the same time, (although noise magnification can be difficult in low signal to noise data) (Anderson, 1998).

- ix. **Relative thickness:** - The zero loss peak can provide information about the thickness of the specimen. This is done by comparing the intensity of the zero-loss peak with the intensity of the electron beam without any specimen in the holder. The thickness of the sample, t , relative to the local mean free path for inelastic interactions is related to the ratio of the two intensities, assuming Poisson statistics for the scattering events.
- x. **Signal SI:** - The high loss area is a combination of the combinatorial falling background of all peaks of lower energy, and the discrete, edge peaks coming from specific atoms, which are the most interesting characteristic of the EEL spectrum. By fitting the combinatorial falling background, the “peak-only” spectrum for each scanned point on the specimen can be extracted. This produces the ‘Spectrum Imaging’ (SI) or Dual EELS that is the main focus of the present thesis. The region of the background before the peak (at lower energies) that is to be fitted can be selected manually or automatically. The procedure is complicated by overlapping peaks and by plural scattering.
- xi. **Deconvolve SI:** - The final step in the SI processing is to use the information of the energy resolution and other information from the PCA analysis of the zero-loss peak, in order to deconvolve the SI. The final result is a clean, background-subtracted spectrum of sharp peaks (due to the deconvolution of the energy resolution), with well-calibrated intensities (calibrated for losses due to the sample thickness), for each point on the specimen, as so-called intensity map (I map).

A graphic synopsis of the analysis technique is shown below in *Figure 2-16*. It shows the processing sequence in parallel for both regions of the spectrum, the Zero Loss Peak (low-loss region), and the spectrum of highly-scattered electrons (high-loss region). Some results from the processing of the ZLP are used in the core-loss region, as explained in the steps above. First, the spectra are corrected for any known non-linearity of the instrument with respect to energy or position of the scanning spot (these are measured by operating the instrument loaded with reference materials and grids). The zero of the spectrum is then adjusted, as explained in step i. above, and then the steps, as described above, are then followed for the two regions of the spectrum. The processing can be highly automated, however, in many of the steps there is provision for manual intervention of the operator, to set correct parameters, select regions of interest, perform alternative techniques, etc.

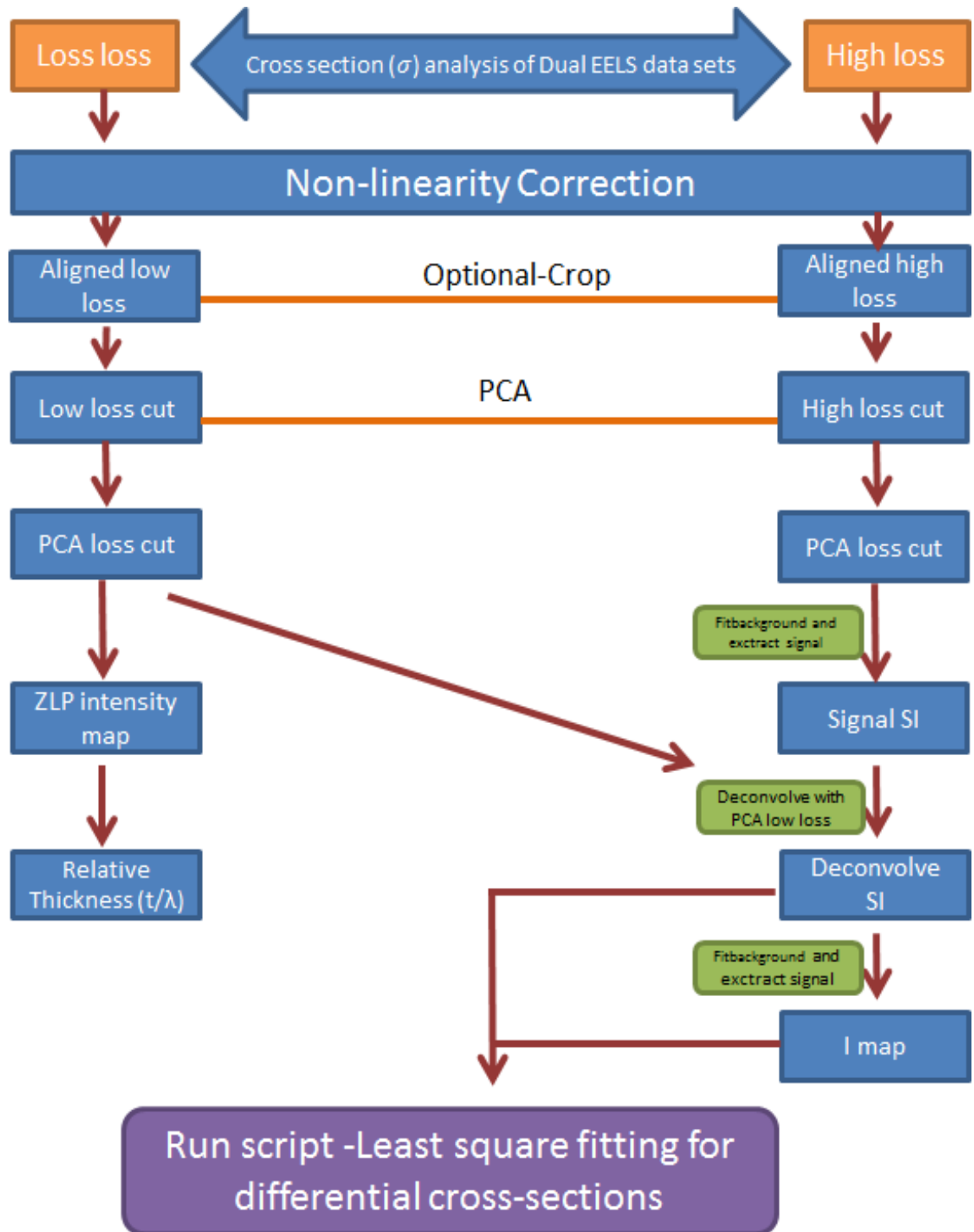


Figure 2-16: Graphic Synopsis of the analysis flow.

2.6. Quantitative Standards-Based Elemental Analysis with EELS

Quantitative microanalysis by EELS depends on measuring the characteristic inner shell line intensities and converting them to elemental concentrations. This is done using the following simple formula:

$$I = I_0 N \sigma \quad (23)$$

where I is the intensity of the edge, I_0 is the un-scattered electron intensity of the zero-loss peak, N is number of atom/m³ and σ is the core edge cross section (probability of interaction) which is called partial cross section and is obtained from differential cross section by choosing a suitable energy range window. The intensity of the edge is measured usually by integrating the background-subtracted, deconvolved peak area over a suitable energy interval. The un-scattered electron intensity is then calculated by doing the same integration to the zero-loss peak, over an appropriate energy window, allowing for non-characteristic background. The core edge cross section is usually available in EELS reference libraries of pure samples, and therefore, the number density of atoms of a particular type in our sample can be calculated from (23) (Rez, 1982). If the background cannot be subtracted effectively, because there is e.g. a local overlap of many edge peaks, it is preferable to fit the experimental spectrum in the core-loss region to sum of background and a reference edge (Ahn & Krivanek, 1983).

There are two complicating factors in this process. The first is that the ionisation edges of atoms that participate in chemical bonds are slightly shifted with respect to those of pure sample (chemical shift). However, inner-shell electrons have energies separated by tens or hundreds of eV, whereas chemical shift energies amount to only a few eV. Hence, identifying ionisation edges in the energy-loss spectrum not only provides a means of quantitative elemental analysis, but also gives information about the structure of the sample, by studying the relative positions of the specific atoms' edge peaks, and their shift from their expected places in the spectrum. Combining the shifts of particular atoms, can in principle reveal the atoms existing in its vicinity, and in this way provide much

more data than the simple stoichiometry, or even the EEL spectrum itself can give (Ahn, 2004, Luo, 2016). The possible change in the cross section can be also calculated, although in principle this uses quite involved mathematical techniques (Foot, 2005).

The second complication arising in the quantification process, comes from the thickness of the sample. Electrons that pass through multiple layers of atoms can be scattered many times before arriving at the spectrometer. This scattering, moreover, does not have to come from the same type of atoms, or even only from atoms (there can be plasmon, phonon, etc. scattering events). In the case of plural, or 'multiple', scattering, the above formula (23) is only approximately correct. To compensate for the extra energy loss in multiple scattering, the integration of the zero-loss peak happens in a larger energy window, which in principle will include other low-loss scattering mechanisms, like plasmons and phonons. Then the integration of the edge peaks is performed over the same energy width (Rez, 1982), presumably including low-energy loss scatterings that happen after the main scattering event that creates the edge peak. Including the whole ZLP area in the deconvolution function of the core-loss peaks is an alternative (conceptually equivalent), more mathematically involved technique (that works better at the higher energy peaks, which are much more isolated) (Luo, 2016).

In case the zero-loss peak is not recorded for every core-loss spectrum in Dual EELS, relative quantification of the atoms present in the analysed sample is still possible. In other words, the ratio of number densities of the two atoms, A, B, is related to the ratio of the intensities of their peaks, multiplied by the respective cross sections:

$$\frac{N_A}{N_B} = \frac{I_A \sigma_B}{I_B \sigma_A} \quad (24)$$

It is desirable to use the same edge type (K-, L-,...), and the same integration width when making the calculation of the intensities of the two atoms to be used for relative quantification.

Cross-sections can be calculated from first principles, using atomic physics models of the participating atoms, in particular calculating the ‘generalised oscillator strength’ of the atomic transitions (Groves, 2005). This is done in practice with numerical integration of the wave functions of the specific shells occupied by the electrons before and after the transition, using approximation techniques like Hartree-Slater wave functions. Alternatively, hydrogen-like approximations are used that can give exact analytic solutions, which only work, however, for K- and L-edges (Foot, 2005).

With Dual EELS, and reference EEL spectra available, multiple linear least square fitting of the reference spectra can be also performed. In this technique, the recorded spectrum for each scanned point is fit using an overall falling background and the reference spectra as components. The fit provides the coefficient of participation of each of the reference spectra in the recorded spectrum, as well as the shape of the overall background. This can be useful as an alternative method of quantification for edge peaks that are too close together to be fit and integrated successfully. Alternatively, it can be used to explore the chemical and structural environment of the atoms of the sample (Leapman & Swyt, 1988). This is standards-based elemental analysis, and details about the analysis procedure are presented in the following sections, before the presentation of the results and the conclusions.

2.7. Multiple Linear Least Squares (MLLS) Fitting

In the process of achieving a spectral signature for each phase of pure region within the dataset, Multiple Linear Least Squares (MLLS) can be utilised by fitting it to a standard spectra. Specifically, the programme creates a model function which consists of a linear combination of the specified spectra and/or models, and then fits that model to the foreground spectrum by adjusting the coefficient of each linear term to minimise the square deviation between the model and the selected spectrum. Consequently, this command is a general (linear) fitting facility that can be employed to the analysis of overlapping edges and superimposed fine structure. This was notably a trial and error technique in which fits had to be iteratively made to sections that were believed to have

contributed to the data set. In the meantime, I constantly analysed the resulting chi-squared map to identify where the fits were not perfect. Once the MLLS fit is complete, the algorithm returns the fit coefficients corresponding to the optimal linear combination of the specified reference spectra to the input data. As a result, this technique allows one to have access to not only how much of each reference is given but also where it comes from. It can be assumed that if MLLS is applied correctly to a spectrum-image dataset, it provides the ability for researchers to map the spatial distributions of the input reference spectra.

2.8. Conclusion

Electron microscopy is a powerful technique for the study of biological, structural, technological and other materials. Electron microscopes' principles of operation are an extension of the conventional optical microscopes, based on the wave nature of electrons. The electron microscopes consist of the electron production system, the lens system and the imaging system. The lenses of the electron microscope are cylindrical electromagnets, creating magnetic fields that act on the electrons and focus or direct them. Electron microscopes also suffer from essentially the same defects and limitations as the optical ones: aberrations, astigmatism, etc. An added bonus of the electron microscopes is the extra information that is produced during the interaction of the imaging electrons with the specimen under study., for example X-rays, Auger (inner shell) electrons, secondary emitted electrons, and elastically and inelastically scattered electrons of the original electron beam of the microscope. The inelastically scattered electrons, in particular present discontinuities in their energy, depending on the kind of atoms they have interacted with, while travelling through the sample.

In this thesis, proposed and already used coating materials for next-generation gravitational wave detectors are analysed using scanning transmission electron microscopes. The main focus of the research is not on the images or diffraction patterns created by the materials under study, but rather the electrons that have inelastically interacted in the sample. These are collected and their energy analysed and recorded (electron energy-loss spectrometry technique) while the electron beam of the STEM is scanned across the samples. The resulting

spectra are analysed quantitatively, and result in a combination of stoichiometric and structure information with unprecedented resolution, for the studied coatings. These results are presented in the following chapters.

3. Quantification of Ta₂O₅-TiO₂ Film Composition

3.1. Research approach

A major part of the coatings-related work within the LIGO-Virgo collaboration has investigated TiO₂-doped Ta₂O₅, for mechanical loss, optical and other properties. Various samples of TiO₂-doped Ta₂O₅ were prepared for this reason, using heat-treatment with temperatures ranging from 200°C to 600°C, and TiO₂ doping levels ranging from 25% to 55%. The coatings studied in this chapter are multi-layer coatings with 30 alternating layers of $\lambda/4$ (at 1.064 μm) thick SiO₂ and Ta₂O₅ doped with TiO₂, and manufactured by LMA [Laboratoire des Matériaux Avancés, LMA, CNRS-IN2P3, France. <http://lma.in2p3.fr>]. These coatings were deposited using ion-beam sputtering and also heat-treated for 24 hours.

Doping high-index Tantalum (Ta₂O₅) with Titania (TiO₂) is already known to reduce mechanical loss and has been implemented as a mirror coating in A-LIGO (Harry et al. 2003, Harry, Armandula, et al. 2006, Flaminio et al. 2010,). Mechanical loss in mirror coatings is the main limiting factor hindering the sensitivity of interferometric gravitational wave detectors. However, mechanical loss can only be understood if we understand the structure, and in order to model the structure correctly, we need to determine the composition accurately and precisely. The main aim of this research is to gain accurate information on the composition of the samples that are being studied in the LIGO-Virgo collaboration. In the work programme of which this thesis forms a small part, detailed studies of film preparation, film, structure, and film properties are performed, and accurate composition information is provided. This enables the determination of potential candidate compositions for use in Advanced LIGO mirror coatings. This work can also guide the development of next-generation coatings.

The second generation of detectors, Advanced LIGO and Advanced VIRGO mirror coating are made by LMA. The mirror coating in Advanced LIGO are using

multi-layer Ta₂O₅ coatings doped with TiO₂. The coating manufacturer LMA first suggested doping Ta₂O₅ with TiO₂ as an alternative coating material to pure Ta₂O₅. TiO₂ is an excellent dopant for Ta₂O₅ because Ti ions are a similar size to Ta ions, because Ti-O and Ta-O bonds are similar in length, and because they both co-ordinate to oxygen in octahedra, suggesting a fair degree of solid solubility between the two oxides. The combination of these factors gave a strong case for studying Ta₂O₅ coatings doped with TiO₂, as these would have a stable amorphous structure and possibly give a high-quality alternative to pure Ta₂O₅ coatings.

In order to better understand the mechanisms behind this improvement, and thereby to further improve coatings, we need to understand the atomic structure of the coatings, specifically TiTa₂O₅ (approaching the composition used in Advanced LIGO). One critical input for atomic structure modelling is the composition of the coating, and this chapter describes the measurement of the composition of Ta-Ti-O amorphous films with unprecedented accuracy and precision using Dual Electron Energy Loss Spectroscopy (DualEELS), and absolute quantification of the resulting spectra. This was made possible due to recent experience in the *Materials and Condensed Matter Physics* group at the University of Glasgow, where standards-based quantification has been very effective for other materials including carbides in steels [Craven 2016, Craven 2018] and Si-Ge quantum wells [Bashir 2018], and so an appropriate set of standards were chosen for this case.

Absolute quantification is the determination of experimental analytical results for each element present within the core loss spectra presented as an absolute equivalent thickness in nanometers, or as an absolute number of atoms along the beam direction. This can only be performed when the EELS partial cross-section is known with high accuracy for each elemental absorption edge used in the analysis, and for all the parameters used in the experiment, and when all data can be normalised to the intensity in the zero-loss peak. Therefore, there are two requirements for this work. Firstly, using DualEELS the zero-loss intensity along with the core loss intensities must be recorded for every pixel. In doing this, the effects of plural scattering can be removed from the data using deconvolution so that the intensity of the edges have a linear dependence on thickness, and this is only made possible by having the low loss and core loss for every pixel from DualEELS (recorded simultaneously). Secondly, the cross sections used in the

evaluation must be accurate. Much of the quantitative EELS work performed prior to the development of DualEELS used calculated cross-sections, either using the hydrogenic or the Hartree-Slater model (Egerton 1980, Leapman et al. 1980, Egerton 2011, Egerton 1993). In most experiments where quantification has been performed, the value of l_0 in equation (23) was not available. Thus N (number of atoms per unit area) for each element was not obtained. However relative quantification (the concentration ratio between N for each element) can be calculated, and hence the percentage of each element present can be calculated. If all the edges involved in the calculation of this ratio come from one group of edges (either K, L, M), the uncertainty in the percentages is much reduced since the value is determined by the ratio of cross-sections, and any systematic errors cancel. This benefit does not apply to the same extent if the ratio of a K and an L line cross-section is involved, although the systematic error is again reduced. Some previous work has attempted to determine absolute cross-sections (F. Hofer, P. Golob 1988, F. Hofer 1987, F. Hofer, G. Kothleitner 1996, Crozier 1990) and demonstrated errors in calculated cross sections of 20% (F. Hofer, P. Golob 1988). This requires both low loss and core loss spectra from the same area to be recorded. In most cases, however, absolute quantification was impractical for more than one or two probe positions, because prior to DualEELS, the EEL spectrometers could only record one energy range, and had insufficient dynamic range to record both the bright zero loss peak and the weak core-loss edges in the same spectrum. Nowadays, excellent relative quantification can be performed using DualEELS, wherein single range core-loss and low-loss spectra are recorded together; this has been demonstrated with standards of well-known composition. For example, Bach et al. (Bach et al. 2018), (Bach et al. 2009) showed that it is possible to separate different Nb-oxides, by using the fine structure and careful, standards-based, quantification. This standards-based quantification was performed using the k -factor method (chapter 35.4 of D. B. Williams and C. B. Carter (Carter 2009)). The k -factor is a sensitivity factor characteristic for any EDX study and standard specimen, which means it is not constant for the same specimen, and later on, Leapman applied it to EELS (Leapman et al. 1980).

$$k_{AB} = \frac{N_A}{N_B} = \frac{I(\beta,\Delta)_A \sigma_B(\beta,\Delta)}{I(\beta,\Delta)_B \sigma_A(\beta,\Delta)} \quad (25)$$

where A , B denote different elements, I is the edge intensity, and σ is ionisation cross-section. The theoretical k -factor calculation is rapid and can be used for all spectral data. It is crucial to study a well-prepared TEM standard specimen of known stoichiometry. However, this method is recommended only when a quick composition answer is enough. When high accuracy is needed, other methods are advised.

While, as described above, it was already possible to determine absolute cross sections, the practical difficulties, also noted above, meant that cross sections were often calculated from experimentally determined ratios with a better known cross section (Manoubi *et al.*, 1990), rather than by direct measurement, i.e. another k -factor method. Neither method is particularly applicable to EELS mapping using spectrum imaging, especially as none of these methods takes any account of thickness variations of edge intensities. The introduction of DualEELS allows the ZLP to be used for normalisation of the signal and makes quantification possible on an absolute scale. Deconvolution also allows for the removal of the effects of plural scattering. Thanks to the single scattering full energy range spectrum, it is possible to obtain experimental differential cross-sections from well-characterised bulk standard material. It is also possible to quantify large datasets collected via spectrum imaging from inhomogeneous samples with few Ångström resolution, which were acquired under similar experimental conditions to the standard data. By using the experimentally determined cross-sections, each element's absolute thickness can be calculated. The choice of edge used for quantification is an important step. In the case of our specimen, the elements that were quantified were Ta and Ti. The standards used in this research and the corresponding edges used are presented in *Table 1* below:

Standard Sample	Edge
TiO ₂	Ti-L ₂₃
SrTiO ₃	
Ta ₂ O ₅ 300° C	Ta-N ₄₅
LiTaO ₃	

Table 1: Standard samples and edges for quantification analyses in TiO₂-Ta₂O₅ thin film coating used in Advanced LIGO mirror coating.

These specific EELS edges were selected because they are close in energy, and therefore quite easy to get in the same collected spectrum. An energy setup of 0 eV for the low-loss and 200 eV for the high-loss portion of the sample are selected, leading to an overlap of low- and high-loss areas at around 100-120eV. The resolution is set at 0.5eV/channel and thus the spectrum is extended up to 1000eV approximately, covering all O-K edges. The collected spectra are then spliced together and deconvolved using the Fourier Log method (R.F Egerton, 2011) in order to get a single scattering distribution suitable for quantification, as done in previous related work (Bobyanko, MacLaren, and Craven 2015, Craven et al. 2018). For the required standard cross section, the best spectra from the standards were chosen to be used for quantification of the studied sample.

3.2. Cross section determination

3.2.1. Titanium cross sections

The standard samples used in this research were TiC, SrTiO₃ (STO) and TiO₂. TiC samples were provided by Sandvik Coromant as bulk materials, with known stoichiometry TiC_{0.98} (Craven et al. 2016). for SrTiO₃ samples, a conventional single crystal substrate was used from a sample prepared in a previous project (I. MacLaren et al. 2015, Choi et al. 2014), and amorphous TiO₂ was constructed by spin coating a Si substrate with Ti alkoxide and annealing it at 300°C to burn out the carbon (performed by Dr Andrew Greer in the School of Engineering). These standards were chosen because their structure and chemistry is well known and therefore their edge cross-section can be converted to absolute cross-section with minimal uncertainty. In general samples with a range of different local environment of the Tia atoms are needed to be examined, in order to compare the measured L₂₃ edges to the coatings under study. At the same time, we need to ensure that the ELNES of the L₂₃ edge fits well with experimental observations.

The images for areas of SrTiO₃ and TiO₂ samples used for cross section measurement, together with a t/λ map for the latter (*Figure 3-1*). Both areas show some reasonable thickness variation, which helps in determining the cross section accurately (Craven 2016).

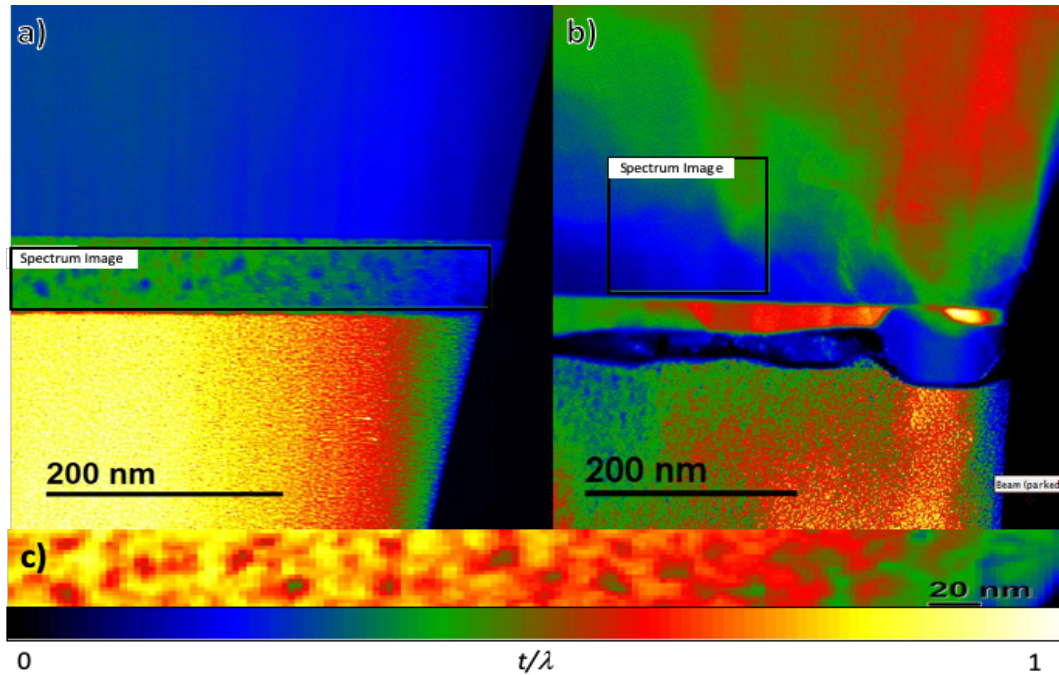


Figure 3-1: The area of the sample used for the cross section measurement: a) survey image for TiO₂; b) survey image for SrTiO₃ c) thickness map of the area scanned in the TiO₂.

The quantification of the chemical composition relies a lot on the function that extrapolates the background shape (R.F. Egerton 2011, Malis, Cheng, and Egerton 1988, Egerton and Malac 2005). Only when this is reasonable under control is the determination of the chemical composition with high accurateness possible, since the shape of the background affects the cross-section. Frequently, the background is fitted in front of the quantified core-loss edge, and extrapolated over the whole range of the energy range used for the integration signal of the chosen edge (Egerton 1996). The fitting of the background in front of the edge is vital because the extrapolation process improves any error in the data (for example underestimations of the cross-sections, or overestimations of the thickness). On a great scale it might be detected in the thick specimen, where multiple scattering is a large portion of the collected signal. The processing procedure permits subtraction of the matrix and surface contributions resulting in signal without multiple scattering and matrix EXELFS, so the background fitting is much improved (Egerton and Cheng 1987). Without these steps, the integration of the signal for quantification is impossible or very difficult and suffers from several errors and overestimations or underestimations of the real signal (*Figure 3-2*).

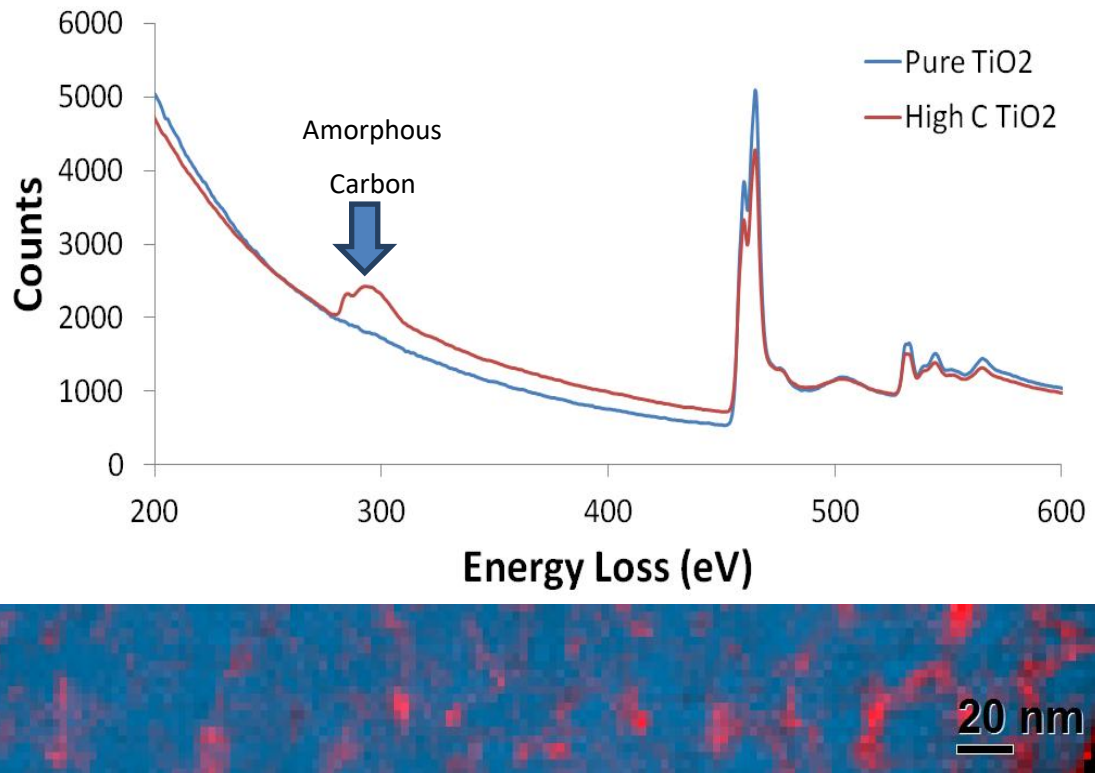


Figure 3-2: Amorphous carbon in the amorphous TiO₂ film, clearly present in some areas in the spectrum, and clearly seen in elemental maps from EELS (60 eV background windows before edge, 50 eV integration window post-edge) with Ti in aqua and C in red.

The amorphous TiO₂ film used in this research showed evidence of traces of carbon, which was easily detected in the spectrum, and can also easily be mapped, as show in *Figure 3-2*, revealing that the carbon has not been completely burned out. TiO₂ in some crystalline form could not be used in calculating cross sections for this research because its ELNES is not comparable to that of amorphous TiO₂ (Bertoni et al. 2006). The Ti in TiO₂ cross section was calculated using the simple ratio technique, based on Equation (23). This was done because the data available came from only six pixels from points with the lowest Carbon concentration in the spectrum image shown, and all had very similar sample thickness values, which meant that the script method [Appendix B : Least squares fitting for differential cross-sections with tags] fails due to the lack of thickness variation.

The cross section for TiO₂ was calculated using a Ti atomic number density of 29.41 atom/nm³ based on the anatase lattice parameters of (Horn et al., 2010).

All TiO₂ polymorphs have similar atom density, but after other structures have been considered such as brookite, anatase and rutile, we assume the sample is anatase based on previous unpublished data that found that anatase is the first form to crystallise from amorphous TiO₂. Based on this structure, the mean free path, λ , was calculated using the corrected lakoubovskii formula (Konstantin lakoubovskii et al. 2008) as 105 nm, while zero loss intensity (ZLP) had a total number of counts of 3.85×10^7 and relative thickness (RT) with mean value of 0.858. An overview plot of three Ti cross sections is shown in *Figure 3-3*.

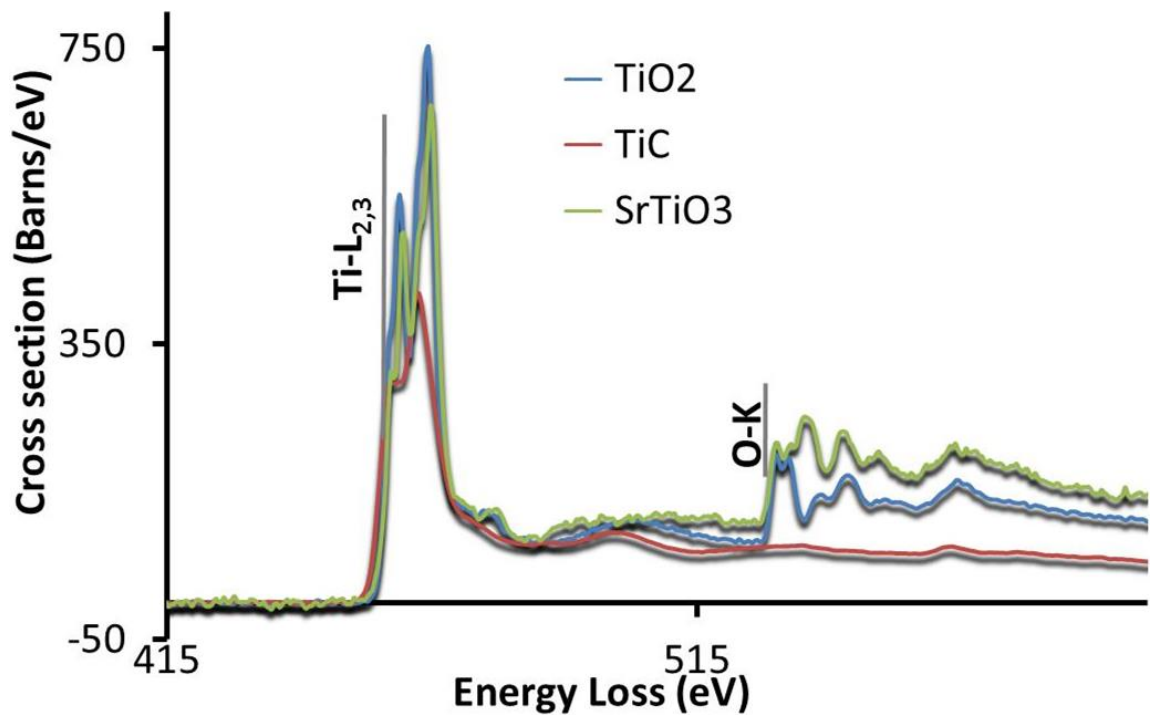


Figure 3-3: Cross section for the Ti-L₂₃ edge in all studied samples.

This plot includes the comparison to Ti cross sections from two other Ti compounds: TiC and SrTiO₃. TiC_{0.98} is a background-subtracted version of the cross section published by (Craven et al. 2018b). SrTiO₃ was calculated using the script method from a spectrum image of 2000 pixels. It covers a thickness range of 30-100 nm, and uses the area indicated in Figure 3.1. A Ti atomic number density of 16.79 atom/nm³ was used based on a standard simple perovskite cell and the parameters determined by (Abramov et al. 1995). Based on this structure, the mean free path, λ , was calculated using the corrected lakoubovskii formula (Konstantin lakoubovskii et al. 2008) as 98 nm.

All cross sections have strong white lines close to the edge, as would be expected for Ti-L₂₃, but their exact position, height and detailed shape varies markedly. The negative numbers are artefacts of the background subtraction and doesn't affect the data analysis of the result. The structures after the white lines also show subtle differences. The sample with the most O, SrTiO₃, has the strongest O-K edge. The TiO₂ has a less pronounced O-K edge with a totally different shape. The TiC has no oxygen, just a weak bump at about 560 eV where the Ti L₁ edge should appear. The similarity in overall magnitude between the TiO₂ and the SrTiO₃ immediately after the edge gives confidence that the calculation of this edge cross section is correct, even when it came from so few pixels.

More detail of the structure of the L₂₃ edge is shown in *Figure 3-4*, which shows these three cross sections compared to a scaled cross section from a sample of nominally 25% Ti in Ta₂O₅. Common to all the spectra is the spin-orbit splitting into 2p_{3/2} (L₃) and 2p_{1/2} (L₂) levels, with a separation of about 5.4 eV (Okada et al. 2004). The degree of crystallinity is reflected by the further splitting of the L₂ and L₃ peaks into two peaks each due to the crystal-field interaction. Octahedral coordination of titanium atoms with oxygen splits the Ti 3d states into the *t*_{2g} (3d_π) and *e*_g (3d_σ) symmetries (Okada et al. 2004). SrTiO₃ showed a very clear splitting of the L₃ peak and slight splitting of the L₂, suggesting strong octahedral coordination, and is fully consistent with the perovskite crystal structure. This effect is much weaker in the amorphous TiO₂, whereas the L₂ and L₃ splitting is well known to be very strong in crystalline TiO₂ e.g. (Bertoni et al. 2006). In contrast to this, the splitting is almost absent in TiC where the peaks are rather broader and less well defined. In the amorphous 25% Ti in Ta₂O₅ sample, the L₂₃ peak is clear, and similar to that in the amorphous TiO₂ but without any splitting in either white line. From the figure, TiC presents also slightly lower onset energy; this is probably due to more electron transfer to O in the oxide samples than to C in the carbide.

While the other well-known structures like SrTiO₃ and TiC produce good quality cross sections, the ELNES does not match what is seen in our (Ta,Ti)O_x films, and the best match is seen for the amorphous TiO₂ standard. However, even though this standard came from a fairly small area of sample with low residual

carbon, we can have confidence in the absolute value of the cross section, as the level after the ELNES around 500-520 eV is very similar to those from better known Ti-containing structures.

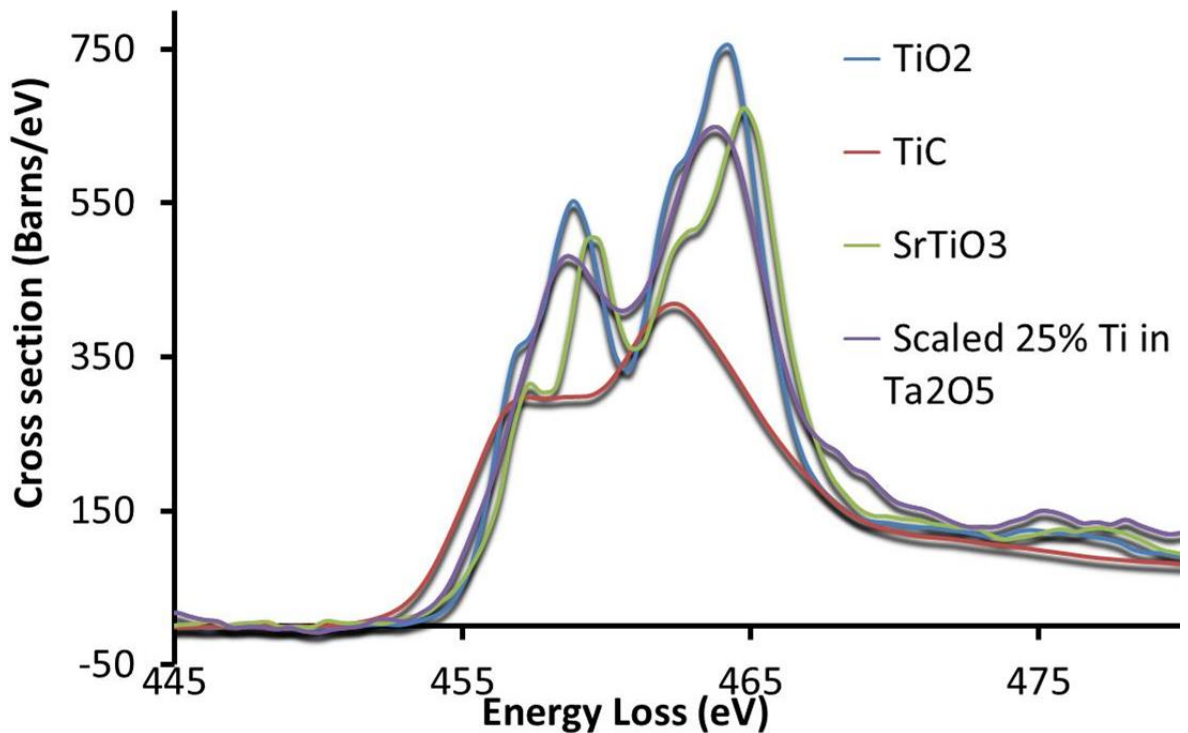


Figure 3-4: ELNES region of the Ti-L_{2,3} cross sections for different compounds containing Ti, and their comparison to a scaled cross section for one of the TiO₂-Ta₂O₅ glasses.

The edge that we interested in is the Ti-L_{2,3} edge at 456eV. The integration window must be quite narrow to avoid alterations by the O-K edge at 530eV and by the Ti-L₁ edge which is at 564eV. So, the fitting window for signal integration is selected to be quite narrow (20 eV width), while the background window is taken to be 35eV wide. In *Table 2*, the three presented specimens are automatically processed until the moment of choosing the integrated window for cross-section extraction.

To ensure consistency while processing the cross-section, the background window, signal window and integrated window for signal and background is kept the same for all three specimens; then plural scattering within the specimen is removed from the datasets using a Fourier Log deconvolution method.

Element-Edge	Element	Background Onset (eV)	Background window (eV)	Signal window Onset (eV)	Signal window (eV)	Cross section (Barns)
Ti-L ₂₃	TiO ₂	415.32	35	450.8	20	7692
	SrTiO ₃	415.25	35	450.8	20	4367
	TiC	415.03	35	450.5	20	4326

Table 2: Background integration windows used for TiO₂, SrTiO₃ and TiC analyses.

It would be possible to use a standard for quantification either by stripping the background off the spectrum with a suitable background fit, or by using the standard spectrum with the background on. This latter approach was found to be better in recent work (Craven 2018). The comparison of the two is shown in *Figure 3-5*.

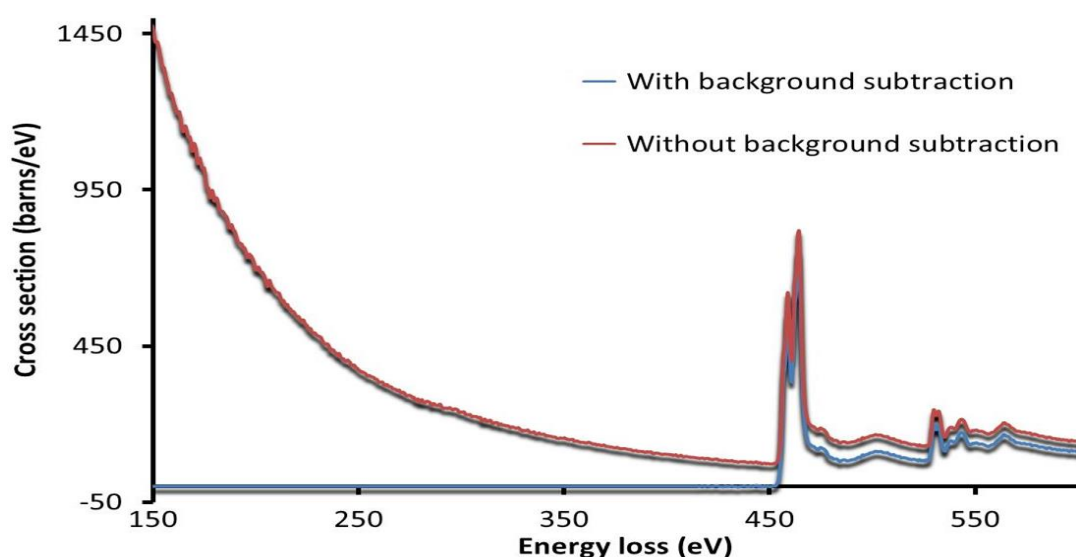


Figure 3-5: EELS spectra of cross section with background subtracted and without background-subtracted of Ti-L_{2,3} and O-K.

3.2.2. Tantalum cross sections

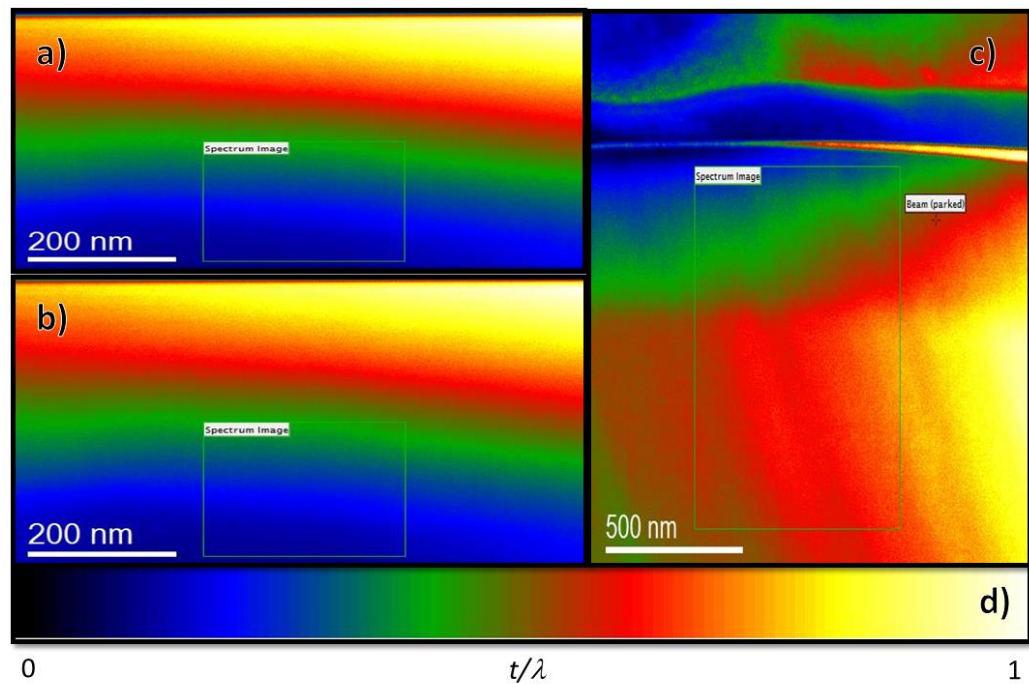


Figure 3-6: The area of the sample used for the cross section measurement: a) survey image for 003 Ta₂O₅ 300 °C; b) Survey image for 004 Ta₂O₅ 300 °C c) Survey image for LiTaO₃. d) Relative thickness colour scale

In order to provide a standard for Ta, we need a well-known stoichiometric structure, but well-characterised samples of suitable compounds are scarcer for Ta than for Ti. The standard samples used in this research were amorphous Ta₂O₅ (a-Ta₂O₅) heat-processed at 300 °C and LiTaO₃ (LTO). The amorphous Ion Beam Sputtered IBS tantalum coatings were manufactured by the Commonwealth Scientific and Industrial Research Organisation (CSIRO, Materials Science and Engineering Division, West Lindfield, NSW, Australia). The coatings were deposited onto fused silica substrates were subject to post-deposition annealing at 300 °C for 24 h in air, and have been studied previously in the LIGO project (Bassiri et al. 2015). Specimens were prepared for the scanning electron diffraction studies using a standard cross section method of gluing two sections of film face to face, encapsulation in a brass tube with epoxy resin, slicing, polishing and dimpling. The samples were then thinned to electron transparency using a Gatan Precision Ion Polishing System (PIPS) (Gatan Inc., Pleasanton, CA, (USA), which used Ar⁺ ion irradiation at a relatively low energy, 4 kV beam, and a final 0.5 kV polishing stage, to avoid any changes to the sample material structure (See more details in

section 2.4.1.1). For LiTaO₃, a commercially produced single crystal (001) substrate was used (manufacturer unknown) and prepared using a FIB lift-out method (Figure 3.6).

The cross section for Ta₂O₅ was calculated using a Ta atomic number density of 21.1 atom/nm³ based on a calculation from the bulk density of 7.75 g cm⁻³, as determined by X-ray reflectivity measurements. This is a little lower than most crystalline forms of Ta₂O₅ as is for example well reviewed by (Bassiri et al. 2015) with a range of densities mostly in the range 22.26 gcm⁻³ (Liu et al. 2007) and 23.11 gcm⁻³(Larson, Cromer, and Roof 2002) (except for some high pressure forms). Based on the structure type of Nb₂O₅(HP) (Varambhia et al. 2018) structure, the mean free path, λ , was calculated using the corrected lakoubovskii formula (Konstantin lakoubovskii et al. 2008) as 89 nm.

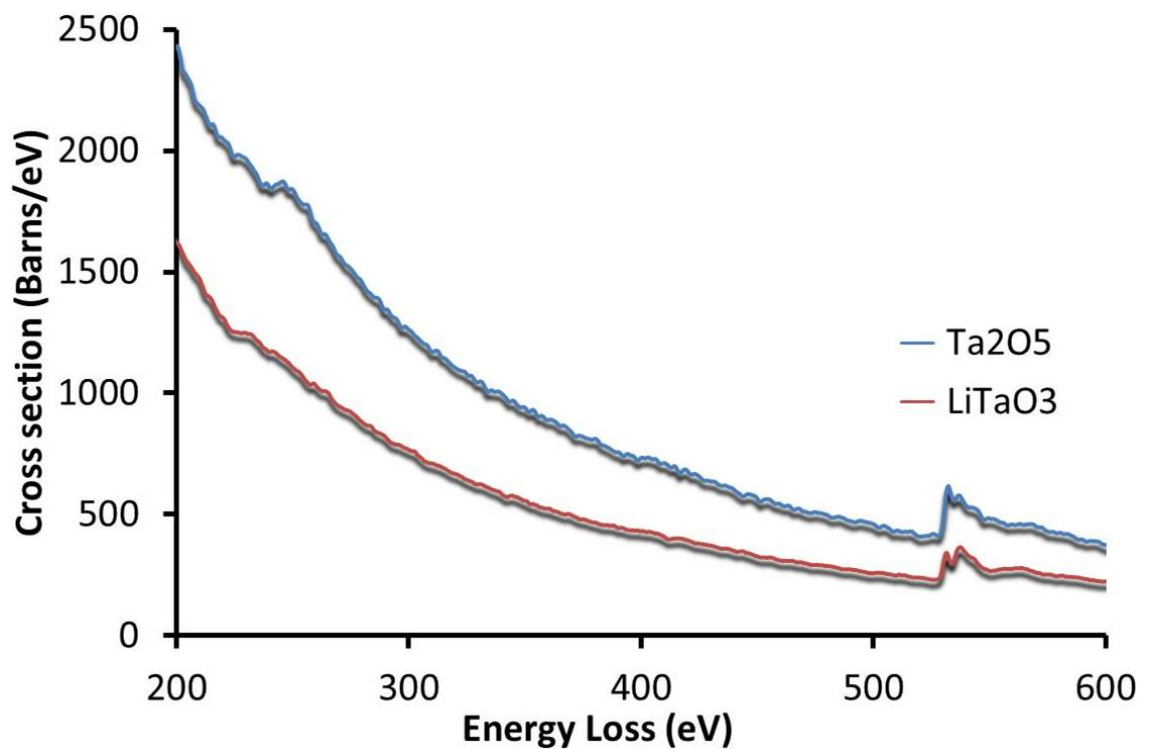


Figure 3-7: Cross section from Ta₂O₅ 300°C and LiTaO₃ without background subtract

The cross section for LiTaO₃ was calculated using a Ta atomic number density of 18.92 atom/nm³ determined from the structural refinement of (Abrahams, Hamilton, and Sequeira 1967). Based on this structure, the mean free path, λ , was calculated using the corrected lakoubovskii formula (Konstantin lakoubovskii et al. 2008) as 90 nm. Cross sections from two datasets are taken

from the Ta₂O₅ film and compared to one from LiTaO₃ in Figure 3.7. The spectrum showed consistency in both data by showing a similar Ta-N₄₅ edge at ~ 229 eV and also at O-K edge at ~ 532eV.

Figure 3-8 shows a background-subtracted cross section of both standards used in this calculation. The fitting window for background extrapolation for Ta-N₄₅ starts at 175.75eV with a width of 35eV. With the background removed, the Ta-N₄₅ edge can be more clearly seen. For Ta₂O₅ a much noisier spectrum is recorded compared to LiTaO₃, and noise amplification in cross section determination is sometimes a problem, especially where signal to background ratio is low (Ian MacLaren et al. 2018). A particular issue is that the background subtraction leaves the tendency well after the edge a little ambiguous, although the near-edge shape looked a little different between Ta₂O₅ and LiTaO₃.

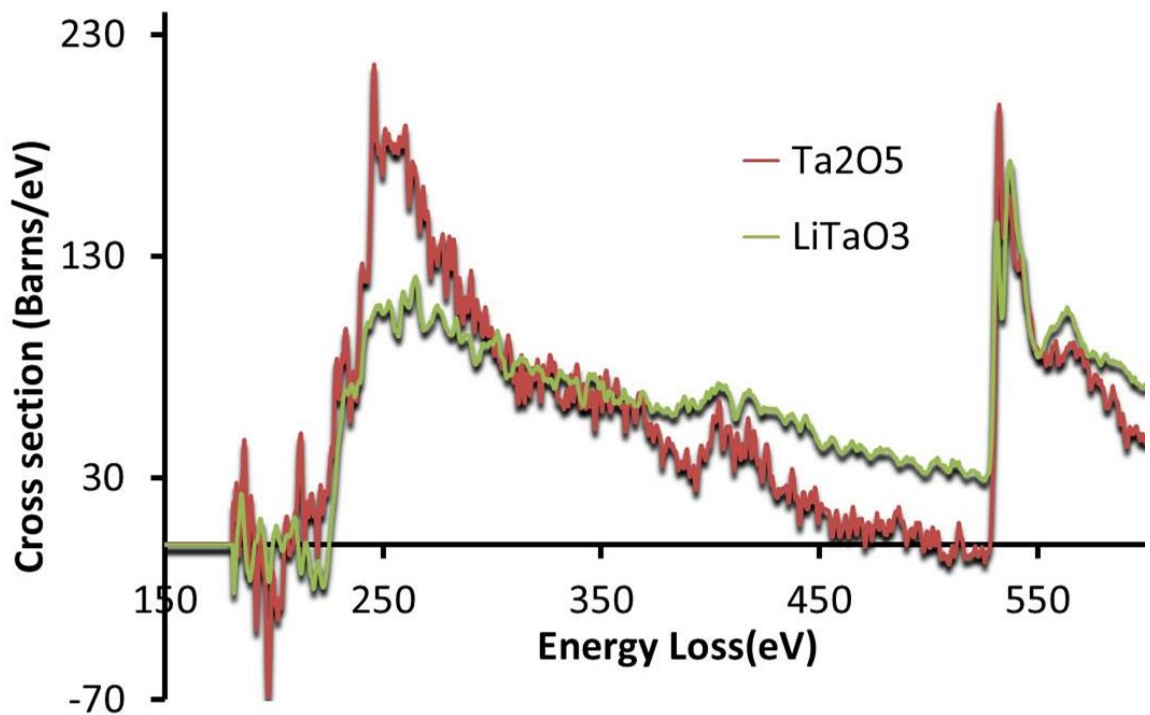


Figure 3-8: Background-subtracted cross sections of Ta-N_{4,5} (and O-K) of Ta₂O₅ 300 °C and LiTaO₃.

Figure 3-9 shows the comparison between background-subtracted deconvolved spectra for Ta₂O₅ and LiTaO₃. The background subtraction was altered until the range around 400eV-500eV followed the same trend. They were manually normalised to have the same integral in this range. This technique, matching of the area after the edge, was chosen because the long term trend after the edge

(ELNES) should be the same no matter what the immediate chemical environment of the atom is; several hundred eV above an edge an atom's chemical environment has a negligible effect, all unoccupied energy states above the Fermi level will be the same, and the cross section values tend to the isolated atom cross section. This effect has previously been noted for transition metal carbides with Hartree-Slater calculations of the cross section (which assume isolated atoms) (Craven et al. 2016). It is now clear that the chemical differences between LiTaO₃ and Ta₂O₅ produce a big difference in ELNES for the first 50 eV above the edge onset, which would seriously affect the quantification by both not fitting the shape well, and underestimating the true cross section (resulting in an overestimate of Ta content).

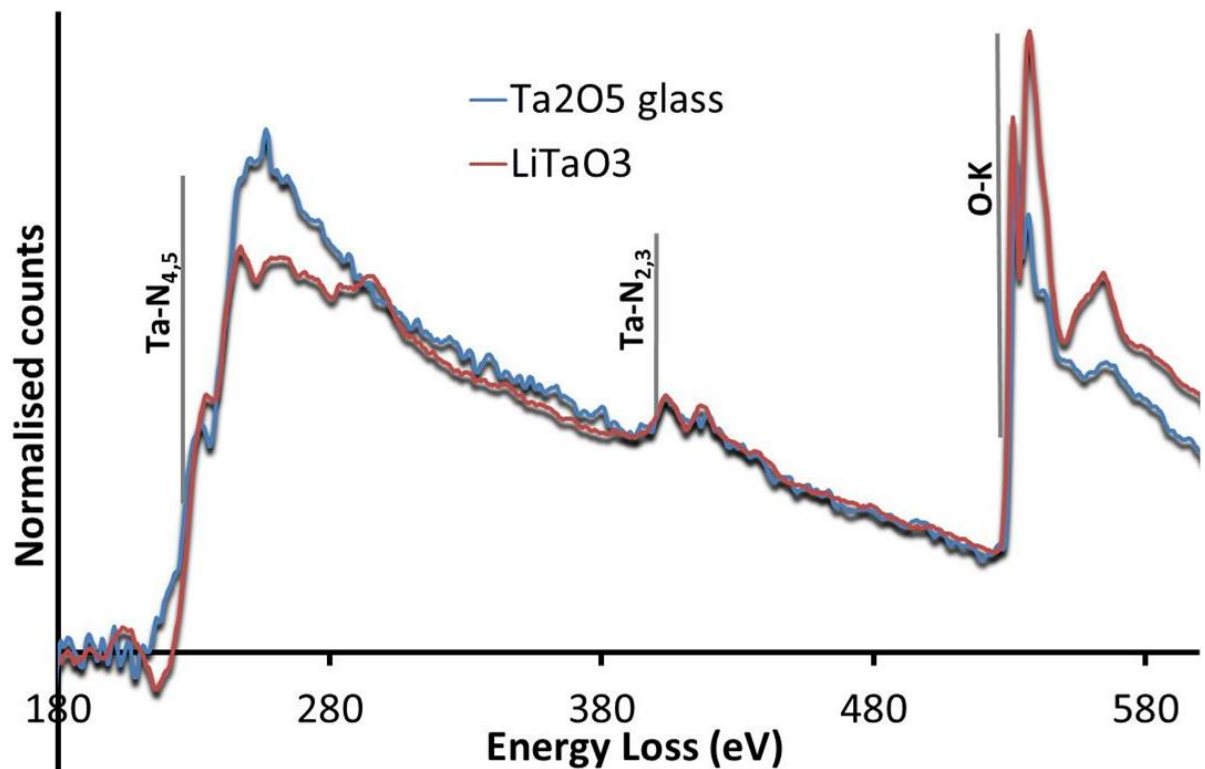


Figure 3-9: Background-subtracted normalised deconvolved spectra for two different oxide compounds containing Ta: LiTaO₃ and Ta₂O₅

3.2.3. Chosen standards

Overall, these results indicate that the amorphous TiO₂ and amorphous Ta₂O₅ (heat treated at 300 °C) produce good quality cross sections in the area of interest. Figure 3-10 shows the cross section for these two standards on the same

plot including the backgrounds. Previous work showed that fitting spectrum images using standards with non-removed backgrounds worked better (Craven et al. 2018), and it is expected that subtracting the backgrounds prior to fitting would increase uncertainties. Earlier work (Bobyanko, MacLaren, and Craven 2015), (Craven et al. 2016) shows that the background from the matrix has significant deviations from a simple power law shape. These deviations arise from extended energy loss fine structure (EXELFS) from lower-lying edges. Thus, subtracting backgrounds from the data and the standards data before attempting quantification is a potential source of significant error.

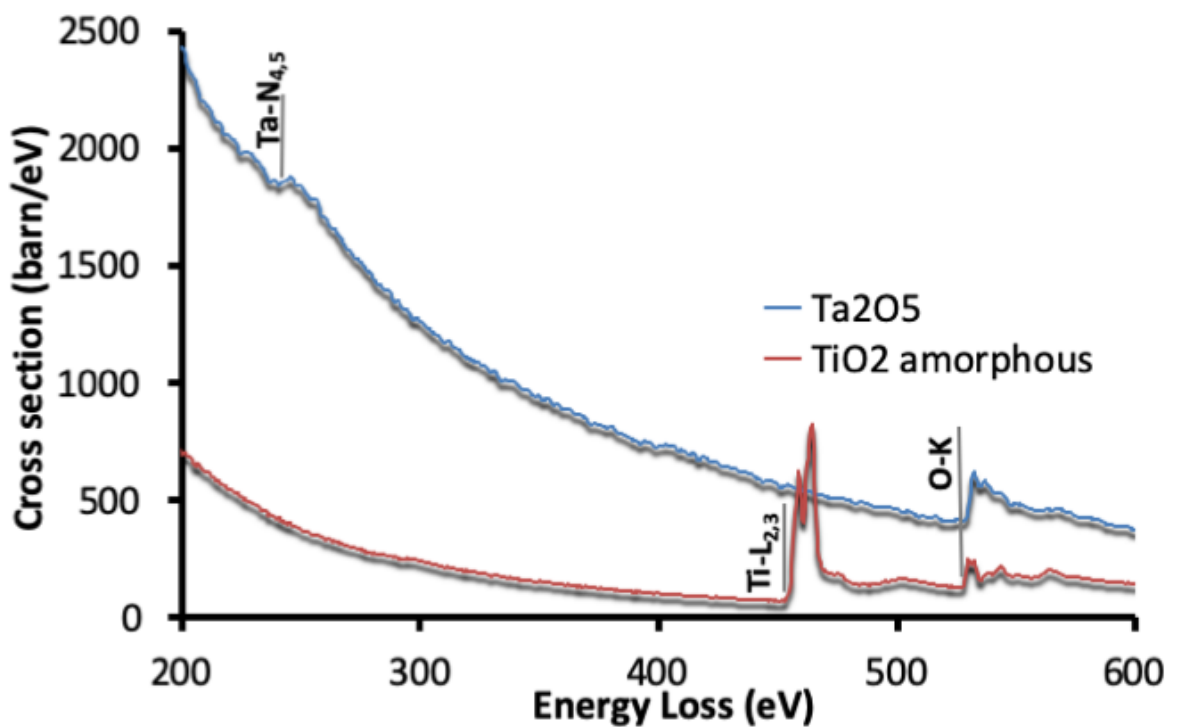


Figure 3-10: Cross section for two standards on the same plot including the backgrounds.

3.3. Ta₂O₅-TiO₂ elemental analysis with experimental cross sections

To quantify the composition of an amorphous Ta₂O₅-TiO₂ film, a spectrum image containing several hundred pixels is recorded from a suitably thin region of the sample, and this is processed as described previously in section 2.5.6 (Craven et al. 2018). First, the data is processed to obtain a deconvolved spectrum image

of the standard. Then an MLLS fit is done directly on the deconvolved image of the real sample. MLLS fitting is a fingerprinting method which requires a pre-existing set of standard spectra for the elements or phases present in the sample. It then creates a model where the original spectrum image is treated as a linear combination of the standard spectra. The model is then fitted to the original spectrum image by adjusting the coefficients of the linear terms to minimise the squared deviation between model and original. The MLLS fit was performed over the energy range 200-500eV in this case to cover the Ta-N_{4,5} and Ti-L_{2,3} edges.. In principle, just two standards should be needed, one is the standard for Ta₂O₅ and second is that for TiO₂, as shown in Figure 3.11. The result is two maps of the fit coefficients for the sum. These are simple to convert to elemental ratios, according to the following scheme:

$$\text{Scaled spectrum of Ta} = A \times \sigma_{Ta} \quad (26)$$

and

$$\text{Scaled spectrum of Ti} = B \times \sigma_{Ti} \quad (27)$$

The final scaled spectrum, which should be similar to the MLLS fit, is therefore:

$$Ta + Ti \text{ scaled} = A\sigma_{Ta} + B\sigma_{Ti} \quad (28)$$

In this work, samples of of 4 Ta₂O₅-TiO₂ films were quantified: CSIRO 25 Ti 200°C, CSIRO 25 Ti 600°C, CSIRO 25 400°C and CSIRO 55 Ti 600°C for 24 hours.

In summary, the components used in MLLS fit are;

- a) Standard cross section reference spectrum - in this research two standards were used;
 - i) Ta₂O₅ 300°C for Ta-N₄₅ edge
 - ii) Amorphous TiO₂ for Ti-L₂₃ edge
- b) Deconvolved spectrum image of real sample

It is possible to add more components to the fit, as some additional shape added in the MLLS fit could further decrease the residual. However, for this research, only two edges are mainly interesting. After the MLLS fit is performed,

in addition to the maps for the fitting coefficients of each of the standard spectra used in the fit, spectrum images for the fit and the fit residuals are also produced, as well as a chi-squared map (which shows areas of poor fit). The residuals spectrum image can help in revealing the causes of fitting errors. In the following section, this approach is used to perform quantitative chemical mapping of the 4 representative samples of different coating percentage and annealing temperature.

3.3.1. MLLS fitting Ta₂O₅-TiO₂

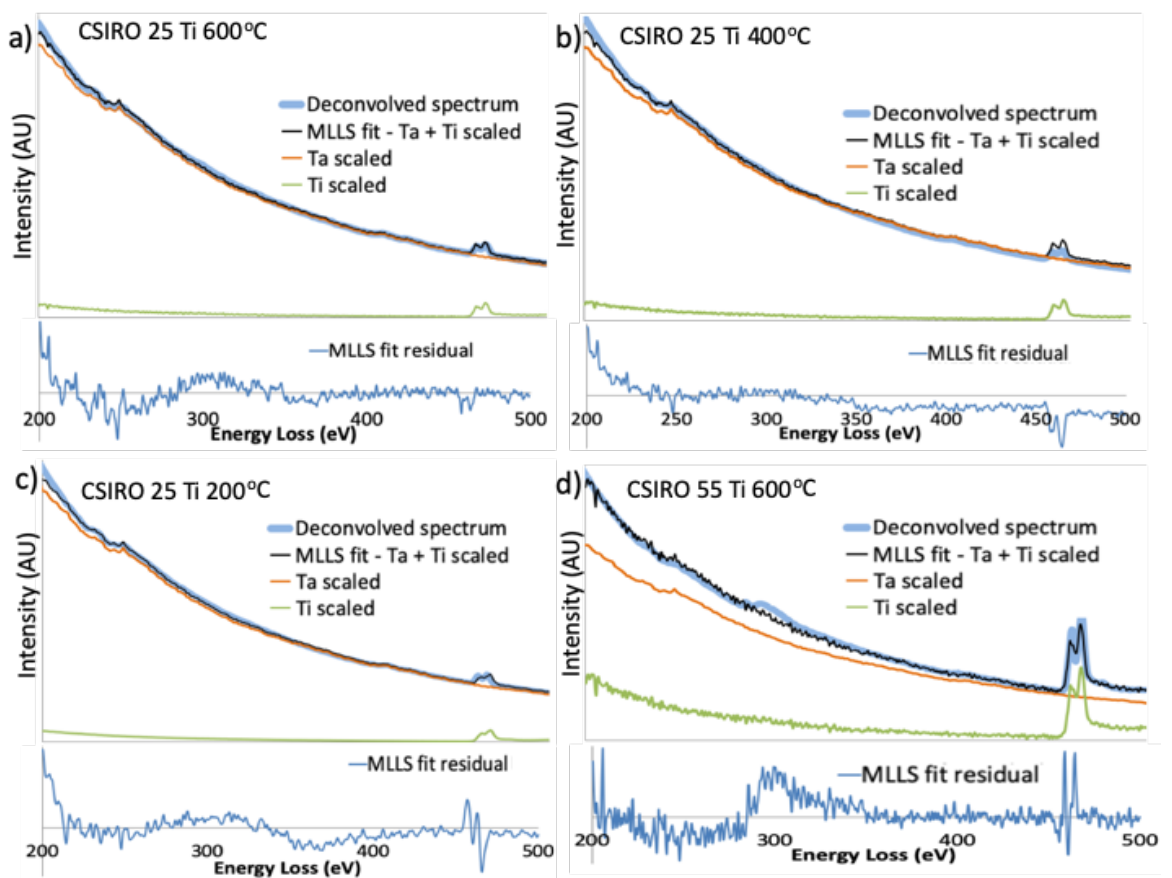


Figure 3-11: MLLS fit on CSIRO samples a) CSIRO 25 Ti 600°C, b) CSIRO 25 Ti 400°C, c) CSIRO 25 Ti 200°C and d) CSIRO 55 Ti 600°C

Figure 3-11 shows the spectra of MLLS fits using all pixels in each spectrum image, quantified for four different samples. Each spectrum image had hundreds of pixels (from 696-1920, depending on the dataset). It can be clearly be seen that all MLLS fit for all samples fit very well with the deconvolved spectra. The Ta-N_{4,5} edge at 229eV and Ti-L_{2,3} edge at 456-462eV match with all samples. In

Figure 3.11(c) the peak of Ta-N_{4,5} and the spectrum wiggles consistently fit the deconvolved spectra, but at Ti-L_{2,3} edge, the MLLS fit can be seen have a shift of about 0.5eV; this could be caused by the energy alignment, and could possibly have been overcome by adjusting the energy alignment. In Figure 3.11(b) similar trends can be observed, however the Ti-L_{2,3} edge of the MLLS fit has higher intensity than the deconvolved spectrum, suggesting a significant overfitting. For Figure 3.11(a) the trends for MLLS fit and deconvolved fit match almost seamlessly to each other. MLLS fit in Figure 3.11(d) shows significant noise in the spectra, but still follows the overall trend, and the important edges, Ti-L_{2,3} and Ta-N_{4,5} can be distinguished. In this case, in the deconvolved spectra a carbon edge at 284eV can be seen suggesting some surface contamination with carbon. Additionally, all plots show a rising curve in the left edge of the residuals, suggesting a slight misfitting of the background. In order to improve the background fits on these spectra, it may be helpful to add an extra background shape into the fit, as was done in previous work (Craven et al. 2018). Additionally, in Figure 3.11(b) the overfitting of the Ti-L_{2,3} edge is a problem, possibly caused by trying to fit the background shape in addition to the TiO₂ spectrum. Thus, an additional background shape was calculated to add to the fit using a power law fit from 200-450 eV on the TiO₂ cross section. The new inputs for the MLLS fit now are as follows:

- i. The deconvolved spectrum image of real sample
- ii. The Ta₂O₅ cross section for Ta-N_{4,5}
- iii. The TiO₂ cross section for Ti-L_{2,3}
- iv. The background shape calculated from the TiO₂ cross section

As shown in *Figure 3.12*, the new MLLS fit shows more accurate result after addition of an extra background into the fit. The accuracy is increased by comparing the residuals or standard deviation for both; comparing figures 3.11 and 3.12 the residual is clearly improving significantly. The intensity of Ti components also appear smaller after the extra background is fitted, which is due to the extra background calculated from TiO₂ cross section. From the above spectra, the composition of Ti can be observed by looking at the intensity of the spectra: from figure 3.12(a), (b) and (c) which supposedly contain 25% of Ti

coating, the intensity of Ti edge is really small compare to figure 3.12(d) of 55% Ti coating. The percentage of Tantalum and Titanium in real sample is calculated from these spectra, and shown in Table 3 below;

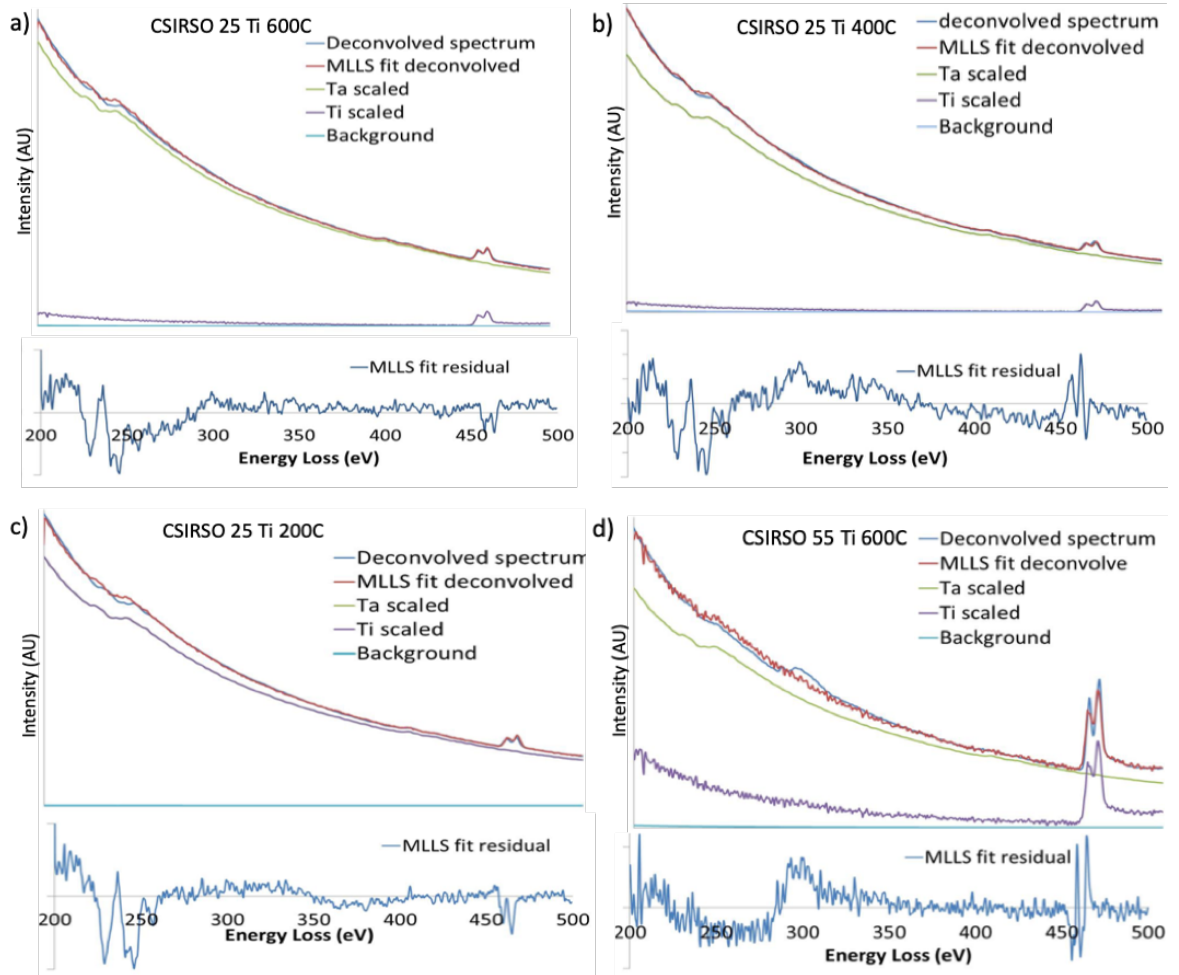


Figure 3-12: MLLS fit on CSIRO samples with extra background on MLLS fit a) CSIRO 25 Ti 600 °C, b) CSIRO 25 Ti 400 °C, c) CSIRO 25 Ti 200 °C and d) CSIRO 55 Ti 600 °C

Figure 3-13 shows the compositional maps of relative concentration of Tantalum and Titanium from each of the spectrum images for each of the four samples, using the same colour scales in each case. All elemental maps for the 25Ti samples are very similar in shade, corresponding to a Ti concentration well below 25%, although the variability in the 400 °C is slightly larger. This is believed to be due to a larger noise level in this dataset, due to the choice of less optimal acquisition conditions. The Ta and Ti concentrations in the 55Ti-600 °C sample are radically different to these and clearly close to the intended stoichiometry, but are notably uneven in some parts of the sample.

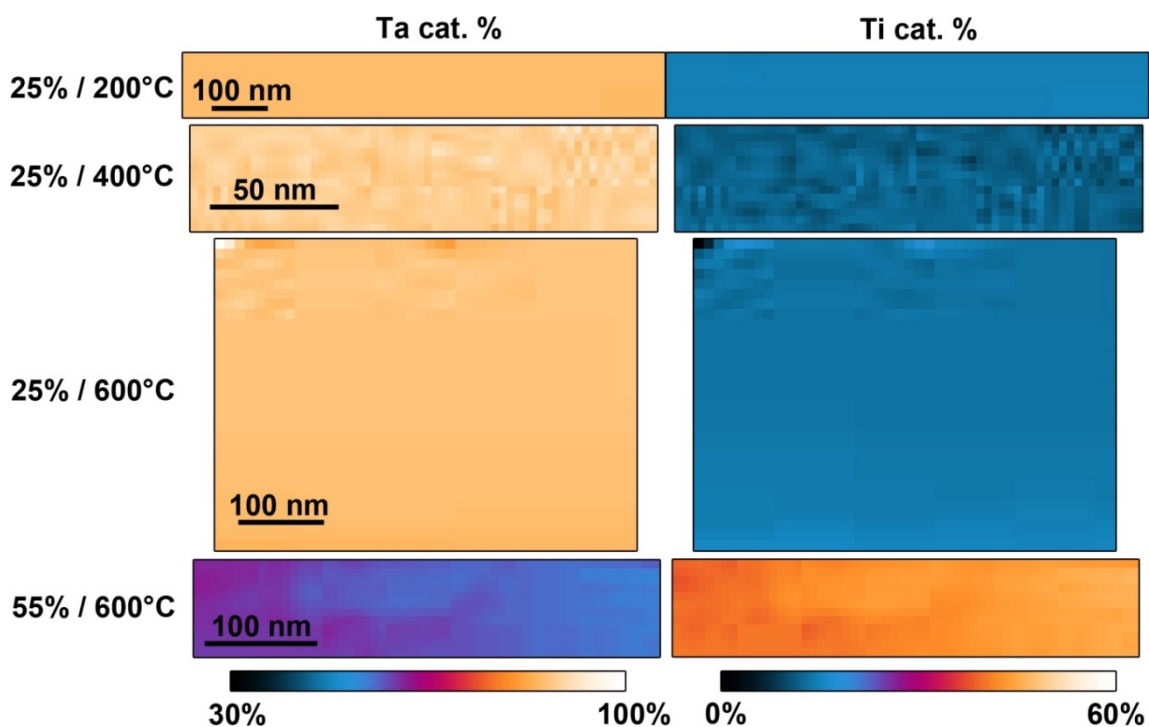


Figure 3-13: EELS mapping of Ti and Ta cation percentage for CSIRO samples with 25% and 55% coating of Ti heat treated at different temperature.

Table 3 shows the average cross-section based quantification in each sample. There are some differences between the different 25Ti samples, in all cases larger than the random error, as can clearly be seen in the histograms of Figure 3-14.

Sample	Ta cat %	Ti cat %
25 Ti 200 °C	88.8 ± 0.1	11.2 ± 0.1
25 Ti 400 °C	91.5 ± 1.2	8.5 ± 1.2
25 Ti 600 °C	89.6 ± 0.5	10.4 ± 0.5
55 Ti 600 °C	56.1 ± 2.3	43.9 ± 2.3

Table 3: Chemical compositions of the four samples in atomic percent as determined by EELS quantification using the MLLS fitting

It is unclear if this is genuine variations from one sample to another (as they are different pieces coated in the same way and therefore nominally of the same composition, not different pieces of the same sample). But, they are clearly a long way from 25% Ti. These samples were previously quantified from EELS data,

using a simpler procedure of background subtraction, integration, and quantification with a standards-based integrated cross section (i.e. a scalar number, not fitting with a differential cross section). In that work, DualEELS was used, and deconvolution was performed. The result using this simpler, more traditional quantification procedure was published as part of Bassiri et al. (2016), and a result of 14 ± 3 cat. % Ti was found. Both the absolute percentage, and the error are different. The absolute value may differ due to difficulties with background subtraction and that the absolute number depends critically on the choice of background window, a problem not found with the MLLS fitting method when backgrounds are included. Clearly, however, these latest measurements confirm the earlier conclusion that the nominally 25% Ti samples was seriously deficient in Ti.

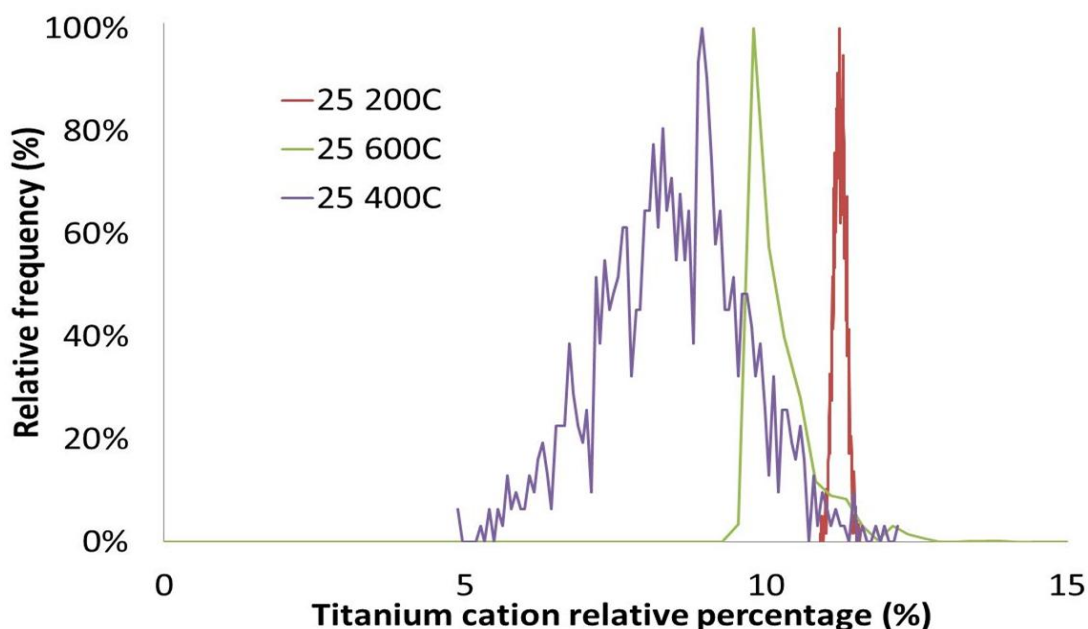


Figure 3-14: Titanium cation relative percentage

Comparing further back in time to the first paper to use EELS for Ti cat. % determination in Ta₂O₅-TiO₂ (Harry, 2007), the samples were different, so the absolute numbers are not comparable. But, again, this work used background subtraction and integration of edge intensity, this time prior to DualEELS and quantification (so the results could be affected by thickness changes in the samples). The errors are several percent in all cases, just as in Bassiri et al. (2016). The random error in these two studies is probably higher because background fitting in the presence of noise also causes amplification of noise in

the integrated background-subtracted intensity. It is therefore, clear that the MLLS procedure gives a significant advantage over traditional background subtraction and integration procedures, even with a standards-based cross section for Ta (where no calculated cross section is available).

For the sample of 55% Ti 600 °C, the result of the quantification is 43.9 ± 2.3 cation % Titanium, apparently more real variation from area to area, not just single pixel noise. This result shows better error than early work in 2006 (Harry et al. 2006) and 2016 (Bassiri et al. 2016), which is at that time, the quantification is very difficult due to Ta edge being so weak at higher Ti content. Initial results on this sample in 2016 give 52 ± 10 Ti cat. %, so absolute number also changed a lot once the whole spectrum fitting works properly, rather than just background fitting small windows on a wiggly background. Ti content is again lower than planned (supposed to be 55%). But not as big a percentage difference as in the nominal 25%. No direct comparison on this figures from any alternative method, but recent work has included Rutherford Backscattering Spectrometry for composition measurement (Vajente et al. 2018), and would be good to cross-check the same sample by both techniques in future.

3.4. Conclusion

The analysis steps to extract the element information from the data, whether it is their atomic number density, relative thickness, λ , or accurate chemical composition must be determined with care by analysing and comparing structure from similar material. From this information, the cross section is calculated, and the best standard to be used in the MLLS fit of DualEELS for quantification is determined. After the standards to be used are determined, the composition of Ta₂O₅-TiO₂ amorphous films similar to those used in A-LIGO is measured with high accuracy, using standards-based quantitative EELS. The results show significant variation of the composition over the surface of the films, as well as significant deviation from the nominal value of Ti doping, depending on the thermal history (annealing temperature and duration) for each sample.

4. Quantifying Ta₂O₅-ZrO₂ Film Compositions

4.1. General concept

The original interferometric gravitational wave detectors had used multilayer mirror coatings consisting of ion beam-sputtered amorphous silica (SiO₂) and tantalum pentoxide (Ta₂O₅), which were demonstrated to achieve close to 1 ppm level of total optical losses (absorption plus scatter) (Martin 2018). A standard HR mirror coating design was used, in which materials with high and low refractive indices were deposited in alternative layers, each having an optical thickness of $\lambda/4$ to which λ is the wavelength of the laser used in the detector. As reviewed in Chapter 3, a reduction in the mechanical loss of these coatings was later achieved through the incorporation of titania within the tantalum layers and this was used in the coatings for the Advanced LIGO detectors used in the first ever detections of gravitational waves (Abbott and et al. 2016), as this was found to give the lowest mechanical loss (Harry et al. 2007)

Substitute high-index materials to Ta₂O₅ have been considered and the range of candidate materials can be extended if other wavelengths were found suited for the laser in future gravitational wave detectors. Currently, detectors operate at a laser wavelength of 1064 nm, which typically limits the candidate high-index materials to oxide materials, such as Ta₂O₅ and its derivatives, Nb₂O₅, ZrO₂, TiO₂ (Flaminio et al. 2010). To date, Zr or Ti oxides are difficult to prevent from crystallising and have other problems, including high stress. Doping tantalum with TiO₂ had been the main focus leading up to Advanced LIGO, and had shown the most promise (Prasai et al., 2019). But it was theorised that doping tantalum with ZrO₂ would result in lower losses (Tewg, Kuo, and Lu 2004) and by doping with ZrO₂ it was hoped to increase the crystallisation temperature of tantalum. Atomic modelling work carried out by Konstantin Borisenko in Oxford (unpublished work) suggested that zirconia doping could have a similar effect on the flexibility of the structure as Ti doping does.

A ZrO₂:Ta₂O₅ thin film prepared by MLD Technologies (<https://mldtech.com/>) was prepared and some initial characterisation on structural changes with annealing have been performed by (Prasai et al., 2019). In order to better understand the mechanisms behind this improvement, and thereby to further improve coatings, we need to understand the atomic structure of the coatings. One critical input for any such atomic structure modelling has to be the composition of the coating, and this research describes the measurement of the composition of Zr-Ta coatings with unprecedented reliability using Electron Energy Loss Spectroscopy (EELS).

For Zr-Ta-O, the spectra are modelled as a sum of Ta₂O₅ and ZrO₂ spectra. The appropriate energy range edges are given Table 4, so the energy loss range needs to extend to above 2300 eV, and with plenty of background before 1735 (Ta-M_{4,5}). Unlike for Ta-Ti-O, where relatively low losses below 600 eV suffice, this requires higher loss EELS data and obtaining high quality at higher energy losses is not quite so simple. As Craven and Buggy (Craven 1981) demonstrated, it is possible to analyse and optimise the behaviour of the post-specimen lens system in a microscope to assist better transfer higher energy-loss electrons into an EELS spectrometer. Recent work by some of the present authors (Craven et al. 2017) has developed a method for producing significantly improved performance in transferring higher loss electrons into the spectrometer on the microscope used in this work, spreading the useful range for quantitative EELS output to at least 5 keV. This was done by changing the optical path of the electrons through the post-specimen lenses to reduce chromatic effects on ray slope and final crossover position before entering the spectrometer. One feature of this was that performance was optimized for an energy loss of 1.5 keV (not 0 keV, as for a standard imaging camera length); thus extending the range of almost constant information transfer within the spectrometer acceptance aperture to 3 keV, at the cost of a little radial distortion at higher angles (which does not affect the spectroscopy). The most important result of this for Electron energy-loss spectroscopy (EELS) is that the backgrounds behave better using the optimised setup.

There is previous published zirconium L-edge data (Annand, Maclaren, and Gass 2015) and (MacLaren et al., 2018) and (MacLaren, Cummings et al. 2019),

including examining the effect of oxidation on these edges. There is less data for Ta, but a high loss spectrum for Ta oxide is included in the EELS Atlas (Ahn and Krivanek, 1983), and the edge energies are well known.

The standards for ZrTaO, we use are pure amorphous Ta₂O₅ heat treated at 300° C, as also used in Chapter 3, and monoclinic ZrO₂ (more details below), and the edge details are presented in *Table 4*.

Standard Sample	Edge	Edge Energy (eV)	Background Onset (eV)	Background window (eV)	Edge Onset (eV)
Ta ₂ O ₅	Ta-M _{4,5}	1735-1793	1621	100	1723
ZrO ₂	Zr-L _{2,3}	2222-2307	1571	150	2210

Table 4: Background extrapolation windows and edge energies for the standards used in the analysis of the ZrO₂-Ta₂O₅ thin film

There are several reasons why the standard EELS quantification approach fails on this sample. The main reason is the background subtraction in front of Zr-L_{2,3} fails due to the Ta-M_{2,3} edge at 2194-2469 eV which is right before Zr-L_{2,3} edge. Furthermore, the cross section for the Ta-M_{4,5} edge calculated by the Hartree-Slater method is probably incorrect, there are at least two studies showing that the M cross section is overestimated near the edge by the Hartree-Slater calculation (Auerhammer, Rez, and Hofer 1989; Egerton 1993). Additionally, according to (Craven et al. 2016), Hartree-Slater cross sections can be very inaccurate for at least 100eV after the edge due to ELNES effects. So, the best alternative is to fit against known standards.

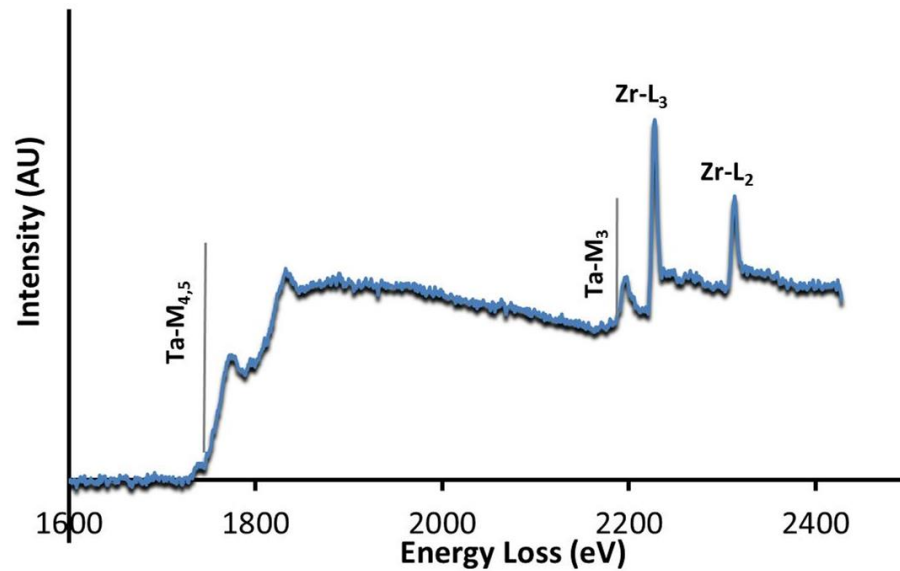


Figure 4-1: An EELS spectrum of Zr-Ta-O the real sample after deconvolution that will be fitted using the MLLS method to find the accurate composition.

Figure 4-1 above shows a spectrum of the film to be quantified, the edges for Ta-M_{4,5}, Ta-M_{2,3} and Zr-L_{2,3} are clearly seen. To quantify the composition of an amorphous ZrO₂-Ta₂O₅ film, there are few steps that need to be taken in order to get accurate result to run a fit at this energy. First is produce a single scattered deconvolved spectra so that the edge shapes do not change with thickness, the only way to do this at high losses is with Fourier-ratio deconvolution (Egerton, 2011). This requires fitting and subtracting a background to the spectrum before the edge of interest and then deconvolving with the low loss spectrum. The two standards have to be treated in the same way, and the background fit must start at the same point for both so the whole spectrum of the film of interest can be treated as a sum of the two cross sections for the standards. Once we have the background-subtracted and deconvolved spectrum image and two background-subtracted and deconvolved standard cross sections, then the MLLS fit can be performed. The fit coefficients can be converted to elemental percentages as performed previously in chapter 3.

$$\text{Scaled spectrum of Ta} = A \times \sigma_{Ta} \quad (29)$$

and

$$\text{Scaled spectrum of Zr} = B \times \sigma_{Zr} \quad (30)$$

The final scaled spectrum, which should be similar to the MLLS fit, is therefore:

$$Ta + Zr \text{ scaled} = A\sigma_{Ta} + B\sigma_{Zr} \quad (31)$$

4.2. Cross section determination

4.2.1. Tantalum

The standard used for Ta is the Ta₂O₅ film annealed 300°C, as used in Chapter 3. *Figure 4-2* shows the area of the sample used for the cross-section measurement.

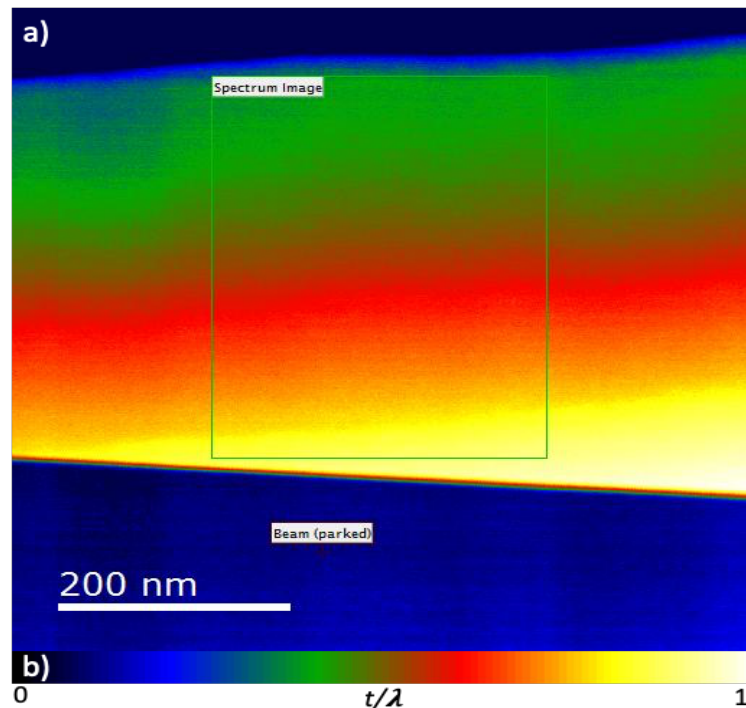


Figure 4-2: a) The area of the Ta₂O₅ 300°C sample used for the cross-section measurement; b) Relative thickness colour scale

The cross section for Ta₂O₅ was calculated using a Ta atomic number density of 21.1 atom/nm³ and the mean free path, λ , of 89 nm, as in Chapter 3. Using the script “Least squares fitting for differential cross-sections Fourier ratio” [Appendix C], the cross section can be obtained. This script is only for use with a background-subtracted Fourier-Ratio-deconvolved high loss SI.

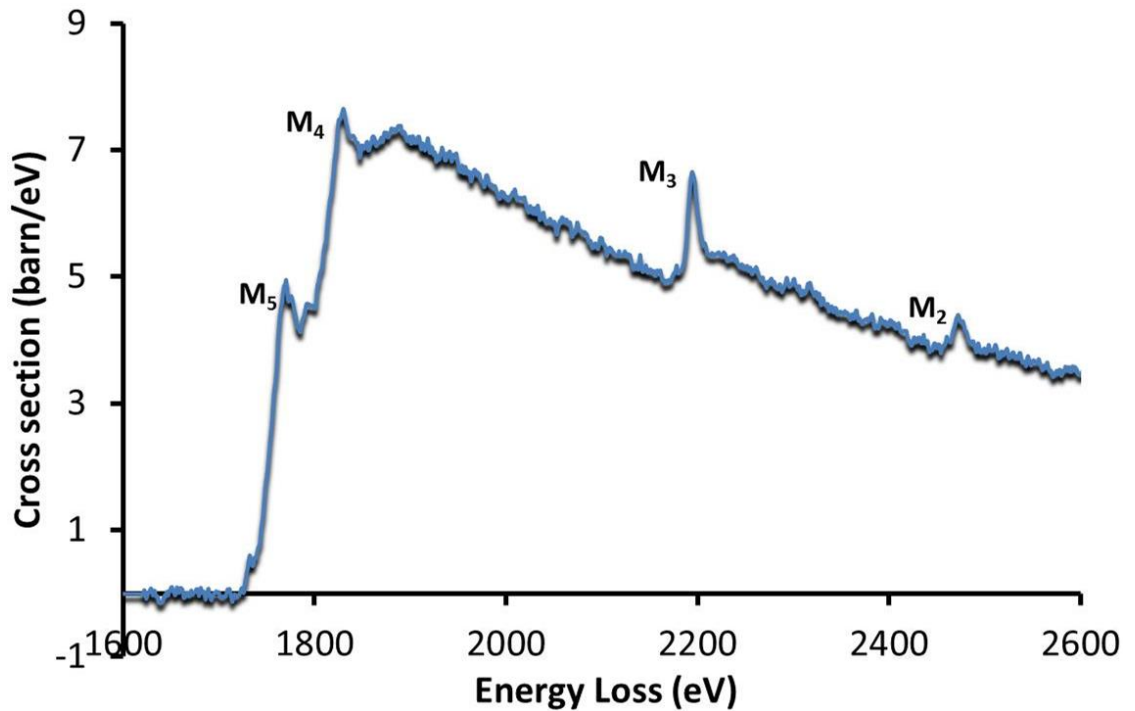


Figure 4-3: EELS differential cross section for the Ta M-edges from a Ta₂O₅ glass, calculated after background subtraction from a 100eV window before the Ta-M_{4,5} edges and Fourier ratio deconvolution with the low loss.

From the script, the cross section in *Figure 4-3* is calculated. The broad but strong peak of the major Ta-M_{4,5} edges dominates the plot. The Ta-M₃ and M₂ edges show sharp white lines, as would be expected for an early transition element because of the large density of vacant 5d states.

4.2.2. Zirconium

The standard used in this research is ZrO₂, grown as an oxide scale on Zircaloy-4, as provided by Dr Kirsty Annand (Annand et al., 2015) (Annand 2018). *Figure 4-4* shows the area of the sample used for the cross-section measurement.

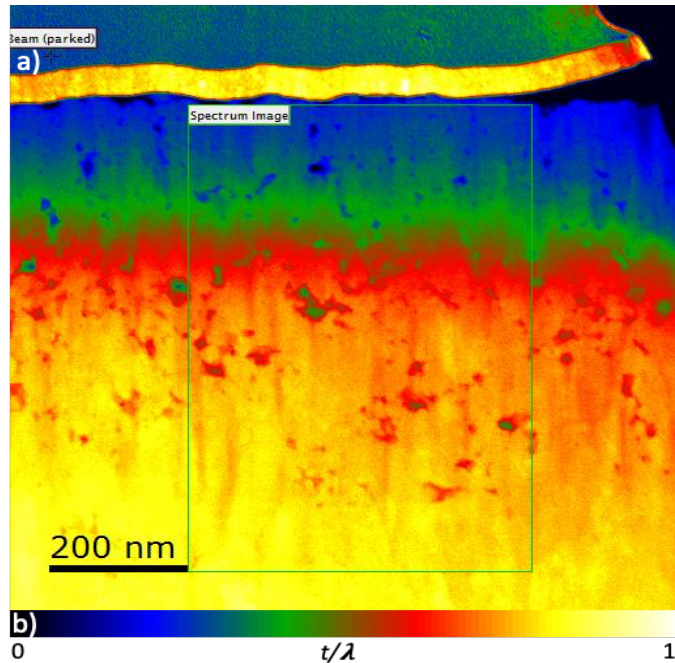


Figure 4-4: a) The area of the ZrO₂ sample used for the cross-section measurement; b) Relative thickness colour scale

The cross section for ZrO₂ was calculated using a Ta atomic number density of 28.48 atom/nm³ based on the monoclinic baddeleyite structure as refined by (Smith and Newkirk 2002). Based on this structure, the mean free path, λ , was calculated using the 80% corrected Iakoubovskii formula (Iakoubovskii et al. 2008, Ian MacLaren et al. 2018) as 95 nm. As for the Ta₂O₅, the area chosen having a significant thickness variation allowed the cross section to be calculated using the “Least squares fitting for differential cross-sections Fourier ratio” script [Appendix C].

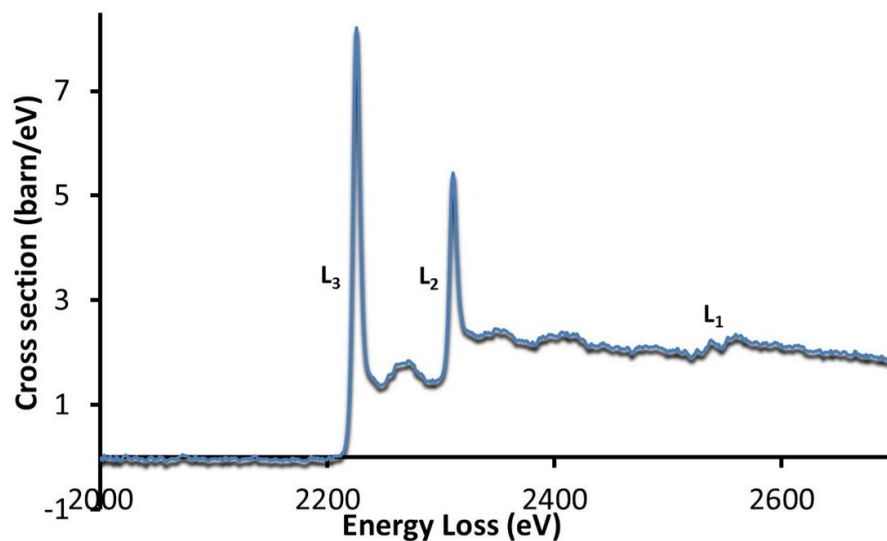


Figure 4-5: Differential cross section for the ZrO₂ L-edges.

The differential cross section for ZrO₂ is shown in *Figure 4-5*. The sharp white lines at the L₃ and L₂ edges are clearly observed, as expected. A weak L₁ peak also can be observed (MacLaren et al. 2018). The exceptional quality of the optical setup for EELS can be seen by the fact that, although the background fitting window ran from 1571-1721 eV, the background subtracted cross section is basically zero with almost no under- or over-subtraction right up until the Zr-L₃ edge at just about 2200 eV. Consequently, this cross-section should be very suitable for quantification of Ta-Zr-O together with the Ta₂O₅-derived M-cross section above.

4.3. Towards elemental analysis with cross section

MLLS fitting over the energy range 1724-2600 eV was then used to quantify the elemental composition of the ZrO₂-Ta₂O₅ thin film. *Figure 4-6* shows spectra for this fit for the whole 1363 pixels in the spectrum image. It is very clear that the fit matches exceptionally well to the deconvolved spectrum throughout, and the residuals are tiny. Unlike in the lower loss case in Chapter 3, no adjustment of background shape was needed. This shows that choosing the right standards is critical in order to get the best result in MLLS fit. There are miniscule differences in the M₅ and M₄ intensity for between the deconvolved spectrum and the MLLS fit. The Zr L₃ and L₂ white lines in the MLLS fit are also slightly sharper compared to the deconvolved spectrum. It is well-known that white line intensity is related to the oxidation (MacLaren et al. 2018; MacLaren et al 2019) and this would not have fitted for any other Zr oxide or compound, especially of a lower oxidation state.

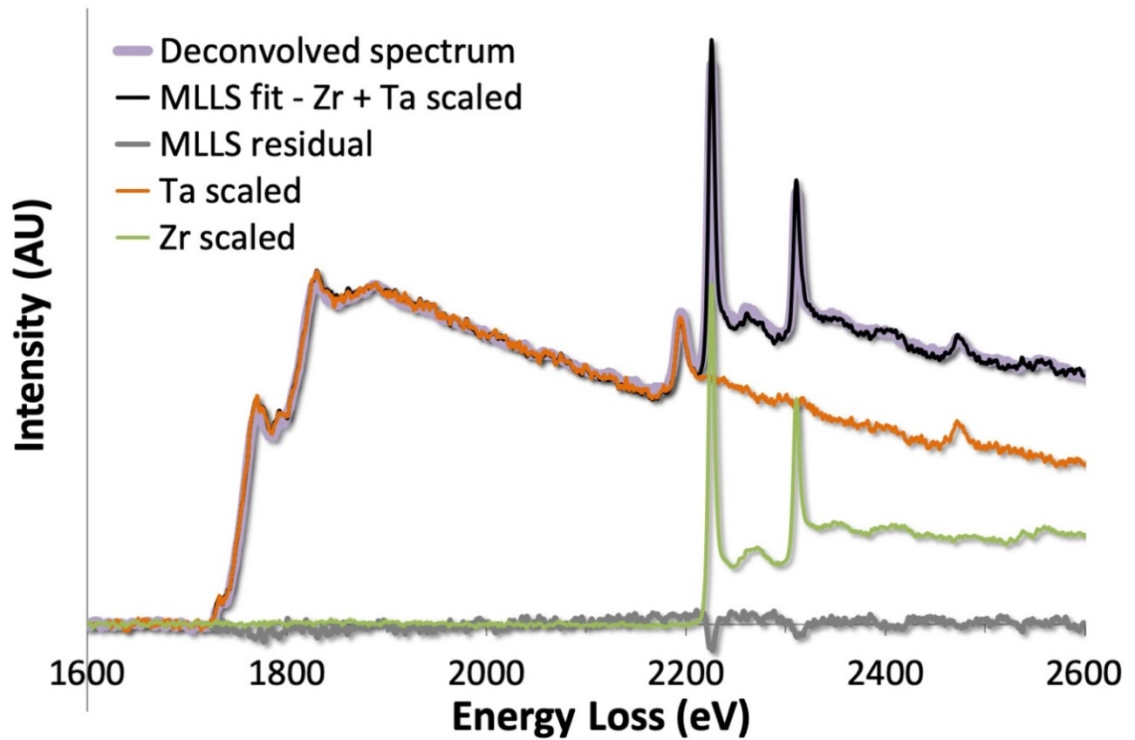


Figure 4-6: MLLS fit to the ZrO₂-Ta₂O₅ LIGO sample

Figure 4-7 shows the elemental map of the Zr and Ta elements, and there is a very nice uniformity of the colour, which indicates that there is very little noise or random uncertainty in the results. There is a possible slight composition gradient from top to bottom indicating that Ta is richer at the top and poorer at the bottom.

From these maps, the composition of each element can be calculated and the result shows that the Zr composition is 47.3 % and Ta composition is 52.7% with standard deviation of 0.6% for both. The distribution of quantification results is also shown in the histograms on Figure 4-7. This film was also quantified independently by (Prasai et al., 2019) using Rutherford Backscattering Spectrometry (RBS), the result they obtain is 48 ± 1 %. This is within 1% of the present result, and within the error bars.

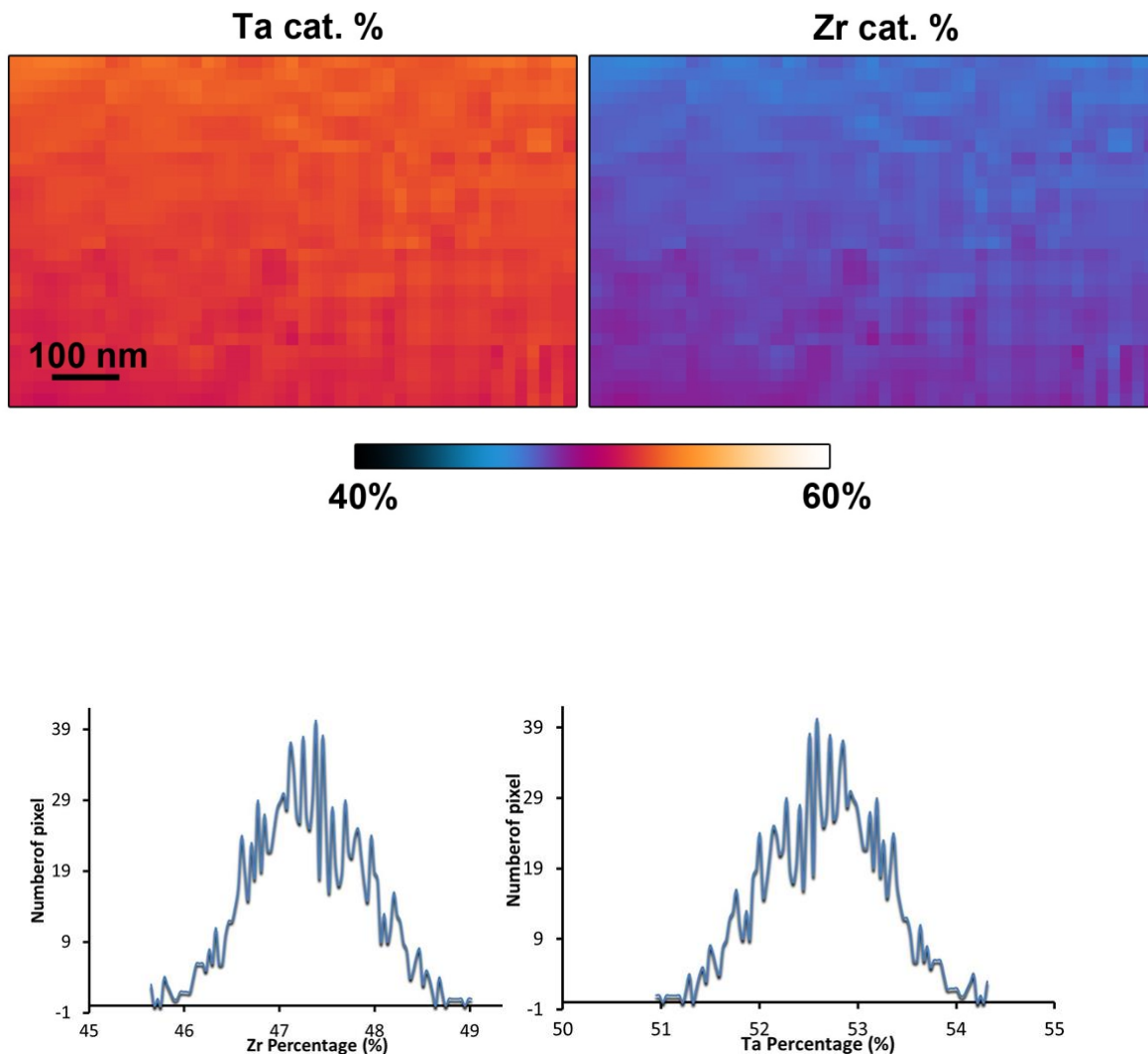


Figure 4-7: EELS mapping of Zr and Ta cation percentage taken at 47×26 pixel size and the histogram graph Ta and Zr and histogram graph for the Ta and Zr percentage.

Nominally the Zr percentage was originally claimed by the coating suppliers to be 34.5%. The agreed Zr coating percentage of 47-48% Zr totally contradicts this, but it is by now completely normal that target compositions of coatings can be missed by 50% or more [REFS Harry 2007, Bassiri 2016]. This makes the performance of such analytical work a completely essential part of the feedback loop in developing suitable coatings of well understood structure and chemistry leading to well controlled properties. Additionally, having a correct chemical composition is an essential part of the atomistic modelling [Bassiri 2013, Bassiri 2016, Prasai 2018].

Of course, the possibility of systematic errors always needs to be considered. In this case, the main concern would be the errors in thickness in the standards. Currently, this is determined from a simple parameterisation (Iakoubovskii et al. 2008) corrected by a phenomenological factor of 0.8 [Craven 2016, MacLaren 2019]. But, this correction was only based on one needle specimen of TiC_{0.98}. Other recent work found slightly different variations from the Iakoubovskii calculations (Varambhia et al. 2018) using a needle method. So, ideally, it would be best to make further needle samples of different materials to test this parameterisation properly over a wider range of samples of different densities and atomic numbers.

4.4. Conclusion

Tantala mixed with zirconia in a glass has been quantified using high loss EELS, using fitting to experimentally derived standards of Ta₂O₅ and ZrO₂. It has been shown that with this higher energy loss, it turns out to be a little easier to perform good quality fitting, since the background subtraction becomes more straightforward and more accurate with wider background windows. The deconvolution of the background needs to be done using the Fourier ratio method when dealing with well separated low loss and high loss spectral energy ranges in DualEELS. The background subtraction and deconvolution functioned remarkably well for this data and the quality of the edge is very high. As a result of this, the MLLS fit also produces an almost perfect fit to the real sample, with a composition of Zr cation of $47.3 \pm 0.6\%$. This agrees well with independent measurements of the composition by Rutherford Backscattering and demonstrates that there was a large deviation in this case from the target composition of 34.5 % Z

5. Conclusion and Future Work

The detection of gravitational waves has been one of the most challenging experimental projects ever to be undertaken. The most successful experiments in this area are essentially Michelson interferometers, with the arms having a length of kilometres. The first-ever experiment of this kind to actually and conclusively detect gravitational waves is Advanced LIGO, the core optical configuration of which comprises a beam-splitter and mirrors. Fabry-Perot cavities as well as power recycling and signal recycling mirrors at the input and output ports are also included in the necessary optics elements. An essential part of all these optical systems is the reflecting multilayer coatings on the optical surfaces of the test mirrors at the two arm ends.

Thermal noise arising from the mechanical loss in the mirror coatings is an important limiting factor for the sensitivity of gravitational wave detectors. Doping the high index Tantalum (Ta_2O_5) layers with Titania (TiO_2) is already known to reduce mechanical loss and has been implemented in a LIGO. In order to better understand the mechanisms behind this improvement, and thereby to further improve coatings, we need to understand the atomic structure of the coatings. One critical input for any such atomic structure modelling is the composition of the coating. This thesis specifically focuses on the accurate and precise determination of the composition of such coatings using electron energy-loss spectroscopy (EELS).

Traditional EELS quantification is based on: (i) fitting a background in front of the edge of interest and subtracting this; (ii) Integrating over some suitable window; (iii) converting to atomic amounts using a calculated cross section; and (iv) convert to relative percentage (%) (Egerton, section 4.50). This all fails for the coatings of interest for Advanced LIGO and future room temperature detectors. Current A-LIGO coatings are based on Ta_2O_5 - TiO_2 which have been shown to reduce mechanical loss, while Ta_2O_5 - ZrO_2 is one composition of interest for a future upgrade.

Quantifying the Ta₂O₅-TiO₂ is difficult for several reasons, (i) the best choice of edges is the Ta-N_{4,5} at 229 eV and the Ti-L_{2,3} at 456 eV, as they are close in energy; (ii) there is a wiggly background before the Ta-N_{4,5} edge because of EXELFS from low-lying edges, which makes background subtraction uncertain and rather dependent on the judgement of the user; (iii) there is a low signal-to-background ratio, so longer counting times are needed per spectrum in order to see the edge well; and (iv) no theoretical Ta-N_{4,5} cross section exists, because there is no Hartree-Slater type calculation currently in existence for N-edges. With all these challenges, it is possible to do a modified traditional quant using an experimentally determined cross section (as in previous work and my own initial work), but this produces very noisy results, and the background extrapolation issue (ii) makes them subject to large systematic errors.

Quantifying the Ta₂O₅-ZrO₂ is difficult for several reasons if the traditional method is used because: (i) The best energy range to get Ta and Zr edges in the same spectrum is to use a higher energy range over 1500 eV to get Ta-M (1735 eV onset) and Zr-L (2222 eV onset) edges, this causes challenges in the electron optics; (ii) the Ta-M₃ edge sits just before the Zr-L₃ edge, so background subtraction is impossible for Zr; (iii) the calculated Ta-M cross section is probably unreliable (most calculated M-cross sections are too high for at least 200 eV after the edge); and (iv) Zr is probably strongly modified by white lines.

In summary, EELS data may be useful for quantifying Ta₂O₅-TiO₂ and Ta₂O₅-ZrO₂ systems, but better methods are needed to quantify it. The key idea in the research presented in this thesis is instead of using traditional background subtraction and integration, to fit the spectrum as a linear combination of standards using multiple linear least squares (MLLS) fitting.

In order to do this, some practicalities need to be attended to. The raw data needs to be collect using DualEELS so that energy alignment, deconvolution, and normalisation with the zero loss intensity are possible. It is known the raw data will contains a large amount of random noise, as well as systematic errors due to the microscope and spectrometer. Before any useful information about the composition of the element in the acquired thin film data can be obtained, the raw data must be processed and analysed. The initial processing deals with

reducing both the volume of the datasets and the amount of noise within them present using methods such as Principal Component Analysis. This is then followed by removing plural scattering within the specimen from the datasets using a Fourier-log deconvolution method, when working with the lower loss $\text{TiO}_2\text{-Ta}_2\text{O}_5$ datasets, or Fourier-ratio deconvolution when analysing higher loss $\text{ZrO}_2\text{-Ta}_2\text{O}_5$ datasets. When working with low loss data, it is useful to correct any non-linearity in the energy scale. When working with high loss energy ranges, it is better to use specially designed camera lengths to give optimal transfer of energy loss electrons into the spectrometer and thus well-behaved background shapes. The final analysis step is the need for suitable standard samples of known chemistry and structure that are a close match to the sample to be quantified.

The process of quantifying $\text{Ta}_2\text{O}_5\text{-TiO}_2$ was done by testing several possible standards for Ti, namely SrTiO_3 , TiC and amorphous TiO_2 . All gave different near edge structure. In order to determine which is the best standard to use, the near edge structure of the calculated interaction cross section of the edge was compared with the edge shape for the real sample, and the best fit was determined, which was for amorphous TiO_2 . The same procedure was also carried out in order to determine the best cross section for Ta. Two possible standards for Ta were tested. LiTaO_3 and Ta_2O_5 glass gave totally different ELNES and the latter was much better for Ta_2O_5 -based glasses. A MLLS fit was then performed. It was found that the fitting worked really well for four samples, nominally 25% and 55% Ti, using two standards for amorphous TiO_2 and Ta_2O_5 glass, although a slight deviation from the correct background shape was found in the fit residuals in all cases. The fitting worked even better if an extra background shape was added to the fit, and residuals were then very low. This then resulted in very precise quantifications and provided much lower random uncertainty than previous work on EELS quant of Ta-Ti oxide glasses. Some small variability was noted between different samples of nominally the same composition in this research, which needs more investigation (is this real, or some systematic effect between different datasets). The absolute numbers of, e.g. 11.2 ± 0.1 % Ti seem more reliable than previous published ones (14 ± 3 % Ti), and rather lower than the target composition of 25% Ti. The nominally 55% Ti specimen was found to actually be 43.9 ± 2.3 % Ti. It is not currently possible to compare these to independent measurements by

other techniques, although it would naturally be good to make such tests in due course.

Quantifying Ta₂O₅-ZrO₂ need to used optimised high loss camera lengths to give well behaved backgrounds. For this thin film, the process is less complicated as there are just two standard for two main element to be process, which is Ta-M_{4,5} and Zr-L_{2,3} the two standards are amorphous Ta₂O₅ and monoclinic ZrO₂. These fitted well to the data with no further correction, and the background extrapolation was excellent. The results are excellent with low random variation and give a result of 47.3 ± 0.6 % Ti agrees to better than 1 % with measurements of the same film using Rutherford Backscattering (RBS) of 48.1 ± 0.1 % Ti (Kiran Prasai et al., n.d.), and the percentage is inside error limits on that measurement. This, we can have great confidence in the quality of these measurements and in the reliability of the analysis technique developed here.

For the future work in order to improve the quantification and study of the samples, it is vital to measure a-LIGO witness sample (a sample of the same substrate as the actual test masses, and deposited alongside them in the same coating run) and get an exact map of content in the 15 repeat multilayer coating. Besides that, by doing cross correlation of results on Ta-Ti-O to other techniques such as RBS, or EDX with absolute standards improve our certainty about the reliability of these results. The study on Ta-Zr-O should be extended by measuring Ta-Zr contents across a wider composition range (only one sample was available in this work), especially down to lower Zr contents around 25%, since this will be a target composition for a next generation film. Further research should also use the cross sections developed here and automate the methods for faster analysis turnaround in future. Whilst this work has focused solely on Ta₂O₅ thin films, the methods developed herein should be fruitful for the quantification of a range of other mixed oxide systems, for example HfO₂-SiO₂ and Nb₂O₅-Ta₂O₅, which have also been considered for dielectric multilayer mirrors.

Bibliography

- Abbott, B. P. et al., 2016. *Observation of Gravitational Waves from a Binary Black Hole Merge*. Phys. Rev. Letters, **116**(1), p. 061102.
- Abbott, B. P. et al., 2016. *Binary Black Hole Mergers in the first Advanced LIGO Observing Run*. Phys. Rev.X **6**(1), 041015.
- Abbott, B. P. et al., 2016. *The basic physics of the binary black hole merger GW150914* (LIGO and Virgo Scientific Collaboration).
- Advanced LIGO team 2007. Advanced LIGO reference design. Technical report, LIGO Laboratory. <https://labcit.ligo.caltech.edu/~dhs/Adv-LIGO/old/main-p.pdf>
- Agresti, J., Castaldi, G., DeSalvo, R., Galdi, V., Pierro, V. and Pinto, I.M., 2006. *Optimised multilayer dielectric mirror coatings for gravitational wave interferometers*. Proceedings of the SPIE.
- Ahn, C. C. and Krivanek, O., 1983. *EELS Atlas*. Gatan Inc. Warrendale, PA.
- Ahn, C. C., 2004. *Transmission Electron Energy Loss Spectrometry in Materials Science and the EELS Atlas*. 2nd ed., Wiley.
- Anderson, I.M., 1998. Multivariate statistical analysis of low-voltage EDS spectrum images. *Microsc Microanal* **4**(2), 272.
- Annand, K. J., Maclaren, I., and Gass, M. 2015. *Utilising DualEELS to Probe the Nanoscale Mechanisms of the Corrosion of Zircaloy-4 in 350°C Pressurised Water*. *Journal of Nuclear Materials* **465**: 390-99.
- Bach, D., 2010, *EELS investigations of stoichiometric niobium oxides and niobium-based capacitors*. PhD Thesis
- Bach, D., Schneider, R., Gerthsen, D., Verbeeck, J., and Sigle, W., 2018. *Microscopy Microanalysis EELS of Niobium and Stoichiometric Niobium-Oxide Phases Part I: Plasmon and Near-Edges Fine Structure*. 505-23.
- Bassiri, R., Borisenko, K.B., 2010. *Probing the atomic structure of amorphous Ta₂O₅ mirror coatings for advanced gravitational wave detectors using transmission electron microscopy*. *J. Phys. Conf. Ser.*, **241**, 012070.
- Bassiri, R., Borisenko, K.B., 2011. *Probing the atomic structure of amorphous Ta₂O₅ coatings*. *Appl. Phys. Lett.*, **98**, 031904.
- Bassiri, R., 2011, *The atomic structure and properties of mirror coatings for use in gravitational wave detectors*. PhD thesis, University of Glasgow

- Bassiri, R. et al., 2013, *Investigating the medium range order in amorphous Ta₂O₅ coatings*. *Journal of Physics Conference Series*, **522**, 012043
- Bassiri, R. et al., 2015. *Order within disorder: The atomic structure of ion-beam sputtered amorphous tantalum (a-Ta₂O₅)*. *APL Materials*, **3**, 036103.
- Bertoni, G., E. Beyers, J. Verbeeck, M. Mertens, P. Cool, E. F. Vansant, and G. Van Tendeloo., 2006. *Quantification of Crystalline and Amorphous Content in Porous TiO₂ Samples from Electron Energy Loss Spectroscopy*. *Ultramicroscopy* 106 (7): 630-35.
- Bobyanko, J., 2018, *Characterisation and absolute quantification of nanosised V and Nb precipitates in high manganese steel using DualEELS*. PhD thesis, University of Glasgow
- Bobyanko, J., MacLaren, I. & Craven, A.J., 2015. *Spectrum imaging of complex nanostructures using DualEELS: I. digital extraction replicas*. *Ultramicroscopy*, 149, pp.9-20.
- Bochner, B., 1998. *Modelling the Performance of Interferometric Gravitational/WaveDetectors with Realistically Imperfect Optics*. PhD thesis, Massachusetts Institute of Technology.
- Bondu, F. and Vinet, J. Y., 1995. *Mirror thermal noise in interferometric gravitational wave detectors*. *Phys.Lett.A*, **198**,74
- Bondu, F., Hello, P. and Vinet, J. Y., 1998. *Thermal noise in mirrors of interferometric gravitational wave antennas*. *PhysLett.A* **246**, 227
- Braginsky V. B. and Vyatchanin, S. P., 2003. *Thermodynamical fluctuations in optical mirror coatings*. *Phys. Lett. A*, **312**, 244
- Brydson, R., 2001. *Electron energy loss spectroscopy*. Microscopy Handbooks, Vol.50 .
- Buonanno, A., 2007. *Gravitational Waves*. arXiv:0709.4682 [gr-qc].
- Carroll, S., 2003. *Spacetime and Geometry: An Introduction to General Relativity*". Benjamin Cummings.
- Carter, C.B. and Williams B.B., 2016. *Transmission Electron Microscopy, Diffraction, Imaging, and Spectroscopy*". Springer.
- Castaldi, G. et al., 2007. *Coating design optimization for advanced interferometers: Minimizing the total noise budget*. *LSC-Virgo joint meeting*, Cascina, (PI), Italy LIGO-G070309-00-Z.
- Choi, Eun Mi, Thomas Fix, Ahmed Kursumovic, Christy J. Kinane, Darío Arena, Suman Lata Sahonta, Zhenxing Bi, et al., 2014. *Room Temperature*

- Ferrimagnetism and Ferroelectricity in Strained, Thin Films of BiFe_{0.5}Mn_{0.5}O₃*. *Advanced Functional Materials*. 24 (47): 7478-87.
- Craven, A. J., and Buggy T. W., 1981. *Design Considerations and Performance of an Analytical STEM*.7: 27-37.
- Craven, A. J., Sawada H., McFadzean, S., and MacLaren, I., 2017. *Getting the most out of a post-column EELS spectrometer on a TEM/STEM by optimising the optical coupling* *Ultramicroscopy* 180: 66-80.
- Craven, A.J., Bobynko, J., Sala, B., and MacLaren. I., 2016. *Accurate measurement of absolute experimental inelastic mean free paths and EELS differential cross-sections*. *Ultramicroscopy*, 170, pp.113-127.
- Craven, A. J., Sala, B., Bobynko, J., and Ian MacLaren., 2018. *Spectrum Imaging of Complex Nanostructures Using DualEELS: II. Absolute Quantification Using Standards*. *Ultramicroscopy* 186: 66-81.
- Craven, A. J., Sawada, H., McFadzean, S., and MacLaren. I., 2017. *Getting the Most out of a Post-Column EELS Spectrometer on a TEM/STEM by Optimising the Optical Coupling*. *Ultramicroscopy* 180: 66-80.
- Cutler, C. and Thorne, K.S., 2002. *An overview of gravitational-wave sources*. *General Relativity and Gravitational*, pp.72-111.
- DigitalMicrograph EELS Analysis User's Guide (2003).
- Edelstein, W.A., Hough, J., Pugh, J.R. and Martin, W., 1978. *Limits to the measurement of displacement in an interferometric gravitational radiation detector*. *J. Phys.E*, 11(7), 710.
- Egerton, R.F., 2016. *Physical Principles of Electron Microscopy*. 2nd Ed., Springer, Switzerland.
- Egerton. R. F., 1996. *Improvement of the Hydrogenic Model to Give More Accurate Values of K-Shell Ionization Cross Sections*. *Ultramicroscopy* 63 (1): 11-13.
- Egerton, R. F., 2011. *Electron Energy-Loss Spectroscopy in the Electron Microscope* Third Edit., New York Springer.
- Egerton, R. F., and Cheng. S. C., 1987. *Measurement of Local Thickness by Electron Energy-Loss Spectroscopy*. *Ultramicroscopy* 21 (3): 231-44.
- Egerton, R. F., Wang, F., Malac, M., Moreno, M. S.. and Hofer. F., 2008. *Fourier-Ratio Deconvolution and Its Bayesian Equivalent*. *Micron* 39 (6): 642-47.
- Egerton, R.F., and Malac. M., 2005. *EELS in the TEM*. *Journal of Electron Spectroscopy and Related Phenomena* 143 (2-3): 43-50.

- Einstein, A., 1916. *Approximative Integration of the Field Equations of Gravitation*. Preuss. Akad. Wiss. Berlin, Sitzber. 688
- Einstein, A., 1918. *On Gravitational Waves*. Preuss. Akad. Wiss. Berlin, Sitzber. 154
- Fine, M.E., van Duyne, H., Kenney, N.T., 1954. *Low-temperature internal friction and elasticity effects in vitreous silica*. J. Appl. Phys., **25**, 402.
- Flaminio, R. et al., 2010. *A study of coating mechanical and optical losses in view of reducing mirror thermal noise in gravitational wave detectors*. Class and Quant Gravity, **27(8)**, 84030.
- Foot, C.J., 2005. *Atomic Physics*. Oxford University Press, Oxford, UK
- Franc, J., et al., 2009. *Mirror thermal noise in laser interferometric gravitational wave detectors operating at room and cryogenic temperature*. Einstein Telescope note ET-021-09
- Gatan Microscopy Suite Software, available at <http://www.gatan.com/products/tem-analysis/gatan-microscopy-suite-software>
- Goodman, J.W., 1968. *Introduction to Fourier Optics*. McGraw-Hill
- Groves, T.R., 2005. *Charged Particle Optics Theory*. CRC Press, Boca Raton, FL.
- Gubbens, A. et al., 2010. *The GIF Quantum, a next generation post-column imaging energy filter*. Ultramicroscopy, 110(8), pp.962-970
- Hamdan, R., Trinastic, J.P., Cheng, H.P., 2014. *Molecular dynamics study of the mechanical loss in amorphous pure and doped silica*. J. Chem. Phys., **141**, 054501.
- Harry, G. M., Abernathy, M. R., Becerra-Toledo, A. E., Armandula, H., Black, E., Dooley, K., Eichenfield, M., Nwabugwu, C., Villar, A., Crooks, D. R. M., Cagnoli, G., Hough, J., How, C. R., et al. 2006. *Titania-Doped Tantalum/Silica Coatings for Gravitational-Wave Detection*. Class. Quantum Grav. 24 (40).
- Harry, G. M., Andri, M. G., Peter, R. S., Steven, D. P., Peter, H. S., Helena, A., Joseph, C. B., et al. 2003. "Classical and Quantum Gravity Related Content Mechanical Loss in Tantalum / Silica Dielectric Mirror Coatings Mechanical Loss in Tantalum / Silica Dielectric Mirror Coatings.
- Harry, G. M. et al., 2002. *Thermal noise in interferometric gravitational wave detectors due to dielectric optical coatings*. Class.Quant.Grav., **19(5)**, 897

- Harry, G. M., 2004. *Encorporating coating anisotropy into coating thermal noise*. Technical Report T040029-00-R, LIGO.
- Hart, M. J., 2017, *Amorphous mirror coatings for ultra-high precision interferometry*. PhD Thesis, University of Glasgow.
- Horn, M., Schwerdtfeger, C. F., and Meagher, E.P. 2010. *Refinement of the structure of anatase at several temperatures*. Zeitschrift für Kristallographie-Crystalline Material. 163 (3-4).
- Iakoubovskii, K., Kazutaka, M., Yoshiko, N., and Kazuo, F. 2008. *Mean Free Path of Inelastic Electron Scattering in Elemental Solids and Oxides Using Transmission Electron Microscopy: Atomic Number Dependent Oscillatory Behavior*. Physical Review B - Condensed Matter and Materials Physics 77 (10): 1-7.
- Jeanguillaume, C. & Colliex, C., 1989. *Spectrum-image: The next step in EELS digital acquisition and processing*. Ultramicroscopy, 28(1-4), pp.252-257.
- JEOL Co., Glossary of TEM terms, available at <http://jeol.co.jp>
- Kizilyaprak, C., Daraspe, J. & Humbel, B.M., 2014. *Focused ion beam scanning electron microscopy in biology*. Journal of Microscopy, Vol. 254, Issue 3, pp. 109-114.
- Kokkotas, K. D., 2002. *Gravitational Wave Physics*. In Encyclopedia of Physical Science and Technology, Academic Press.
- Larson, A. C., D. T. Cromer, and R. B. Roof. 2002. *The Crystal Structure of the High Temperature Form of PuGa₃*. Acta Crystallographica 18 (2): 294-95.
- Leapman, R. D., Swyt, C. R., 1988. *Separation of overlapping core edges in electron energy loss spectra by multiple-least-squares fitting*. Ultramicroscopy, 26, 393.
- LIGO Collaboration, <http://www.ligo.caltech.edu/>
- Liu, X. Q., X. D. Han, Z. Zhang, L. F. Ji, and Y. J. Jiang., 2007. *The Crystal Structure of High Temperature Phase Ta₂O₅*. Acta Materialia 55 (7): 2385-96.
- Luo, Z., 2016. *A Practical Guide to Transmission Electron Microscopy*. 2 vols, Momentum Press, New York, NY. LISA experiment collaboration, <http://lisa.jpl.nasa.gov/>
- MacLaren, I., B. Sala, S. M.L. Andersson, T. J. Pennycook, J. Xiong, Q. X. Jia, E. M. Choi, and J. L. MacManus-Driscoll., 2015. *Strain Localization in Thin Films of Bi(Fe,Mn)O₃ Due to the Formation of Stepped Mn⁴⁺-Rich Antiphase*

- Boundaries*. *Nanoscale Research Letters* 10 (1).
- MacLaren, I., Kirsty, J. A., Colin, B., and Craven, A. J., 2018. EELS at Very High Energy Losses. *Microscopy* 67 (September 2017): i78-85.
- Malis, T., Cheng, S. C., and Egerton, R. F. 1988. *EELS Log-ratio Technique for Specimen-thickness Measurement in the TEM*. *Journal of Electron Microscopy Technique* 8 (2): 193-200.
- Reid, S., and Martin, I., 2018. *Development of Mirror Coatings for Gravitational-Wave Detectors*. *Philosophical Transactions of the Royal Society A: Mathematical, Physical and Engineering Sciences* 376 (2120). <https://doi.org/10.1098/rsta.2017.0282>.
- Maggiore, M., 2014. *Gravitational Waves: Theory and Experiments*. Oxford University Press.
- Martin, I. W., Armandula, H., et al., 2008. *Measurements of a low-temperature mechanical dissipation peak in a single layer of Ta₂O₅ doped with TiO₂*. *Class. Quantum Gravity*, **25**, 055005.
- Martin, I. W., Chalkley, E., Nawrodt, R., et al., 2009. *Comparison of the temperature dependence of the mechanical dissipation in thin films of Ta₂O₅ and Ta₂O₅ doped with TiO₂*. *Classical and Quantum Gravity*, Vol.26(15).
Class. Quantum Gravity, **26**, 155012.
- Misner, C. W., Thorne, K. S. and Wheeler J., 1973. *Gravitation*. W. H. Freeman, San Francisco
- Ni, N., et al., 2011. *Quantitative EELS analysis of zirconium alloy metal/oxide interfaces*. *Ultramicroscopy*. 111(2): p. 123-130.
- Nowick, A.S., Berry, B.S., 1972. *Mechanical Models and Discrete Spectra*". In *Anelastic Relaxation in Crystalline Solids*, Academic Press, New York, NY, USA.
- Okada, M., Ping, J., Yasusei, Y., Masato, T., and Kazuki, Y., 2004. *Low-Energy Electron Energy Loss Spectroscopy of Rutile and Anatase TiO₂ Films in the Core Electron Excitation Regions*. *Surface Science* 566-568 (1-3 PART 2): 1030-34.
- Penn, S. D. et al., 2003. *Mechanical loss in tantala/silica dielectric mirror coatings*. *Class. Quantum Grav.*, **20**, 2917
- Penn, S. D., .et al., 2006a. *Frequency and surface dependence of the mechanical loss in fused silica*. *Phys. Lett. A*, **352(1-2)**, 3

- Penn, S. D. et al., 2006. *Experimental measurements of mechanical dissipation associated with dielectric coatings formed using SiO₂, Ta₂O₅, and Al₂O₃*. *Class. Quantum Grav.*, **23**, 4953
- Portland State University, *FEI Tecnai T20 Operations Manual*, 2010
- Prasai, K., Jiang, J., et al., 2019. *Supplementary information - High precision detection of change in intermediate range order of amorphous zirconia-doped tantala thin films due to annealing*.
- Prasai, K., Jiang, J., et al., 2019. *High precision detection of change in intermediate range order of amorphous zirconia-doped tantala thin films due to annealing*.
- Principe, M., DeSalvo, R., et al., 2008. *Minimum Brownian Noise Dichroic Dielectric Mirror Coatings for AdLIGO*. LIGOT080337 internal note
- Rakhmanov, M., 2000. *Dynamics of Laser Interferometric Gravitational Wave Detectors*. PhD thesis, California Institute of Technology.
- Rao, S. R., 2003. *Mirror Thermal Noise in Interferometric Gravitational-Wave Detectors*. PhD thesis, California Institute of Technology.
- Reid, S., Martin, I.W., 2016. *Development of Mirror Coatings for Gravitational Wave Detectors*. *Coatings*, **6**, 61.
- Rez, P., 1982. *Cross-sections for energy-loss spectrometry*. *Ultramicroscopy*. **9**,283
- Riles, K., 2013. *Gravitational Waves: Sources, Detectors and Searches*. *Prog. in Part. and Nucl. Phys.* **68**, 1.
- Saulson, P. R., 1994. *Fundamentals of Interferometric Gravitational Wave Detectors*. World Scientific
- Saulson, P. R., 1990. *Thermal noise in mechanical experiments*. *PhysRevD* **42**,2437
- Schutz, B. F., 1984. *Gravitational Waves On The Back Of An Envelope*. *Am.J.Phys.* **52**, 412-419.
- Schutz, B. F., 1996. *Gravitational-wave sources*. *Class. Quantum Grav.* **13** A219
- Schutz, B. F., 1999. *Gravitational wave astronomy*. *Class.Quant.Grav.* **16**, A131.
- Schutz, B. F. and Ricci, F., 2010. *Gravitational Waves, Sources, and Detectors*. arXiv:1005.4735.
- Scott, J. et al., 2008. *Near-simultaneous dual energy range EELS spectrum imaging*. *Ultramicroscopy*, 108(12), pp.1586-1594.

- Somiya, K. for the KAGRA Collaboration, 2012. *Detector configuration of KAGRA the Japanese cryogenic gravitational-wave detector*. *Class. Quantum Grav.* **29**, 124007.
- Tran, T.T., 2017. *Synthesis of Germanium-Tin Alloys by Ion Implantation and Pulsed Laser Melting: Towards a Group IV Direct Band Gap Semiconductor*. PhD Thesis Uppsala University.
- Trinastic, J.P., Hamdan, R., Billman, C., Cheng, H. P., 2016. *Molecular dynamics modeling of mechanical loss in amorphous tantala and titania-doped tantala*. *Phys. Rev.*, **B93**, 014105.
- University of Sydney, (2012) <https://myscope.training>
- Verbeeck, J. & Van Aert, S., 2004. *Model based quantification of EELS spectra*. *Ultramicroscopy*, 101(2-4), pp.207-224.
- Verbeeck, J., Van Aert, S. & Bertoni, G., 2006. *Model-based quantification of EELS spectra: Including the fine structure*. *Ultramicroscopy*, 106(11-12 SPEC. ISS.), pp.976-980.
- Villar, A.E., Black, E.D., Desalvo, R., et al., 2010. *Measurement of thermal noise in multilayer coatings with optimised layer thickness*. *Phys. Rev.*, **D81**, 122001.
- Vinet, J. Y., 2005. *Mirror thermal noise in flat-beam cavities for advanced gravitationalwave interferometers*. *Class. Quantum Grav.*, **22**,1395
- Virgo Collaboration, <http://www.virgo.infn.it/>
- Virgo Collaboration, 2010. *The virgo physics book, vol. ii: Optics and related topics*. Technical Report, VIRGO.
- Wang, L., 2013. *Quantitative three dimensional atomic resolution characterization of non-stoichiometric nanostructures in doped bismuth ferrite*. PhD Thesis University of Glasgow.
- Wang, Y. et al., 2018. *Towards atomically resolved EELS elemental and fine structure mapping via multi-frame and energy-offset correction spectroscopy*. *Ultramicroscopy*, **184B**, 98
- Weber, J., 1969. *Anisotropy and polari sation in the gravitational-radiation experiments*. *Phys. Rev. Lett.*, **22**, 1320.
- Weidersich, J., Adichtchev, S.V., Rossler, E., 2000. *Spectral Shape of Relaxations in Silica Glass*. *Phys. Rev. Lett.*, **84**, 2718.
- Weisberg, J. M. and Huang, Y., 2003. *Relativistic measurements from timing the binary pulsar psr b1913+16*. *The Astrophysical Journal* **829(1)**, 55.

Williams, D. B. and Carter, C. B., 2009. *Transmission Electron Microscopy, A Textbook for Materials Science*, 2nd ed., Springer.

Appendix A

Script to measure and correct the spectrometer dispersion non-linearity (by Mr. R. Webster)

```
// $BACKGROUND$
////////////////////////////////////
//          Dispersion Non-Linearity Processing Script
//
//          Robert Webster, April 2018
////////////////////////////////////
////////////////////////////////////
//          ANY GLOBAL PARAMETERS HERE
////////////////////////////////////
////////////////////////////////////
//          EXTRACT ZLP MAPS
////////////////////////////////////
void ZLPGauss()
{
    image LL, HL
    GetTwoLabeledImagesWithPrompt("Choose Input Images", "Choose reference Low-Loss and
dispersion High-Loss images.", "Low-Loss", LL, "High-Loss", HL)
    image ref, disp
    ref:= LL.ImageClone()
    disp:= HL.ImageClone()
    number ZLPshiftStepCh = 10 //Ask what the channel step in the experiment was (this
should be implemented as a tag in future)
    taggroup acquitags
    acquitags = LL.ImageGetTagGroup()
    if(!acquitags.TaggroupGetTagAsNumber("Test          Notes:ChStep", ZLPshiftStepCh))
if(!GetNumber("Tag not found. How many channels were stepped?", ZLPshiftStepCh,
ZLPshiftStepCh)) exit(0)

    number x, y
    ref.GetSize(x,y)
    number RHSlim = 20 //Ask what the right hand channel limit was in the experiment (future
tag).
    if(!acquitags.TaggroupGetTagAsNumber("Test          Notes:RHS          Buffer", RHSlim))
if(!GetNumber("Tag not found. What right channel limit was used in acquisition?", RHSlim, RHSlim))
exit(0)

    //////////////////////////////////////
    //          SINGLE CHANNEL PRECISION
    //////////////////////////////////////
    image roughRefCh = ReallImage("Max Pixel Location",4,y,1)
    image roughDispCh = ReallImage("Max Pixel Location",4,y,1)
    //First, we locate the maximum pixel position in each frame and collate
    //that in a single image.
    number usedCh = 0
    number i
    for(i=0;i<y;i++)
    {
        number refX, dispX, throwaway
        max(ref.slice1(0,i,0,0,x,1),refX,throwaway)
        max(disp.slice1(0,i,0,0,x,1),dispX,throwaway)

        //result("Peaks found at "+refX+" and "+dispX+"\n")
        roughRefCh.SetPixel(i,0,refX)
        roughDispCh.SetPixel(i,0,dispX)
    }
}
```

```

        if(roughRefCh.GetPixel(i,0)!=0.0) usedCh++
    }
    //Having extracted each peak position, want to determine offsets using
    //reference positions. Will allow us to calculate deviation
    image deviations = ReallImage("Pixel Accurate Deviations",4,usedCh,1)
    for(i=0;i<usedCh;i++)
    {
        if(roughRefCh.GetPixel(i,0)!=0.0)
        {
            //determine the position of the peak relative to its' reference to get
            deviation from ideal conditions
            number dev = roughDispCh.GetPixel(i,0) - roughRefCh.GetPixel(i,0) +
i*ZLPshiftStepCh
            deviations.SetPixel(i,0,dev)
        }
    }
    deviations.SetName("Single Pixel Deviations")
    deviations.FlipHorizontal()
    deviations.ImageSetDimensionScale(0,ZLPshiftStepCh)
    number origin = (x-RHSlim)-(usedCh-1)*ZLPshiftStepCh
    deviations.ImageSetDimensionOrigin(0,origin)
    deviations.ImageSetDimensionUnitString(0,"CCD Channels")
    deviations.ImageSetIntensityUnitString("# Channel Deviation from linearity")
    deviations.ShowImage()
    if(!OKCancelDialog("Enhance with sub-pixel precision measurement? (Note, the maps
output by this step are centred on the rough peak position. If using maps for gaussian fit after
script ends, you will need to add the single pixel deviations to the result to obtain the correct
dispersion.") exit(0)
    //////////////////////////////////////
    //          SUB-PIXEL PRECISION
    //////////////////////////////////////
    //To execute this, we need to fit a gaussian to each peak to find the centre.
    //To do that, we want to shift all the peaks by the expected drift tube offset
    //The measured peak positions should then characterise the deviation as before

    //The window we want to slice out of the dataset will then be twice this value
    number buffer = 0 // increases the window size if necessary to capture all features.
    //Note, too large a buffer will result in probing outside the dataset.
    number window = 2 * RHSlim + buffer
    //We need to set up an image which the windowed slices will be dropped into
    image subDisp = ReallImage("Extracted disp ZLPs",4>window,usedCh)
    image subRef = ReallImage("Extracted ref ZLPs",4>window,usedCh)
    //now we can start transferring data into this image
    for(i=0;i<usedCh;i++)
    {
        //The next 30 lines provide a set of checks and balances for centering the window
        //about the rough ZLP position. Ensures that the resultant image can be properly
calibrated
        //and also that no pixels outside the image are referenced.
        number refLow = roughRefCh.GetPixel(i,0) - (window/2)
        number dispLow = roughDispCh.GetPixel(i,0) - (window/2)
        number refHigh = refLow + window
        number disphigh = dispLow + window
        number refPad = 0
        number dispPad = 0
        number refSize = window
        number dispSize = window
        if(refLow < 0)
        {
            refPad = -refLow
            refLow = 0
            refSize = window - refPad

```

```

    }
    if(dispLow < 0)
    {
        dispPad = -dispLow
        dispLow = 0
        dispSize = window - dispPad
    }
    if(refHigh > x)
    {
        refSize = window - (refHigh - x)
        refHigh = x
    }
    if(dispHigh > x)
    {
        dispSize = window - (dispHigh - x)
        dispHigh = x
    }
    //Now that we have determined it is safe to pick out and move slices, it's time to
do just that
    image dispSlice = disp.slice1(dispLow,i,0,0,dispSize,1)
    image refSlice = ref.slice1(refLow,i,0,0,refSize,1)
    subDisp[i,dispPad,i+1,dispSize+dispPad] = dispSlice
    subRef[i,refPad,i+1,refSize+refPad] = refSlice
}
//Now that this has been extracted, we want to set up images to have the proper
calibration
subRef.ImageSetDimensionOrigin(0,-window/2)
subDisp.ImageSetDimensionOrigin(0,-window/2)
subRef.FlipVertical()
subDisp.FlipVertical()
subRef.ImageSetDimensionScale(1,ZLPshiftStepCh)
subRef.ImageSetDimensionOrigin(1,x-RHSlim-(usedCh-1)*ZLPshiftStepCh)
subDisp.ImageSetDimensionScale(1,ZLPshiftStepCh)
subDisp.ImageSetDimensionOrigin(1,x-RHSlim-(usedCh-1)*ZLPshiftStepCh)
subDisp.ImageSetDimensionUnitString(1,"CCD Channels")
subRef.SetName("Cropped Reference ZLPs")
subRef.SetStringNote( "Meta Data:Format","Spectrum image" )
subRef.SetStringNote( "Meta Data:Signal","EELS" )
subDisp.SetName("Cropped Dispersion ZLPs")
subDisp.SetStringNote( "Meta Data:Format","Spectrum image" )
subDisp.SetStringNote( "Meta Data:Signal","EELS" )
//subRef.ShowImage()
//subDisp.ShowImage()
image subPixDist := deviations.ImageClone()
number StartTick, EndTick
StartTick = GetHighResTickCount()
//Implement Gaussian Fit
for(i=0;i<usedCh;i++)
{
    //extract slices
    image RS, DS
    RS:=subRef.slice2(0,i,0,0>window,1,1,1,1).ImageClone()
    DS:=subDisp.slice2(0,i,0,0>window,1,1,1,1).ImageClone()
    image eR:=RS.ImageClone()
    eR=1.0
    image eD := eR.ImageClone()
    number AR, midR, widR, chisqR, convR, AD, midD, widD, chisqD, convD
    convR = 0.00001
    chisqR=1e6
    convD = convR
    chisqD = chisqR
    number DXP, RXP, hold

```

```

        number epch = RS.ImageGetDimensionScale(0)
        aR = max(RS,RXP,hold) //amplitude component
        midR = RXP - window/2//xp*scale1+origin1 //center position
        widR = 1/epch //guestimate FWHM
        aD = max(DS,DXP,hold) //amplitude component
        midD = DXP - window/2//xp*scale1+origin1 //center position
        widD = 1/epch //guestimate FWHM
        number okR = FitGaussian(RS,eR,aR,midR,widR,chisqR,convR)
        number okD = FitGaussian(DS,eD,aD,midD,widD,chisqD,convD)
        subPixDist[i,0] = midD - midR + deviations.GetPixel(i,0)
        number prog = round(i/usedCh*100)
        if(remainder(i,floor(usedCh/10))==0) result("ZLP fit is "+prog+"% complete\n")
    }
    subPixDist.SetName("Result of Gaussian Fits")
    subPixDist.ShowImage()
    deviations.DeleteImage()
    EndTick = GetHighResTickCount()
    number elapsedTime = ( EndTick - StartTick ) / GetHighResTicksPerSecond()
    Result("\nZLP Fit complete - duration: " + elapsedTime + " sec\n\n" )
}
////////////////////////////////////
//          RUN FITTING PROCEDURES
////////////////////////////////////
void PolyReg()
{
    if(!OKCancelDialog("Ensure trend to be fitted is front-most image.")) exit(0)
    image data := GetFrontImage().ImageClone()
    image errors := data.ImageClone()
    errors = 1.0
    number chisq = 1e6
    number conv = 1e-8
    image pars:=NewImage("Poly Pars",2,6,1)
    pars = -5
    image parsToFit:=NewImage("tmp",2,6,1)
    parsToFit = 1
    number ok = FitPolynomial(data, errors, pars, parsToFit, chisq, conv)
    pars.SetName("Fit Coefficients")
    pars.ShowImage()
    image output:=data.ImageClone()
    number i,j,scale,orig
    orig = data.ImageGetDimensionOrigin(0)
    scale = data.ImageGetDimensionScale(0)
    for(i=0;i<output.ImageGetDimensionSize(0);i++)
    {
        number outval = 0
        for(j=0;j<pars.ImageGetDimensionSize(0);j++)
            outval += (((i*scale)+orig)**j)*pars.GetPixel(j,0)
        output[i,0] = outval
    }
    output.SetName("Fit Result")
    output.ShowImage()
    DeletePersistentNote("EELSDispersion:NonLinFit")
    for(i=0;i<6;i++)
    {
        SetPersistentNumberNote("EELSDispersion:NonLinFit:a"+i,pars.GetPixel(i,0))
    }
}
}
void Implement()
{
    Image O_LL, O_HL, R_LL, R_HL, RCE_LL, RCE_HL, RCECI_LL, RCECI_HL, CECI_LL, CECI_HL
    Image IntensityCorrection
    Number sx,sy,sz, c5, c4, c3, c2, c1, c0,l

```

```

String NameO_LL, NameO_HL
GetTwoLabeledImagesWithPrompt("Choose Spectrum Images", "Select Sl's", "Low-
Loss", O_LL, "High-Loss", O_HL)
CECI_LL := O_LL.ImageClone()
CECI_HL := O_HL.ImageClone()
//Retrieve polynomial coefficients calculated in previous section
GetPersistentNumberNote("EELSDispersion:NonLinFit:a0",c0)
GetPersistentNumberNote("EELSDispersion:NonLinFit:a1",c1)
GetPersistentNumberNote("EELSDispersion:NonLinFit:a2",c2)
GetPersistentNumberNote("EELSDispersion:NonLinFit:a3",c3)
GetPersistentNumberNote("EELSDispersion:NonLinFit:a4",c4)
GetPersistentNumberNote("EELSDispersion:NonLinFit:a5",c5)
result("Fit Coeffs c0: "+Format(c0,"% .10e")+ " c1: "+Format(c1,"% .10e")+ " c2:
"+Format(c2,"% .10e")+ " c3: "+Format(c3,"% .10e")+ " c4: "+Format(c4,"% .10e")+ " c5:
"+Format(c5,"% .10e")+ "\n\n")
//Get original names of spectrum images
NameO_LL=GetName(O_LL)
NameO_HL=GetName(O_HL)
//Get dimensions of spectrum images
O_LL.Get3DSize(sx,sy,sz)
//rotate spectrum images to put dispersive direction in slice direction
R_LL = Slice3(O_LL ,sx-1, 0, 0, 2,sz, 1, 1,sy, 1, 0,sx,-1)
R_HL = Slice3(O_HL ,sx-1, 0, 0, 2,sz, 1, 1,sy, 1, 0,sx,-1)
RCE_LL = R_LL.ImageClone()
RCECI_LL = R_LL.ImageClone()
RCE_HL = R_HL.ImageClone()
RCECI_HL = R_HL.ImageClone()
//Make the intensity correction
IntensityCorrection = Slice3(R_LL,0,0,0,sz,1,1,sy,1,2,1,1)
//Calculate intensity correction factor according to Jacobian conversion of coordinate
systems
IntensityCorrection=5*c5*icol**4+4*c4*icol**3+3*c3*icol**2+2*c2*icol+c1+1 //(the +1 at the
end is effectively bookkeeping
//apply the polynomial interpolation and subsequent intensity correction
I=0
While (I<sx)
{
//Correct the energy
Slice3(RCE_LL,0,0,I,0,sz,1,1,sy,1,2,1,1)=WARP(Slice3(R_LL,0,0,I,0,sz,1,1,sy,1,2,1,1),c5*i
col**5+c4*icol**4+c3*icol**3+c2*icol**2+c1*icol+c0+icol,irow)
Slice3(RCE_HL,0,0,I,0,sz,1,1,sy,1,2,1,1)=WARP(Slice3(R_HL,0,0,I,0,sz,1,1,sy,1,2,1,1),c5*i
col**5+c4*icol**4+c3*icol**3+c2*icol**2+c1*icol+c0+icol,irow)
//Correct the Intensity
Slice3(RCECI_LL,0,0,I,0,sz,1,1,sy,1,2,1,1)=Slice3(RCE_LL,0,0,I,0,sz,1,1,sy,1,2,1,1)*Intens
ityCorrection
Slice3(RCECI_HL,0,0,I,0,sz,1,1,sy,1,2,1,1)=Slice3(RCE_HL,0,0,I,0,sz,1,1,sy,1,2,1,1)*Inten
sityCorrection
I++
}
//undo the earlier rotation
CECI_LL = Slice3(RCECI_LL , 0, 0,sx-1, 2,sx,-1, 1,sy, 1, 0,sz, 1)
CECI_HL = Slice3(RCECI_HL , 0, 0,sx-1, 2,sx,-1, 1,sy, 1, 0,sz, 1)
//set image name
SetName(CECI_LL, NameO_LL+" (CorrE)(CorrI)")
SetName(CECI_HL, NameO_HL+" (CorrE)(CorrI)")
//display corrected images
ShowImage(CECI_LL)
ShowImage(CECI_HL)
}
void Main()
{
if(OKCancelDialog("Process experimental dispersion spectrum images?")) ZLPGauss()

```

```
        if(OKCancelDialog("Proceed with 5th order polynomial fit to non-linearities?")) PolyReg()  
        if(OKCancelDialog("Use fitted nonlinearities to correct a pair of Dual-EELS SI's?"))  
Implement()  
}  
Main()
```

Appendix B

Least squares fitting for differential cross-sections with tags 2

```
//SCRIPT TO EXTRACT THE DIFFERENTIAL CROSS-SECTION OF AN EDGE FROM A SPECTRUM IMAGE
// CONTAINING A BACKGROUND SUBTRACTED EDGE
//Tags added to output spectrum to give processing conditions
//The gradient is differential cross-section is in BARNS/eV.
//The vertical axis and intercept is the signal per eV normalised by lo
//The horizontal scale is atoms/barn
//***** INPUT THE DATA *****
Image EdgeSI, TLamda, lo, SpliceRatio, EdgeSI2, TLamda2, lo2, SpliceRatio2
number TimeHigh, TimeLow
GetFourImagesWithPrompt("Enter Edge SI,t/lamda map,lo map,Splice ratio map","Enter
Data",EdgeSI,TLamda,lo, SpliceRatio)
//Put the file names in strings to put in the tags below
string EdgeSIname, TLamdaName, loName,SpliceRatioName
EdgeSIname=GetName(EdgeSI)
TLamdaName=GetName(TLamda)
loName=GetName(lo)
SpliceRatioName=GetName(SpliceRatio)
//Result(EdgeSIname+"\n")
//Result(TLamdaName+"\n")
//Result(loName+"\n")
//Result(SpliceRatioName+"\n")
//Put the input images into duplicates
EdgeSI2=EdgeSI.imageclone()
TLamda2=TLamda.imageclone()
lo2=lo.imageclone()
SpliceRatio2=SpliceRatio.imageclone()
//Get the acquisition times
GetNumber("Enter the High Loss Acquisition Time",49700,TimeHigh)
GetNumber("Enter the Low Loss Acquisition Time",298.2,TimeLow)
//***** CHECK THE DATA IS SELF CONSISTENT *****
// Get image sizes and test for compatibility
Number sxEdge, syEdge, szEdge, sxTL, syTL, sxlo, sylo, sxSplice, sySplice
EdgeSI2.get3dsizes(sxEdge,syEdge,szEdge)
TLamda2.get2dsizes(sxTL,syTL)
lo2.get2dsizes(sxlo,sylo)
SpliceRatio2.get2dsizes(sxSplice,sySplice)
//Result(sxEdge+" "+syEdge+" "+szEdge+" "+sxTL+" "+syTL+" "+sxlo+" "+sylo+" "+sxSplice+" "+
sySplice+" \n")
If (sxTL != SxEdge) OKCancelDialog("Dimensions of t/lamda map wrong CANCEL")
If (sxlo != SxEdge) OKCancelDialog("Dimensions of lo map wrong CANCEL")
If (sxSplice != SxEdge) OKCancelDialog("Dimensions of Splice Map map wrong CANCEL")
If (syTL != SyEdge) OKCancelDialog("Dimensions of t/lamda map wrong CANCEL")
If (sylo != SyEdge) OKCancelDialog("Dimensions of lo map wrong CANCEL")
If (sySplice != SyEdge) OKCancelDialog("Dimensions of Splice map wrong CANCEL")
If (TimeHigh/TimeLow<1) OKCancelDialog("Ratio of Core and Low Loss Acquisition Time <1. Expect
>1.")
//***** OPTION TO CHANGE SPLICE RATIO TO TIME RATIO *****
// Ask for choice
number choice
choice = 0
getnumber("To change from Splice Ratio to Time Ratio enter 1",0,choice)
//result(choice+" \n")
//set string for tags if splice ratio is used
string RatioChoice
RatioChoice = "Splice"
```

```

// Change lo if "Choice" is 1
If (Choice==1) lo2 = lo2/SplICERatio*TimeHigh/TimeLow
//showimage(lo2)
//Change string for tags if time ratio is used
If (Choice==1) RatioChoice = "Time"
//Normalise the EdgeSI by dividing by lo
Image loverlo
loverlo=EdgeSI.imageclone()
loverlo /=lo2[icol,irow]
//Convert to loverloPerEV
number dE
dE=EdgeSI.imagegetdimensionscale(2)
//Result(dE+" \n")
loverlo=loverlo/dE
//ShowImage(loverlo)
//*****
//Enter Lamda (nm) and Number of atoms per nanometre cubed
//*****
Number Lamda, AtomsPerVol,BarnConversion
getnumber("Inelastic Lamda (nm)",122,Lamda)
getnumber("Atoms per cubic nm",52.47,AtomsPerVol)
TLamda2=TLamda2*Lamda*AtomsPerVol
// Convert to Barns^-1 by dividing by 10^10
BarnConversion=10000000000.
TLamda2=TLamda2/BarnConversion
//ShowImage(TLamda2)
//***** DO THE LEAST SQUARES FITTING *****
number N,M //running variables for loops in least square fit
number sx,sy,sz // data size for least square fit
number meanx,bytes,meany,type //numbers for least squares fit
//set the array sizes to match the data
sx=sxEdge
sy=syEdge
sz=szEdge
//Set the number of bytes to be used for the calculation
Getnumber ("Enter the number of bytes",8,bytes)
//Put the variables into variables used in the routine below
//First get the x-arrays
image xArray2D := ReallImage("x-array",bytes,sx,sy,sz)
image xArray3D := ReallImage("x-array3D",bytes,sx,sy,sz)
// take T/lamada as the x-array
xarray2D += TLamda2[icol,irow]
//Copy xArray2D into each slice of xArray3D
xarray3D +=xarray2D[icol,irow]
//Showimage(xarray3D)
//Then get the yarray
image yArray3DplusNoise := ReallImage("y-array with noise",bytes,sx,sy,sz)
//Set the yArray to be the signal intensity per eV normalised by lo
yArray3DplusNoise += loverlo[icol,irow,iplane]
//ShowImage(yArray3DplusNoise)
//The equations for the least squares fit are taken from
//Least Squares Fitting -- from Wolfram MathWorld on the web
//calculate the mean of the x-array2D
meanx=average(xarray2D)
//result(meanx+"\n")
//Calculate the xArray3D minus the mean
image xMinusMeanxArray3D := ReallImage("X minus meanX 3D",bytes,sx,sy,sz)
xMinusMeanxarray3D=xarray3D-meanx
//ShowImage(xMinusMeanxarray3D)
//Maybe it's easier to put the y means in a 3d array and the the subtraction is straightforward
using the subtract two 3D array script
//Calculate the mean of each slice of the y-array 3d and put in a 3D array

```

```

image yMeanArray3D := ReallImage("yMeanArray3D",bytes,sx,sy,sz)
image yMinusMeany3D := ReallImage("Y minus meanY 3D",bytes,sx,sy,sz)
N=0
While(N<sz)
  {
    // The axes of the output dataset are in the order x,y,z
    // slice3 has arguments
    // startx, starty, startz, x-axis, number-x, step-x,
    // y-axis, number-y, step-y, z-axis, number-z, step-z)
    yMeanArray3D.slice3(0,0,N,0,sx,1,1,sy,1,2,1,1)=yArray3DplusNoise.slice3(0,0,N,0,sx,1,1,
sy,1,2,1,1).average()
    N=N+1
  }
//ShowImage(yMeanArray3D)
// subtract the mean y from the y array
yMinusMeany3D=yArray3DplusNoise-yMeanArray3D
//ShowImage(yMeanArray3D)
//ShowImage(yMinusMeany3D)
//Form the the arrays (x-mean)^2 (y-meany)^2 and (x-meanx)*(y-meany)
image xxProduct := ReallImage("xx product",bytes,sx,sy,sz)
image yyProduct := ReallImage("yy product",bytes,sx,sy,sz)
image xyProduct := ReallImage("xy product",bytes,sx,sy,sz)
xxproduct=xMinusMeanxarray3D*xMinusMeanxarray3D
yyproduct=yMinusMeany3D*yMinusMeany3D
xyproduct=xMinusMeanxarray3D*yMinusMeany3D
//ShowImage(xxProduct)
//ShowImage(yyProduct)
//ShowImage(xyProduct)
//Form the sums SSxx, SSyy SSxy and put them into "FitResults" in cols 1,2,3 of row 1 (as used in a
spreadsheet)
// DM would have it as 0,1,2, in row 0
number sxresults, syresults
sxresults=4
syresults=3
image FitResults := ReallImage("Fit Results",bytes,sxresults,syresults,sz)
FitResults[0,0,iplane] += xxProduct
FitResults[1,0,iplane] += yyProduct
FitResults[2,0,iplane] += xyProduct
//Evlaute the fit results plane by plane
N=0
While (N<sz)
  {
    //Form s and put it into row 1 column 4
    FitResults[3,0,N]=sqrt((FitResults[1,0,N]-
FitResults[2,0,N]*FitResults[2,0,N]/FitResults[0,0,N])/(sx*sy-2))
    //Put xmean and ymean into row 2 cols 1,2 of FitResults
    FitResults[0,1,N]=Meanx
    FitResults[1,1,N]=yMeanArray3D[0,0,N]
    //Calculate, gradient, gradient error, interecept, intercept error
    //Put in row 3 columns1,2,3,4 of fit results
    FitResults[0,2,N]= FitResults[2,0,N]/FitResults[0,0,N]
    FitResults[1,2,N]= FitResults[3,0,N]/sqrt(FitResults[0,0,N])
    FitResults[2,2,N]= FitResults[1,1,N]-FitResults[0,2,N]*FitResults[0,1,N]
    FitResults[3,2,N]=
FitResults[3,0,N]*sqrt((1/sx/sy)+(FitResults[0,1,N]*FitResults[0,1,N]/FitResults[0,0,N]))
    N=N+1
  }
//Set the display type to spreadsheet for FitResults
//To convert the display type of an image use
//setDisplayType(img,type)
//img is the image of interest
//n is the display type required

```

```

//By trial and error
// type=1 raster
// type=2 surface plot
// type=3 error - not sure
// type=4 Line plot
// type=5 Spreadsheet
// type=6 error not sure
// type=7 spreadsheet
type=5
setdisplaytype(FitResults,type)
ShowImage(FitResults)
//*****
// Put the data into 4 byte form so that it can be recognised
//as a Spectrum Image and Convert to EELS
//*****
//results currently in nm squared not Barns
//*****
//Put the coefficient and error data into 4 byte form
number sxResults4byte, syResult4byte, BytesResults4Byte
BytesResults4Byte=4
sxResults4byte=4
syResult4byte=1
image FitResults4byte := ReallImage("Fit results 4
byte",BytesResults4Byte,sxResults4byte,syResult4byte,sz)
FitResults4byte=FitResults[icol,2,iplane]
//Calibrate energy scale
FitResults4byte.imagesetdimensionyscale(2,EdgeSI.imagegetdimensionyscale(2))
FitResults4byte.imagesetdimensionorigin(2,EdgeSI.imagegetdimensionorigin(2))
FitResults4byte.imagesetdimensionunitstring(2,EdgeSI.imagegetdimensionunitstring(2))
ShowImage(FitResults4Byte)
//Change to EELS data.
//"FitResults$Byte is now the front image.
//Change to EELS using the menu command.
//There ought to be a script command to do this directly but I can't find it.
//However, it's clear what tags are added when the swap to EELS is made
//Thus writing in the extra tags might do it.
ChooseMenuItem("Spectrum","Convert Data To", "EELS")
//Set the display type to spreadsheet for FitResults4Byte
//To convert the display type of an image use
//setDisplayType(img,type)
//img is the image of interest
//n is the display type required
//By trial and error
// type=1 raster
// type=2 surface plot
// type=3 error - not sure
// type=4 Line plot
// type=5 Spreadsheet
// type=6 error not sure
// type=7 spreadsheet
type=1
setdisplaytype(FitResults4Byte,type)

//Add tags to FitResults$Byte under dSigma/dE conditions
//High loss time in arb units
FitResults4Byte.SetNumberNote("dSigma/dE conditions:High Loss Aquisition Time", TimeHigh)
//Low loss time in arb units
FitResults4Byte.SetNumberNote("dSigma/dE conditions:Low Loss Aquisition Time", TimeLow)
//Splice or Time Ratio
FitResults4Byte.SetStringNote("dSigma/dE conditions:Time or Splice Ratio", RatioChoice)
//In elastic mean free path
FitResults4Byte.SetNumberNote("dSigma/dE conditions:Mean Free Path (nm)", Lamda)

```

```

//Atoms/vol
FitResults4Byte.SetNumberNote("dSigma/dE conditions:Atoms per cubic nm", AtomsPerVol)
//Bytes for processing
FitResults4Byte.SetNumberNote("dSigma/dE conditions:Bytes for fitting process", Bytes)
//EdgeSI file name
FitResults4Byte.SetStringNote("dSigma/dE conditions:EdgeSI file name", EdgeSIName)
//TLamda file name
FitResults4Byte.SetStringNote("dSigma/dE conditions:T/Lamda Map file name", TLamdaName)
//Io file name
FitResults4Byte.SetStringNote("dSigma/dE conditions:Io Map file name", IoName)
//EdgeSI file name
FitResults4Byte.SetStringNote("dSigma/dE conditions:Splice Ratio Map file name",
SpliceRatioName)
//*****
//put the results in a form suitable for transfer to EXCEL for plotting
//*****
//the results in a given plane are in columns of length sx*sy.
//The first column contains the x-values
//The second column contains the y values
//The third column contains the fity values
//The fourth column contained the deviatons
image EXCELResults := ReallImage("EXCEL Results",bytes,4,sx*sy,sz)
//Define TEMP images to do the transfers.
//To do this assign the relevant section of the array to the TEMP function
//by using ":-"
number sxTemp
sxTemp=1
Image TEMPx := ReallImage("",bytes,sxTemp,sy,sz)
Image TEMPy := ReallImage("",bytes,sxTemp,sy,sz)
Image TEMPfit := ReallImage("",bytes,sxTemp,sy,sz)
Image TEMPdev := ReallImage("",bytes,sxTemp,sy,sz)
//initialise loop parameters
N=0
M=0
//Create a loop over the x-direction
//NB icol addresses X irow addresses Y
While (N<sx)
  {
    //Select the current position down the array
    TEMPx:=EXCELResults.slice3(0,M,0, 0,1,1, 1,sy,1, 2,sz,1)
    // Transfer the current column in
    TEMPx=Xarray3D[N,irow,iplane]
    //Select the current position down the array
    TEMPy:=EXCELResults.slice3(1,M,0, 0,1,1, 1,sy,1, 2,sz,1)
    //Transfer the current column in
    TEMPy=yArray3DplusNoise[N,irow,iplane]
    //Select the current position down the array
    TEMPfit:=EXCELResults.slice3(2,M,0, 0,1,1, 1,sy,1, 2,sz,1)
    // Transfer the current column in
    TEMPfit=Xarray3D[N,irow,iplane]
    // multiply by the gradiesnt
    TEMPfit *=FitResults[0,2,iplane]
    //add the intercept
    TEMPfit +=FitResults[2,2,iplane]
    //Select the current position down the array
    TEMPdev:=EXCELResults.slice3(3,M,0, 0,1,1, 1,sy,1, 2,sz,1)
    // Subtract the fit from the y data
    TEMPdev=TEMPy-TEMPfit
    N=N+1
    M=M+sy
  }
//Set the display type to spreadsheet for EXCELresults

```

```
//To convert the display type of an image use
//setDisplayType(img,type)
//img is the image of interest
//n is the display type required
//By trial and error
// type=1 raster
// type=2 surface plot
// type=3 error - not sure
// type=4 Line plot
// type=5 Spreadsheet
// type=6 error not sure
// type=7 spreadsheet
type=5
setDisplayType(EXCELresults,type)
ShowImage(EXCELresults)
```

Appendix C

Least squares fitting for differential cross-sections fourier ratio

```
//SCRIPT TO EXTRACT THE DIFFERENTIAL CROSS-SECTION OF A BACKGROUND SUBTRACTED
//FOURIER RATIO DECONVOLUTED EDGE.
```

```
//VERSION 1.1
```

```
// Convert the cross-section plot to EELS
```

```
//Set up for VC83
```

```
//Tags added to output spectrum to give processing conditions
```

```
//The gradient is differential cross-section is in BARNS/eV.
```

```
//The vertical axis and intercept is the signal per eV normalised by lo
```

```
//The horizontal scale is atoms/barn
```

```
//An OK dialog to give information on what's required
```

```
OKdialog("This script is for use with a background subtracted, Fourier RATIO deconvolved high loss
SI and the t/lamda and lo maps from the corresponding low loss SI.\n\nThe main purpose of this
script is to give a differential cross-section in barns/eV plus its error.\n\nIt also provides
information on the quality of the fits. \n\nThe inputs are:\n\n    An SI with the Fourier RATIO
deconvolved edge SI; \n\n    A t/lamda map from the Fourier LOG deconvolved low loss SI;\n\n
An lo map from the Fourier LOG deconvolved low loss SI;\n\n    A set of parameters.\n\nAn option
to save the files is provided")
```

```
//*****
//                               INPUT THE DATA
//*****
```

```
Image EdgeSI, TLamda, lo, EdgeSI2, TLamda2, lo2
```

```
number TimeHigh, TimeLow
```

```
GetThreeLabeledImagesWithPrompt("Enter Bkg Sub FR decon Edge SI, t/lamda map, lo map", "Enter
Data", "Edge SI", EdgeSI, "t/lamda map", TLamda, "lo map", lo)
```

```
//Put the file names in strings to put in the tags below
```

```
string EdgeSIname, TLamdaName, loName
```

```
EdgeSIname=GetName(EdgeSI)
```

```
TLamdaName=GetName(TLamda)
```

```
loName=GetName(lo)
```

```
//Result(EdgeSIname+"\n")
```

```
//Result(TLamdaName+"\n")
```

```
//Result(loName+"\n")
```

```
//Put the input images into duplicates
```

```
EdgeSI2=EdgeSI.imageclone()
```

```
TLamda2=TLamda.imageclone()
```

```
lo2=lo.imageclone()
```

```
//Get the identifier to insert in the file names
```

```
String FileIdentifier
```

```
GetString("Enter the identifier for the file name", "VC83 SB001 ", FileIdentifier)
```

```
//Get the acquisition times
```

```
GetNumber("Enter the High Loss Acquisition Time", 19512.2, TimeHigh)
```

```
GetNumber("Enter the Low Loss Acquisition Time",487.805,TimeLow)
```

```
//*****g*****
//          CHECK THE DATA IS SELF CONSISTENT
//*****g*****

// Get image sizes and test for compatiblity
Number sxEdge, syEdge, szEdge, sxTL, syTL, sxlo, sylo
EdgeSI2.get3dsizes(sxEdge,syEdge,szEdge)
TLamda2.get2dsizes(sxTL,syTL)
lo2.get2dsizes(sxlo,sylo)
//Result(sxEdge+" "+ syEdge+" "+ szEdge+" "+ sxTL+" "+ syTL+" "+ sxlo+" "+ sylo+" \n")

If (sxTL != SxEdge) OKCancelDialog("Dimensions of t/lamda map wrong CANCEL")
If (sxlo != SxEdge) OKCancelDialog("Dimensions of lo map wrong CANCEL")
If (syTL != SyEdge) OKCancelDialog("Dimensions of t/lamda map wrong CANCEL")
If (sylo != SyEdge) OKCancelDialog("Dimensions of lo map wrong CANCEL")
If (TimeHigh/TimeLow<1) OKCancelDialog("Ratio of Core and Low Loss Acquisition Time <1. Expect
>1.")

//*****
//          Divide the Edge SI by the time ratio and normalise it with lo
//*****

//set string for tags if splice ratio is used
string RatioChoice
RatioChoice = "Time"

//Clone the Edge SI
Image loverlo
loverlo=EdgeSI.imageclone()

//Divide the EdgeSI by the time ratio
//This step is needed here but not when using a spliced SI, where it's already done
loverlo=loverlo*TimeLow/TimeHigh

//Normalise the EdgeSI by dividing by lo
loverlo /=lo2[icol,irow]
//Convert to loverloPerEV
number dE
dE=EdgeSI.imagegetdimensionscale(2)
//Result(dE+" \n")
loverlo=loverlo/dE
//ShowImage(loverlo)

//*****
//Enter Lamda (nm) and Number of atoms per nanometre cubed
//*****

Number Lamda, AtomsPerVol,BarnConversion
getnumber("Inelastic Lamda (nm)",99.9,Lamda)
getnumber("Atoms per cubic nm",55.29,AtomsPerVol)
TLamda2=TLamda2*Lamda*AtomsPerVol
// Convert to Barns^-1 by dividing by 10^10
BarnConversion=10000000000.
TLamda2=TLamda2/BarnConversion
//ShowImage(TLamda2)

//*****
//          DO THE LEAST SQUARES FITTING
//*****
```

```

number N,M //running variables for loops in least square fit
number sx,sy,sz // data size for least square fit
number meanx,bytes,meany,type //numbers for least squares fit

//set the array sizes to match the data
sx=sxEdge
sy=syEdge
sz=szEdge

//Set the number of bytes to be used for the calculation
Getnumber ("Enter the number of bytes",8,bytes)
//Put the variables into variables used in the routine below

//First get the x-arrays
image xArray2D := ReallImage("x-array",bytes,sx,sy,sz)
image xArray3D := ReallImage("x-array3D",bytes,sx,sy,sz)
// take T/lamada as the x-array
xarray2D += Tlamda2[icol,irow]
//Copy xArray2D into each slice of xArray3D
xarray3D +=xarray2D[icol,irow]
//Showimage(xarray3D)

//Then get the yarray
image yArray3DplusNoise := ReallImage("y-array with noise",bytes,sx,sy,sz)
//Set the yArray to be the signal intensity per eV normalised by lo
yArray3DplusNoise += loverlo[icol,irow,iplane]
//ShowImage(yArray3DplusNoise)

//The equations for the least squares fit are taken from
//Least Squares Fitting -- from Wolfram MathWorld on the web

//calculate the mean of the x-array2D
meanx=average(xarray2D)
//result(meanx+"\n")

//Calculate the xArray3D minus the mean
image xMinusMeanxArray3D := ReallImage("X minus meanX 3D",bytes,sx,sy,sz)
xMinusMeanxarray3D=xarray3D-meanx
//ShowImage(xMinusMeanxarray3D)

//Maybe it's easier to put the y means in a 3d array and the the subtraction is straightforward
using the subtract two 3D array script

//Calculate the mean of each slice of the y-array 3d and put in a 3D array
image yMeanArray3D := ReallImage("yMeanArray3D",bytes,sx,sy,sz)
image yMinusMeany3D := ReallImage("Y minus meanY 3D",bytes,sx,sy,sz)
N=0
While(N<sz)
  {
    // The axes of the output dataset are in the order x,y,z
    // slice3 has arguments
    // startx, starty, startz, x-axis, number-x, step-x,
    // y-axis, number-y, step-y, z-axis, number-z, step-z)
    yMeanArray3D.slice3(0,0,N,0,sx,1,1,sy,1,2,1,1)=yArray3DplusNoise.slice3(0,0,N,0,sx,1,1,
sy,1,2,1,1).average()
    N=N+1
  }
//ShowImage(yMeanArray3D)

// subtract the mean y from the y array
yMinusMeany3D=yArray3DplusNoise-yMeanArray3D
//ShowImage(yMeanArray3D)

```

```

//ShowImage(yMinusMeany3D)

//Form the the arrays (x-mean)^2 (y-meany)^2 and (x-meanx)*(y-meany)
image xxProduct := ReallImage("xx product",bytes,sx,sy,sz)
image yyProduct := ReallImage("yy product",bytes,sx,sy,sz)
image xyProduct := ReallImage("xy product",bytes,sx,sy,sz)
xxproduct=xMinusMeanxarray3D*xMinusMeanxarray3D
yyproduct=yMinusMeany3D*yMinusMeany3D
xyproduct=xMinusMeanxarray3D*yMinusMeany3D
//ShowImage(xxProduct)
//ShowImage(yyProduct)
//ShowImage(xyProduct)

//Form the sums SSxx, SSyy SSxy and put them into "FitResults" in cols 1,2,3 of row 1 (as used in a
spreadsheet)
// DM would have it as 0,1,2, in row 0
number sxresults, syresults
sxresults=4
syresults=3
image FitResults := ReallImage("Fit Results Expt lamda",bytes,sxresults,syresults,sz)
FitResults[0,0,iplane] += xxProduct
FitResults[1,0,iplane] += yyProduct
FitResults[2,0,iplane] += xyProduct

//Evlaute the fit results plane by plane
N=0
While (N<sz)
{
//Form s and put it into row 1 column 4
FitResults[3,0,N]=sqrt((FitResults[1,0,N]-
FitResults[2,0,N]*FitResults[2,0,N]/FitResults[0,0,N])/(sx*sy-2))
//Put xmean and ymean into row 2 cols 1,2 of FitResults
FitResults[0,1,N]=Meanx
FitResults[1,1,N]=yMeanArray3D[0,0,N]
//Calculate, gradient, gradient error, interecept, intercept error
//Put in row 3 columns1,2,3,4 of fit results
FitResults[0,2,N]= FitResults[2,0,N]/FitResults[0,0,N]
FitResults[1,2,N]= FitResults[3,0,N]/sqrt(FitResults[0,0,N])
FitResults[2,2,N]= FitResults[1,1,N]-FitResults[0,2,N]*FitResults[0,1,N]
FitResults[3,2,N]=
FitResults[3,0,N]*sqrt((1/sx/sy)+(FitResults[0,1,N]*FitResults[0,1,N]/FitResults[0,0,N]))
N=N+1
}

//name FitResults to include file identifier
FitResults.SetName(FileIdentifier+ " Fit Results Exp Lamda")

//Set the display type to spreadsheet for FitResults
//To convert the display type of an image use
//setDisplayType(img,type)
//img is the image of interest
//n is the display type required
// type= -1 Best
// type=1 raster
// type=2 surface plot
// type=3 RGB
// type=4 Line plot
// type=5 Spreadsheet
type=5
setDisplaytype(FitResults,type)
ShowImage(FitResults)

```

```

//Add tags to FitResults under "dSigma/dE conditions"
//High loss time in arb units
FitResults.SetNumberNote("dSigma/dE conditions:High Loss Aquisition Time", TimeHigh)
//Low loss time in arb units
FitResults.SetNumberNote("dSigma/dE conditions:Low Loss Aquisition Time", TimeLow)
//Splice or Time Ratio
FitResults.SetStringNote("dSigma/dE conditions:Time or Splice Ratio", RatioChoice)
//ln elastic mean free path
FitResults.SetNumberNote("dSigma/dE conditions:Mean Free Path (nm)", Lamda)
//Atoms/vol
FitResults.SetNumberNote("dSigma/dE conditions:Atoms per cubic nm", AtomsPerVol)
//Bytes for processing
FitResults.SetNumberNote("dSigma/dE conditions:Bytes for fitting process", Bytes)
//EdgeSI file name
FitResults.SetStringNote("dSigma/dE conditions:EdgeSI file name", EdgeSIName)
//TLamda file name
FitResults.SetStringNote("dSigma/dE conditions:T/Lamda Map file name", TLamdaName)
//lo file name
FitResults.SetStringNote("dSigma/dE conditions:lo Map file name", loName)

//*****
// Put the data into 4 byte form so that it can be recognised
//as a Spectrum Image and Convert to EELS
//*****
//results currently in nm squared not Barns
//*****

//Put the coefficient and error data into 4 byte form
number sxResults4byte, syResult4byte, BytesResults4Byte
BytesResults4Byte=4
sxResults4byte=4
syResult4byte=1
image      FitResults4byte      :=      ReallImage("Fit      results      4      byte      expt
lamda", BytesResults4Byte, sxResults4byte, syResult4byte, sz)
FitResults4byte=FitResults[icol,2,iplane]

//Calibrate energy scale and give the dimensions of the intensity axis
FitResults4byte.imagesetdimensionyscale(2,EdgeSI.imagegetdimensionyscale(2))
FitResults4byte.imagesetdimensionorigin(2,EdgeSI.imagegetdimensionorigin(2))
FitResults4byte.imagesetdimensionunitstring(2,EdgeSI.imagegetdimensionunitstring(2))
ImageSetIntensityUnitString(FitResults4Byte, "dSigma/dE (barns/eV)")

//name FitResults4Byte to include file identifier
FitResults4byte.SetName(FileIdentifier+ " Fit Results 4 Bytes Expt Lamda")

ShowImage(FitResults4Byte)

//Change to EELS data.
setstringnote(FitResults4Byte, "Meta Data:Format", "Spectrum image");
setstringnote(FitResults4Byte, "Meta Data:Signal", "EELS");
//Bernhard says some DM versions don't recognise the change without being forced to.
// He uses a change of display type. This might work.
//imagedisplay disp= FitResults4Byte.imagegetimagedisplay(0)
//disp.ImageDisplayChangeDisplayType(5)
//disp.ImageDisplayChangeDisplayType(1)

//Set the display type to spreadsheet for FitResults4Byte
//To convert the display type of an image use
//SetDisplayType(img,type)
//img is the image of interest
//n is the display type required
// type= -1 Best

```

```

// type=1 raster
// type=2 surface plot
// type=3 RGB
// type=4 Line plot
// type=5 Spreadsheet
type=1
setdisplaytype(FitResults4Byte,type)

//Add tags to FitResults4Byte under "dSigma/dE conditions"
//High loss time in arb units
FitResults4Byte.SetNumberNote("dSigma/dE conditions:High Loss Aquisition Time", TimeHigh)
//Low loss time in arb units
FitResults4Byte.SetNumberNote("dSigma/dE conditions:Low Loss Aquisition Time", TimeLow)
//Splice or Time Ratio
FitResults4Byte.SetStringNote("dSigma/dE conditions:Time or Splice Ratio", RatioChoice)
//ln elastic mean free path
FitResults4Byte.SetNumberNote("dSigma/dE conditions:Mean Free Path (nm)", Lamda)
//Atoms/vol
FitResults4Byte.SetNumberNote("dSigma/dE conditions:Atoms per cubic nm", AtomsPerVol)
//Bytes for processing
FitResults4Byte.SetNumberNote("dSigma/dE conditions:Bytes for fitting process", Bytes)
//EdgeSI file name
FitResults4Byte.SetStringNote("dSigma/dE conditions:EdgeSI file name", EdgeSIName)
//TLamda file name
FitResults4Byte.SetStringNote("dSigma/dE conditions:T/Lamda Map file name", TLamdaName)
//lo file name
FitResults4Byte.SetStringNote("dSigma/dE conditions:lo Map file name", loName)

//*****
//put the results in a form suitable for transfer to EXCEL for plotting
//*****
//the results in a given plane are in columns of length sx*sy.
//The first column contains the x-values
//The second column contains the y values
//The third column contains the fity values
//The fourth column contained the deviatitons
image EXCELResults := ReallImage("EXCEL Results Expt Lamda",bytes,4,sx*sy,sz)

//Define TEMP images to do the transfers.
//To do this assign the relevant section of the array to the TEMP function
//by using ":"=
number sxTemp
sxTemp=1
Image TEMPx := ReallImage("",bytes,sxTemp,sy,sz)
Image TEMPy := ReallImage("",bytes,sxTemp,sy,sz)
Image TEMPfit := ReallImage("",bytes,sxTemp,sy,sz)
Image TEMPdev := ReallImage("",bytes,sxTemp,sy,sz)

//initialise loop parameters
N=0
M=0

//Create a loop over the x-direction
//NB icol addresses X   irow addresses Y
While (N<sx)
{
//Select the current position down the array
TEMPx:=EXCELResults.slice3(0,M,0, 0,1,1, 1,sy,1, 2,sz,1)
// Transfer the current column in
TEMPx=Xarray3D[N,irow,iplane]
//Select the current position down the array
TEMPy:=EXCELResults.slice3(1,M,0, 0,1,1, 1,sy,1, 2,sz,1)

```

```

//Transfer the current column in
TEMPy=yArray3DplusNoise[N,irow,iplane]
//Select the current position down the array
TEMPfit:=EXCELResults.slice3(2,M,0, 0,1,1, 1,sy,1, 2,sz,1)
// Transfer the current column in
TEMPfit=Xarray3D[N,irow,iplane]
// multiply by the gradiesnt
TEMPfit *=FitResults[0,2,iplane]
//add the intercept
TEMPfit +=FitResults[2,2,iplane]
//Select the current position down the array
TEMPdev:=EXCELResults.slice3(3,M,0, 0,1,1, 1,sy,1, 2,sz,1)
// Subtract the fit from the y data
TEMPdev=TEMPy-TEMPfit
N=N+1
M=M+sy
}

//Set the display type to spreadsheet for EXCELresults
//To convert the display type of an image use
//setDisplayType(img,type)
//img is the image of interest
//n is the display type required
// type= -1 Best
// type=1 raster
// type=2 surface plot
// type=3 RGB
// type=4 Line plot
// type=5 Spreadsheet
type=5
setDisplaytype(EXCELresults,type)

//name EXCELResults to include file identifier
EXCELresults.SetName(FileIdentifier+ " EXCEL Results Expt Lamda")

//Add tags to EXCELresults under dSigma/dE conditions
//High loss time in arb units
EXCELresults.SetNumberNote("dSigma/dE conditions:High Loss Aquisition Time", TimeHigh)
//Low loss time in arb units
EXCELresults.SetNumberNote("dSigma/dE conditions:Low Loss Aquisition Time", TimeLow)
//Splice or Time Ratio
EXCELresults.SetStringNote("dSigma/dE conditions:Time or Splice Ratio", RatioChoice)
//ln elastic mean free path
EXCELresults.SetNumberNote("dSigma/dE conditions:Mean Free Path (nm)", Lamda)
//Atoms/vol
EXCELresults.SetNumberNote("dSigma/dE conditions:Atoms per cubic nm", AtomsPerVol)
//Bytes for processing
EXCELresults.SetNumberNote("dSigma/dE conditions:Bytes for fitting process", Bytes)
//EdgeSI file name
EXCELresults.SetStringNote("dSigma/dE conditions:EdgeSI file name", EdgeSIName)
//TLamda file name
EXCELresults.SetStringNote("dSigma/dE conditions:T/Lamda Map file name", TLamdaName)
//lo file name
EXCELresults.SetStringNote("dSigma/dE conditions:lo Map file name", loName)

ShowImage(EXCELresults)

//*****
//
//          CREATE REQUIRED LABELLED LINEPLOTS
//*****

```

```

//*****
//                               First the cross-section.
//*****

//Set up the 1D dataset
image Xsection := ReallImage(FileIdentifier + " X-section with Expt Lamda",4,sz)

//Extract the first pixel of FitResults4Byte as the cross-section in a D dataset of size sz x 1 x 1
// The axes of the output dataset are in the order x,y,z
// slice3 has arguments
// startx, starty, startz, x-axis, number-x, step-x,
//y-axis, number-y, step-y, z-axis, number-z, step-z)
Xsection.slice3(0,0,0, 0,sz,1, 1,1,1, 2,1,1)=FitResults4Byte.slice3(0,0,0, 2,sz,1, 0,1,1, 1,1,1)

//Change to EELS data.
setstringnote(Xsection, "Meta Data:Format", "Spectrum");
setstringnote(Xsection, "Meta Data:Signal", "EELS");
//Bernhard says some DM versions don't recognise the change without being forced to.
// He uses a change of display type. This might work.
//imagedisplay disp= FitResults4Byte.imagegetimagedisplay(0)
//disp.ImageDisplayChangeDisplayType(5)
//disp.ImageDisplayChangeDisplayType(1)

//Calibrate energy scale and give units for intensity
Xsection.imagesetdimensionyscale(0,EdgeSI.imagegetdimensionyscale(2))
Xsection.imagesetdimensionorigin(0,EdgeSI.imagegetdimensionorigin(2))
Xsection.imagesetdimensionunitstring(0,EdgeSI.imagegetdimensionunitstring(2))
ImageSetIntensityUnitString(Xsection, "dSigma/dE (barns/eV)")

//Add tags to Xsection under "dSigma/dE conditions"
//High loss time in arb units
Xsection.SetNumberNote("dSigma/dE conditions:High Loss Aquisition Time", TimeHigh)
//Low loss time in arb units
Xsection.SetNumberNote("dSigma/dE conditions:Low Loss Aquisition Time", TimeLow)
//Splice or Time Ratio
Xsection.SetStringNote("dSigma/dE conditions:Time or Splice Ratio", RatioChoice)
//In elastic mean free path
Xsection.SetNumberNote("dSigma/dE conditions:Mean Free Path (nm)", Lamda)
//Atoms/vol
Xsection.SetNumberNote("dSigma/dE conditions:Atoms per cubic nm", AtomsPerVol)
//Bytes for processing
Xsection.SetNumberNote("dSigma/dE conditions:Bytes for fitting process", Bytes)
//EdgeSI file name
Xsection.SetStringNote("dSigma/dE conditions:EdgeSI file name", EdgeSIName)
//TLamda file name
Xsection.SetStringNote("dSigma/dE conditions:T/Lamda Map file name", TLamdaName)
//Io file name
Xsection.SetStringNote("dSigma/dE conditions:Io Map file name", IoName)

ShowImage(Xsection)

//Set the variables for the lineplot labelling

imagedisplay DISP
object SLICEID_0,SLICEID_1

//Add the foreground plot to the final plot
DISP = Xsection.ImageGetImageDisplay(0)
DISP.LinePlotImageDisplaySetDoAutoSurvey( 0, 0 )
SLICEID_0 = DISP.ImageDisplayGetSliceIDByIndex(0)

```

```

//Show the legend
disp.LinePlotImageDisplaySetLegendShown(1)

//Add the original label to the first slice of the final plot
disp.ImageDisplaySetSliceLabelById( sliceID_0, FileIdentifier + " X-section")

//*****
//      Now the percentage error
//*****

//Clone to presrve the tags and calibration
IMAGE PerCentError := Xsection.ImageClone()

//Add the units to the axis
ImageSetIntensityUnitString(PerCentError, "% error")

SetName(PerCentError, FileIdentifier + " X-section PER CENT ERROR with Expt Lamda")

//Extract the spectrum from the second pixel of FitResults4Byte and calculate the percentage
error
PerCentError.slice3(0,0,0, 0,sz,1, 1,1,1, 2,1,1)=FitResults4Byte.slice3(1,0,0, 2,sz,1, 0,1,1,
1,1,1)
PerCentError=PerCentError/Xsection*100

ShowImage(PercentError)

//Add the foreground plot to the final plot
DISP = PerCentError.ImageGetImageDisplay(0)
DISP.LinePlotImageDisplaySetDoAutoSurvey( 0, 0 )
SLICEID_0 = DISP.ImageDisplayGetSliceIDByIndex(0)

//Show the legend
disp.LinePlotImageDisplaySetLegendShown(1)

//Add the original label to the first slice of the final plot
disp.ImageDisplaySetSliceLabelById( sliceID_0, FileIdentifier + " X-section % Error")

//Set vertical scale max to 1.
disp.LinePlotImageDisplaySetContrastLimits(0,1)

//*****
//      Save the files to disc
//*****

// Ask if the files are to be saved. Check if the "disc" icon greys out showing that they have been
saved
//Put a YES/NO dialog box here

number legend = TwoButtonDialog("File the results?\n\nFor the first file choose/create the folder
required\n\nFor the rest just hit return to put them in the same folder\n\nBEWARE the DISC ICON
doesn't grey out even though the file has been save nor does the SAVE option disappear from the
file menu\n\nA dialog box appears at the end to show how many files have been saved.\n\nIf it
DOESNT, check that they have been saved." , "Yes", "No")
If(Legend==0) Exit(0)

//For each image to be saved
//      Check it is valid. Drop out if it's not.
//      Get its current image name
//      Select the destination. Once the first is chosen, the rest will default to it.
//      Save the file with the current image name as the file name offered

```

```

//          For the first it's necessary to choose choose/create the folder into which the file
is saved
//          For subsequent files, this folder is automatically chosen so that only a carriage
returne is needed.

//As a precaution, the number of files saved is counted and shown at the end.

String FileName, FileName0
Number FileCount
FileCount=0

If (!FitResults.ImagelsValid()) Exit(0)
GetName(FitResults, FileName0)
If (!SaveAsDialog("Please select destination", filename0, filename)) Exit(0)
//Result("\n Selected file path:"+filename+".dm3")
FitResults.SavelImage(filename+".dm3")
Filecount=FileCount+1

If (!FitResults4Byte.ImagelsValid()) Exit(0)
GetName(FitResults4Byte, FileName0)
If (!SaveAsDialog("Please select destination", filename0, filename)) Exit(0)
//Result("\n Selected file path:"+filename+".dm3")
FitResults4Byte.SavelImage(filename+".dm3")
Filecount=FileCount+1

If (!EXCELresults.ImagelsValid()) Exit(0)
GetName(EXCELresults, FileName0)
If (!SaveAsDialog("Please select destination", filename0, filename)) Exit(0)
//Result("\n Selected file path:"+filename+".dm3")
EXCELresults.SavelImage(filename+".dm3")
Filecount=FileCount+1

If (!Xsection.ImagelsValid()) Exit(0)
GetName(Xsection, FileName0)
If (!SaveAsDialog("Please select destination", filename0, filename)) Exit(0)
//Result("\n Selected file path:"+filename+".dm3")
Xsection.SavelImage(filename+".dm3")
Filecount=FileCount+1

If (!PerCentError.ImagelsValid()) Exit(0)
GetName(PerCentError, FileName0)
If (!SaveAsDialog("Please select destination", filename0, filename)) Exit(0)
//Result("\n Selected file path:"+filename+".dm3")
PerCentError.SavelImage(filename+".dm3")
Filecount=FileCount+1

OKdialog(FileCount+" files saved")

```